UNIVERSITAT POLITÈCNICA DE CATALUNYA
BARCELONATECH
Departament d'Enginyeria Electrònica

An Energy Management Strategy for Plug-in Hybrid Electric Vehicles

Tesi doctoral presentada per a l'obtenció del títol de Doctor per la Universitat Politècnica de Catalunya, dins el Programa de Doctorat en Enginyeria Electrònica

Benjamin Bader

Director: *Dr. José Luis Romeral*

Co-Director: *Dr. Gerhard Lux*

Noviembre 2013

Abstract

This dissertation formulates a proposal for a real time implementable energy management strategy (EMS) for plug-in hybrid electric vehicles. The EMS is developed to minimize vehicle fuel consumption through the utilisation of stored electric energy and high-efficiency operation of powertrain components. This objective is achieved through the development of a predictive EMS, which, in addition to fuel efficiency, is optimized in terms of computational cost and drivability.

The requirement for an EMS in hybrid powertrain vehicles stems from the integration of two energy stores and converters in the powertrain; in the case of hybrid electric vehicles (HEVs) usually a combustion engine and one or more electric machines powered by a battery. During operation of the vehicle the EMS controls power distribution between engine and electric traction motor. Power distribution is optimized according to the operating point dependent efficiencies of the components, energy level of the battery and trip foreknowledge. Drivability considerations, e.g. frequency of engine starts, can also be considered.

Powertrain hybridization is one of several measures which can increase vehicle fuel economy. Due to high oil prices and legislative requirements caused by the environmental impact of greenhouse emissions, fuel economy has gained importance in recent years. In addition to increased fuel economy, powertrain hybridization permits the substitution of fuel for electrical energy by implementing an external recharging option for the battery. This vehicle class, incorporating a battery rechargeable via the electrical grid, is known as a plug-in HEV (PHEV). PHEV share characteristics of both HEVs and all-electric vehicles combining several advantages of both technologies.

The rechargeable battery feature of the PHEVs makes their EMS development especially challenging. For minimal fuel consumption, the battery is discharged optimally over the whole trip length, prioritising electrical energy when driving conditions are such that its use maximises the fuel saving that can be achieved. Therefore, an EMS for a PHEV depends heavily on the availability of *a priori* knowledge about the trip, i.e. the knowledge about future vehicle speed and road grade. This requires the driver to indicate the route before trip start. The route knowledge in combination with GPS or Galileo based *next generation navigation systems* using information from a geographic information system (GIS) about terrain height profile, road type (e.g. motorway or country road), and legal speed limits can be evaluated by a speed prediction algorithm including information about the driver's behaviour for a detailed prediction of the trip.

These navigation systems and algorithms in combination with expected future advances and the deployment of technologies such as intelligent transport systems (ITS) and vehicle-to-vehicle communication (V2V), will make more exact traffic information available to further improve prediction. Despite expected advances in prediction quality, inaccuracy of prediction data has to be considered and is therefore regarded in this work.

The EMS proposed in this dissertation combines different approaches which are executed step by step. A first approximation of the energy distribution during the trip is based on a mixed integer linear program (MILP), which gives the optimal energy state of the battery during the trip. This is especially important for trips with long uphill, downhill or urban phases, i.e. sections with a particularly high or lower power requirement. The results from MILP are then used by a dynamic programming (DP) algorithm to calculate optimal torque and gear using a receding prediction horizon. Using a receding prediction horizon, an important reduction of computational cost is achieved. Lastly, from the DP results a rule-based strategy is generated using a support vector machine (SVM). This last step is necessary to ensure the drivability of the vehicle also for inaccurate prediction data. The dissertation is organized as followed:

Firstly, the vehicle models employed in the dissertation and its validation are described.

Secondly, a DP based algorithm is presented to compute the torque and gear during the trip. As DP is computational quite intensive, techniques are presented to lower the computational costs.

Thirdly, the DP algorithm is used in a model predictive control framework (MPC) with a receding prediction horizon. Necessary boundary condition of the battery state of charge (SOC) given by a SOC set point function for the entire trip are obtained using MILP.

Fourthly, the MPC framework is implemented in an adaptive rule-based strategy. This strategy is continuously adapted during the trip in respect to the MPC optimization results. The rule-based strategy ensures robustness of the EMS also for inaccurate prediction data.

Contents

List of Tables

List of Figures

List of Symbols

α_{acc}	accelerator pedal position
α_{brake}	brake pedal position
α_{road}	angle of road inclination
a	longitudinal vehicle acceleration
A_f	vehicle frontal area
c_w	vehicle drag coefficient
$E_{bat,min}$	minimum battery energy level
$E_{bat,max}$	maximum battery energy level
$E_{bat,nom}$	nominal battery energy capacity
E_{bat}	stored chemical energy in battery
f_{BW}	nonlinear vehicle backward model
f_{MILP}	linear vehicle model
F_{wh}	traction wheel force
g	gear
g_r	gear ratio (including final ratio)
Δh	road slope
J_{wh}	wheel inertia (sum of all four wheels)
m	vehicle mass
$\dot{m}_f$	engine fuel mass flow
P_{bat}	chemical battery power
P_{cycle}	wheel power requirement for driving cycle
$P_{em,max}$	maximum mechanical power of the electric motor as a fuction of ω_{em}
P_{em}	mechanical power of the electric motor
$P_{ice,max}$	maximum mechanical power of the engine as a fuction of ω_{ice}
P_{ice}	mechanical power of the engine

$P_{inv,AC}$	electrical power at AC (motor) side of the inverter
$P_{inv,DC}$	electrical power at DC (battery) side of the inverter
P_{wh}	wheel power
R_{bat}	battery internal resistance
r_{wh}	dynamic wheel radius
$T_{em,max}$	maximum electric motor torque as a function of ω_{em}
T_{em}	electric motor torque
T_{ice}	engine torque
$T_{ice,max}$	maximum engine torque as a function of ω_{ice}
T_{req}	torque requested by driver
η_{em}	electric motor efficiency
η_{inv}	inverter efficiency
η_{trans}	transmission and drivetrain efficiency
N_c	control horizon length
N_p	prediction horizon length
μ_r	vehicle rolling resistance
$\boldsymbol{u}$	control vector
Δt	sample time
SOC_0	battery state of charge at trip start
SOC_{end}	battery state of charge at end of trip
SOC	battery state of charge
$\widetilde{SOC}$	estimated battery state of charge
v	vehicle speed
v_{cycle}	driving cycle vehicle speed
V_0	nominal battery voltage
ω_{em}	electric motor shaft speed
ω_{ice}	combustion engine shaft speed
x	DP model state SOC

1 Introduction

1.1 Background and Motivation

In recent years, the issue of fuel economy in the development of transportation vehicles has gained increasing importance. This is mainly due to:

- the assumed impact of carbon dioxide (CO_2) on the climate
- legislative requirements
- the increasing price of oil and uncertainty over future price changes.

In 2009, transportation sector emissions amounted to 25% of the European Union (EU)'s total greenhouse gas emissions[1], and 29.9% of its CO_2 emissions. The contribution of road-only transport (i.e. cars, trucks and buses) to the transportation sector's total greenhouse gas emissions is 71.7%, which still corresponds to more than 14% of the EU's total emissions [1]. Taking into account the emissions caused by the complete energy transformation process (mines, plants, refineries, pipelines, etc.) to calculate end-user emissions, the figure of transportation sector greenhouse gas emissions rises to 29% [2]. Consequently, in 2009 legal requirements were made for car manufacturers to reduce the average CO_2 emissions of their fleet to 130g/km by 2015 and to 95g/km by 2020 [3].

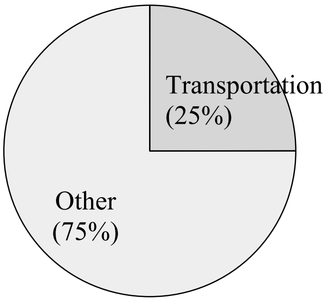

Fig. 1.1. Transportation sector greenhouse gas emissions (energy transformation emissions not included) in the EU in 2009 [1].

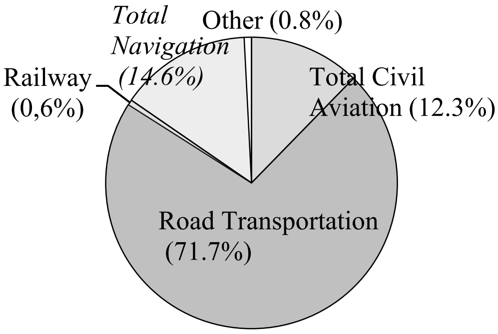

Fig. 1.2. Road transportation contribution to the transportation sector greenhouse gas emissions in the EU in 2009 (energy transformation emissions not included) [1].

---

[1] CO_2 equivalent emissions

In addition to environmental issues, the development of fuel efficient vehicles is motivated by economic factors, principally rising fuel prices over the last ten years. This price increase is mainly due to rising fuel duty and oil prices on the world markets (Fig. 1.3). Although new oil extraction techniques have been developed (tar sands in Canada and deep sea extraction off the coasts of Brazil and Nicaragua), the higher costs of these processes and the increased demand from developing countries have driven oil prices to new heights. Future oil price development is difficult to predict[2], but with rising extraction and production costs, a return to the low oil prices of the past seems improbable.

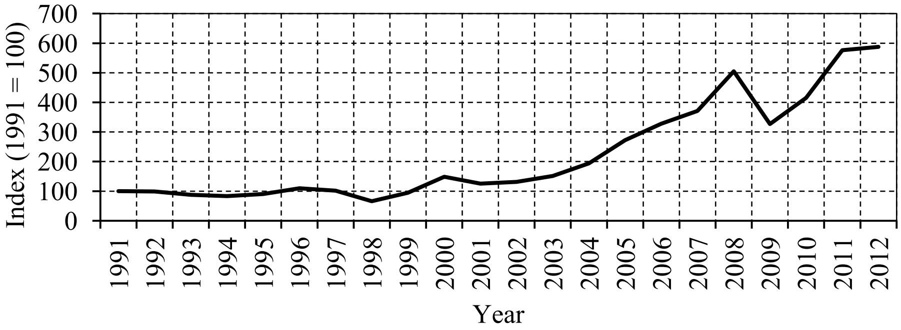

Fig. 1.3. Crude oil price development from 1981 to 2012 in US $ (Index 1991=100) [4].

Reduced fuel use brings political and economic benefits for oil importing countries - lesser dependence on politically unstable oil-producing regions, reduced impact of potential future oil shortages, and a positive effect on the domestic economy through reduced imports. Other advantages are reduced environmental damage, a reduction in global warming and climate change and its associated extreme weather phenomena. Summarising the above, increased fuel economy in automobiles is highly desirable.

Driven by increasing customer demand, manufacturers have already taken measures with vehicles using a *conventional* powertrain, i.e. a powertrain driven only by a combustion engine. Among those measures are the reduction of the vehicle's air drag coefficient, the use of lightweight materials, engine downsizing and temporary cylinder deactivation ("dynamic downsizing"). Major advances have been made in this area in recent years, resulting in a steady reduction in fuel consumption (Fig. 1.4). Another approach for fuel saving is the powertrain *hybridization*. Hybridization is the integration of an additional energy store and energy converter within a conventional powertrain. Usually, this is an electric motor with electrical energy store, which is normally an electrochemical battery or supercapacitor. Vehicles using this type of *hybrid powertrain* are

---

[2] In 2004 the International Energy Agency (IEA) predicted a crude oil price of 22$ / barrel for 2012. The actual price in 2012 was more than 100$ / barrel.

called hybrid electric vehicles (HEV). The additional electrical energy store and electric motor permit that some of the vehicle's kinetic energy can be regenerated while braking by operating the electric motor in generating mode. In addition, traction power demand can be decoupled in terms of time from the mechanical power output of the engine within certain limits. Therefore, the combustion engine can operate in higher efficiency regions. This is especially advantageous in urban traffic, which is characterised by frequent braking, long idle times and low engine load - while on motorways with their higher load profile the engine can operate without additional measures in high efficiency regions. Powertrain hybridization can be classified into different levels, according to the maximum power of the electric motor and the electrical energy store capacity. Vehicles with high levels of hybridization incorporate electric powertrain components which are similar in nominal electric motor power and battery capacity to all-electric vehicles, as e.g. battery electric vehicles (BEVs). HEVs with an energy storage system capacity comparable to BEVs, i.e. with an energy capacity of at least 4kWh, can recharge the battery not only by means of the engine but also by connection to the electrical grid (plug-in HEVs). These plug-in HEVs (PHEVs) have a more limited electric driving range than BEVs, but with the option of refilling with gasoline and thereby offering practically unlimited driving range.

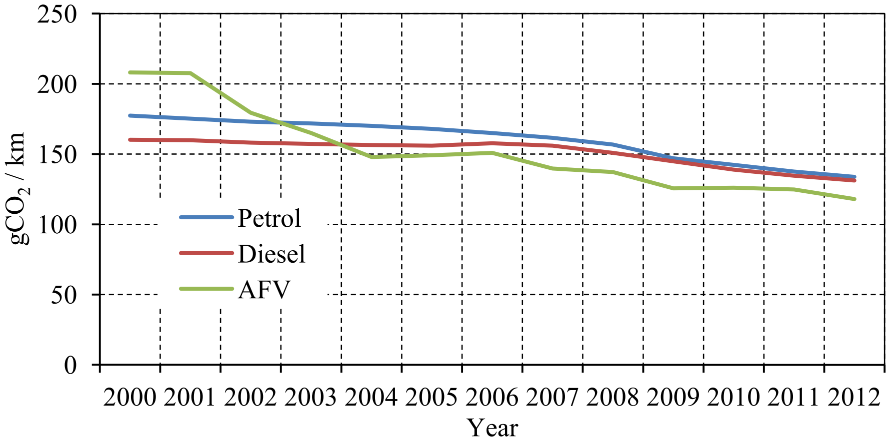

Fig. 1.4. Development of average CO_2 emissions of new passenger cars in the EU. The cars are classified into petrol, diesel and alternative fuel vehicles (AFV) including (P)HEVs [5].

By substituting fuel for electrical energy in vehicles, CO_2 emissions can be reduced significantly. In contrast to using fuel, when using electrical energy to propel the vehicle emissions are not generated directly by the vehicle, but at the power plants where the electricity is generated. Therefore CO_2 emissions depend on the methods of power generation and fuel type used at the power plant. In regions where large proportions of total energy output are generated by renewable sources (hydro-plants, wind/solar plants, etc) such as Sweden or Switzerland, the resulting CO_2 emissions are low. However, in regions where coal is the main source for power generation, emissions can be higher than those generated by conventional powertrain configurations without an electric motor (Fig. 1.5). Therefore, to be effective in reducing emissions, widespread use of PHEVs and BEVs must go hand-in-hand with clean electricity generation. The impact of widespread use of BEVs or PHEVs on electrical power generation would be minor, as the generated electrical grid load would be relatively small. In Germany, the additional electrical energy requirement of 10 million BEVs amounts to only 3% of current total electrical power production [6].

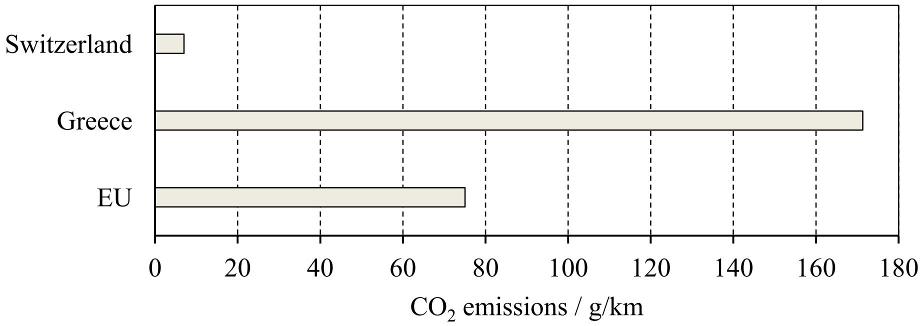

Fig. 1.5. Indirect CO_2 emissions of battery electric vehicles by region. Calculation based on a BEV with an electrical energy consumption of 18kWh/100km and a charging efficiency of 0.95 using data from [7].

1.2 Introduction to Hybrid Powertrain Concepts

Hybrid vehicles can have non-electric energy storage system such as flywheels [8], or, as in hydraulic hybrid vehicles, compressed gas [9] In the following work, only HEV concepts with electrical energy store are discussed, as they not only increase powertrain efficiency, but PHEVs can also substitute fuel for electrical energy as the traction energy source. HEVs have in addition to the fuel based energy store (natural gas, gasoline, diesel, hydrogen) an electrical energy store which is normally an electrochemical battery or a supercapacitor [10]. This electrical energy store supports bidirectional power transfer, i.e. it can both store and deliver energy. For PHEVs and most HEVs, this energy store is a battery and the fuel based energy store a petrol tank. In the following work, discussion is limited to (P)HEVs of this type.

There are a variety of different HEV concepts, which can be classified in terms of their *level of hybridization* or their powertrain configuration. HEV powertrain configurations differ in the number of electric machines they incorporate and in the manner in which they are physically connected to the combustion engine and wheels. The level of hybridization is defined by the power rating of the electric machine and battery capacity. Increasing levels of hybridization brings on the one hand benefits in the area of fuel economy, but on the other hand, higher fabrication costs. Conventional vehicles have the lowest level of hybridization (powertrain without electric components), and electric vehicles like BEVs with only electric powertrain components have the highest levels of hybridization. Between them, there are (in order of level of hybridization): micro HEVs, mild HEV, and full HEVs. There are no standardised definitions for the levels, and their definitions in literature are inconsistent. A typical classification is indicated in Table I.

Micro HEVs support mainly an engine start/stop function to reduce engine idle times and limited kinetic energy regeneration. Mild HEVs have a higher level of hybridization and support energy regeneration at higher loads, and load point shifting of the engine. Full HEVs with their stronger electric motor can, in addition, drive electrically. Vehicles with higher battery capacities have a battery charger onboard, which permits battery charging by connection to the electrical grid. HEVs with this charging capability are called plug-in HEVs (PHEVs).

Table I: Typical classification of HEV according to their level of hybridization.

	Micro HEV	Mild HEV	Full HEV	PHEV	BEV
$P_{em.max}$	< 6 kW	<25 kW	25-125 kW	50-125 kW	50-125 kW
$E_{bat,nom}$	<0.1kWh	<0.1kWh	<2kWh	> 4kWh	>12kWh
V_0	<24V	<60V	<600V	<600V	<600V

For evaluation of PHEV and BEV, typical trip length between two recharging stops is an important factor. The most common trip distances of passenger cars are distances less than 20km (Fig. 1.6). In Europe, 60% of trips in passenger cars are shorter than 30km and more than 70% of trips shorter than 50km (Fig. 1.7). According to these figures, in Europe, for the vast majority of trips the all-electric range achieved with today's battery technology is sufficient. However, as private customers demand vehicles without range restrictions, purchase of BEVs is mainly expected by companies. Due to range limitations and high costs, sales figures for all-electric vehicles were below 14,000 in 2012 in the EU [5] , despite government incentives such as the 7.000 euro premium offered in France. Therefore, PHEV must bridge the gap between HEV and BEV until battery technology is more advanced.

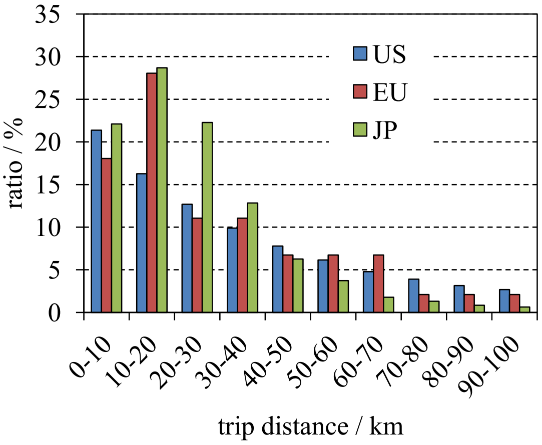

Fig. 1.6. Ratio of typical trip distances of passenger cars in Europe, the USA and Japan [11].

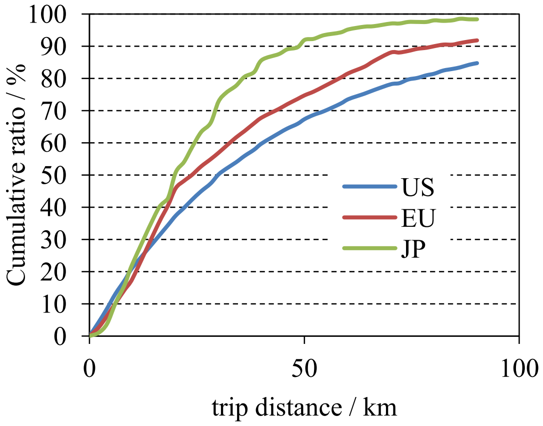

Fig. 1.7. Cumulative ratio of typical trip distances of passenger cars in Europe, the USA and Japan [11].

1.2.1 Hybrid Powertrain Configurations

In addition to the level of hybridization, HEV can also be classified in terms of the mechanical connections between engine, electric machines and wheels. There are four different configuration types: the series, parallel, series/parallel and power split concept. These configurations will now be briefly discussed.

All concepts include a battery, inverter and at least one electric machine. The exemplary vehicle in this work has a parallel powertrain, in which both the electric motor and the engine are mechanically connected to the wheels, so that the sum of electric motor and engine power propels the vehicle. The mechanical connection between engine and electric motor can be made using torque addition (the most common type); speed addition, incorporating a planetary gear; or traction force addition by connecting the electric motor and engine to the different driving axles [12]. In the exemplary vehicle, torque addition is achieved by mounting engine and electric motor on a common shaft (Fig. 1.8).

An advantage of the parallel configuration is that the electric powertrain components can be relatively easily integrated into conventional powertrains. Due to the direct mechanical connection of engine and drivetrain, engine power can be used for driving without the transformation losses which occur in the series concept. In parallel full HEV, the engine can usually be separated by a clutch from the rest of the powertrain to prevent friction losses when the vehicle is propelled electrically.

When the engine cannot be separated by a clutch, the configuration is referred to as a torque assist parallel hybrid. In [13] it is demonstrated that a torque assist hybrid has lower fuel economy compared with a full parallel hybrid with an identical level of hybridization. Therefore, this configuration is not common for powertrains with a high level of hybridization.

In contrast to the parallel configuration, in the series configuration only the electric traction motor has a mechanical connection with the wheels. The engine is coupled to a generator which delivers electrical energy to supply the electric traction motor. A battery is used as an energy buffer. A significant drawback of this configuration is that the engine power always suffers transformational losses via the conversion chain (engine-generator-inverter-electric motor). On the other hand, due to the energy buffer, the engine can operate in high efficiency regions and with slow operating point change, resulting in lower emissions of unburned hydrocarbons (HC) and carbon monoxide (CO). Wheel hub motors can also be used in this concept.

As only the electric motor is used to power the vehicle, drivability is better than with parallel full HEVs due to less engine starts and gear shifts. Having a mechanical connection between electric motor and wheels only, also results in greater freedom in the placement of components in the vehicle. Series HEV with an energy store capacity comparable to PHEV or BEV and which is chargeable via the electrical grid is referred to as a range extender configuration, as it is considered an electric vehicle with onboard charging unit.

Adding a mechanical connection between engine and electric traction motor to the series configuration, results in a *series-parallel* configuration. This configuration combines advantages of both series and parallel concepts, such as an increased number of available operation modes (for operation modes see Section 1.2.2), but at the cost of increased fabrication cost. In order to reduce costs and complexity, a two-speed gearbox between drivetrain and powertrain can be used, limiting engine use at lower vehicle speeds to the series operation mode. The *power-split* configuration is another configuration with two electric machines. A drive shaft, engine, motor and generator are connected through a planetary gear. Using a planetary gear, the torque ratio between electric machine and engine is fixed.

Fuel economy of the different configurations depends heavily on the component sizes, trip length, and power demand. Comparisons between the different plug-in powertrain configurations with identical all-electric range and acceleration capability show that the minimum possible fuel consumption depends on how much the trip length exceeds the all-electric range. Generally, for short trips below the typical range of electric vehicles, and with a low power profile, the series configuration has best fuel economy of PHEV powertrain configurations. For longer trips with a high power profile, the parallel configuration benefits from the direct mechanical power transmission from engine to wheels, avoiding the electrical losses in the component chain of the series configuration when using the engine to propel the vehicle. Results of the power-split configuration fall between the results of the series and parallel configuration [14], as due to the planetary gear a proportion of the engine power is transmitted mechanically to the wheels.

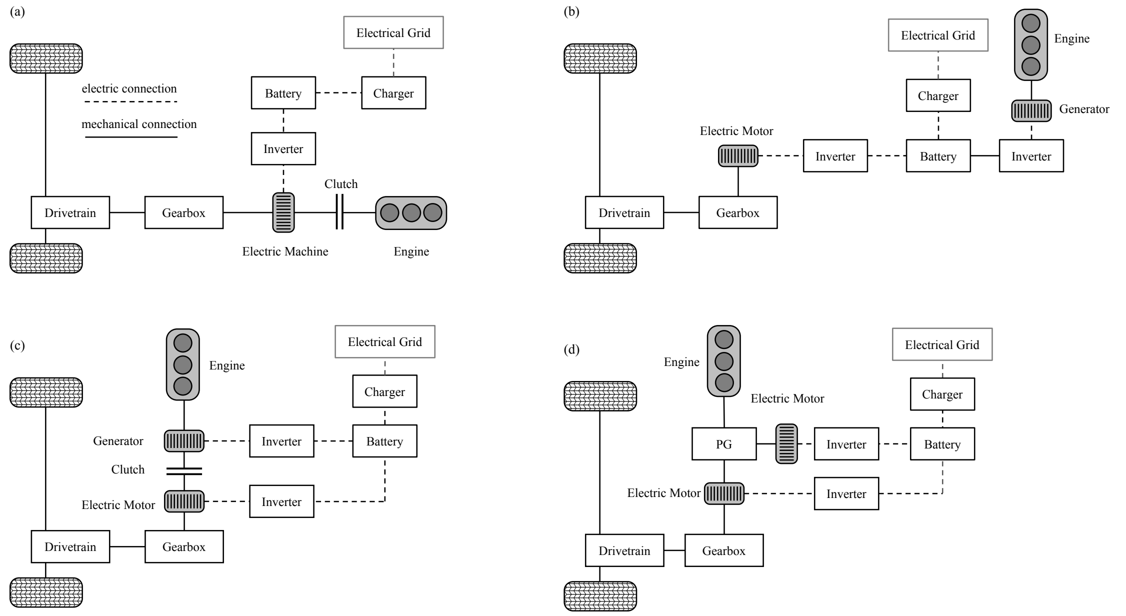

Fig. 1.8. Hybrid powertrain configurations: parallel (a), serial (b), serial/parallel (c) and power-split with a planetary transmission (d).

1.2.2 Operation Modes of Parallel PHEVs

The operation modes describe the operation states of the electric motor and engine. The available modes depend on the powertrain configuration. In the following discussion, only the four operation modes of the considered parallel configuration are introduced (Fig. 1.9). Driving electrically, the clutch between electric motor and engine is open and the vehicle has BEV behaviour. When accelerating, traction power is only delivered by the electric motor (*electric mode*). When braking, the battery is charged by operating the electric machine in generating mode to regenerate some of the vehicle’s kinetic energy (*regenerative braking mode*).

Closing the clutch and connecting the engine mechanically to the rest of the powertrain makes two more operating modes available. In *boost mode* the engine torque is lower than the torque demanded by the driver, and the electric motor supplies the difference. In *charge mode* the engine torque is higher than the requested torque and the electric machine operates in generating mode to recharge the battery. This enables operation of the engine in high efficiency regions during periods of low cycle power demand, a process known as *load point shifting* (Fig. 1.10). Engine-only operation, corresponding with a conventional powertrain configuration, is referred to as *ICE mode*.

Frequent switching from boost or charge mode to electric mode should be avoided by the EMS, as this requires starting or stopping the engine and employing the clutch. This results in a higher wear-rate for the clutch and can negatively affect drivability of the vehicle, as the changing vehicle sound is noticeable by the driver. For these transitions an engine start control is necessary which controls motor and engine speed before controlling the slip of the clutch [15].

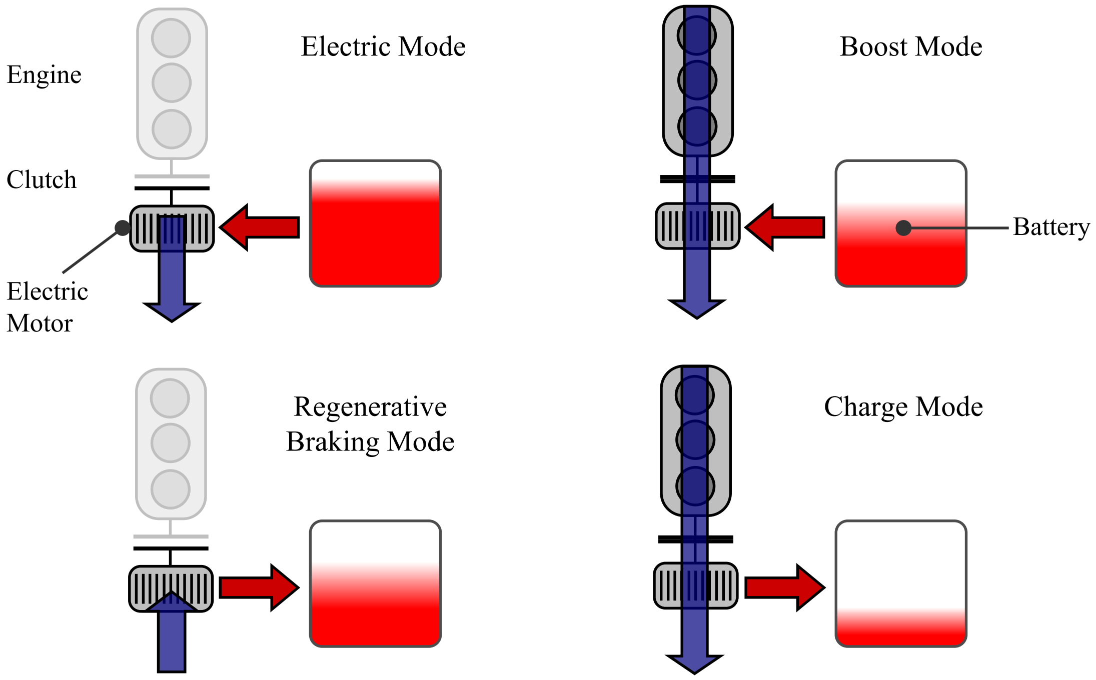

Fig. 1.9. Operation modes of a parallel PHEV. The blue arrows indicate mechanical power transfer, while the red ones indicate electrical power transfer.

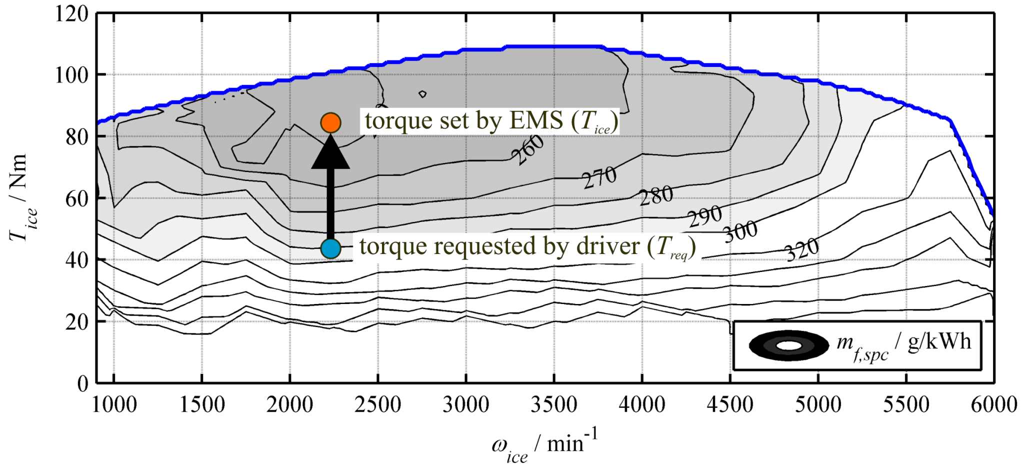

Fig. 1.10. Load point shifting. Engine operating points in the specific fuel consumption map.

1.3 Energy Management Problem

Road vehicle speed is controlled by the driver via a positive torque request via the accelerator pedal or a negative torque request via the brake pedal. The powertrain control problem of vehicles with conventional powertrains is straightforward, as positive torque is only supplied by the engine. In HEV, a positive torque is supplied either by the engine, the electric motor or by both. This difference makes necessary the use of an EMS. The EMS developed in this work is based on the assumption that vehicle speed is controlled by the driver by means of a torque control. There are other approaches to EMS which combine power distribution optimization with vehicle speed optimization [16]. Vehicle speed optimization is a method which can increase fuel efficiency in a conventional vehicle for a given trip [17].

The tasks of the EMS are distribution of torque demand T_{req} between electric machine (T_{em}) and engine (T_{ice}), gear shifting control, and engine starting and stopping. Optimization of engine torque is usually done in terms of fuel efficiency, but emissions can also be considered. When considering emissions, optimization of the engine operating point is a trade-off principally between nitrogen oxide (NO_x) emissions, and fuel efficiency [18]. With PHEVs, as a significant portion of the trip can typically be driven electrically, engine emission considerations are, relatively, of less importance with PHEV than HEV. Disregard of emissions considerations is also motivated by practical considerations, as engine emissions are influenced by the transient behaviour of the engine; considering emissions resulting from transient engine behaviour would require a more complex dynamic engine model and thus hamper execution in real time.

In order to improve drivability and reduce clutch wear, engine start and gear shift events are minimized. As gear shifting can move the engine operating point into higher efficiency regions there is also a trade-off between gear shifts and maximal fuel economy.

There is also a trade-off between engine start minimization and maximal fuel efficiency. Acceleration phases allow the engine to operate for a short time in high efficiency regions, but employing engine power in acceleration phases can lead to frequent engine starts. Therefore, a strategy minimizing the number of engine starts must operate the engine during trip sections which permit only sub-optimal operation (Chapter 5). However, short engine running periods also have adverse effects on engine efficiency, as following an engine start, for a period of time the engine operates below nominal operation temperature. Due to higher friction losses from cold lubricating oil, fuel consumption can be up to twice as high compared with a engine at nominal operation temperature [18], [19]if additional measures are not taken [20].

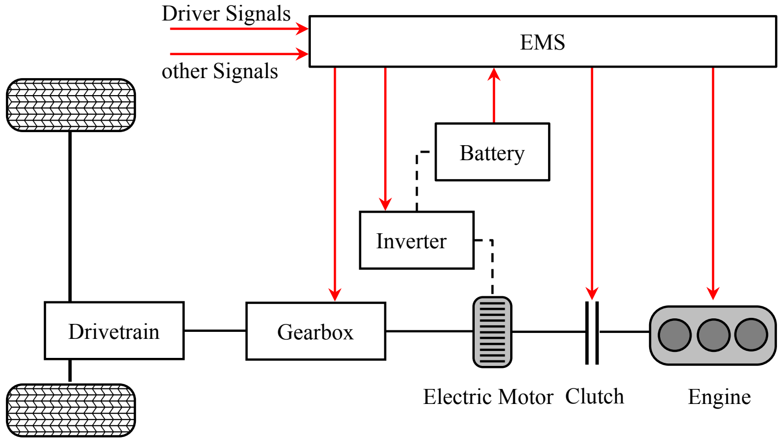

Fig. 1.11. Communication between EMS and powertrain components.

SOE control depends on whether the battery is rechargeable via the electrical grid or, as in autonomous HEV, only by means of the electric motor operating in generator mode. Therefore, for autonomous HEV the battery energy balance of a trip should be neutral, i.e. the electrical energy consumed by the electric motor should be returned by regenerative braking or by using charge mode. This mode of electrical energy use is called charge-sustaining mode (CS). By contrast, the battery in PHEV is preferably recharged via the electrical grid. Therefore, the aim is to deplete the battery across the trip, and recharge it at end of trip. This mode of operation is known as charge-depleting mode (CD). It must be considered that battery recharging times are much greater than refuelling times, and recharging during short standstills is not possible.

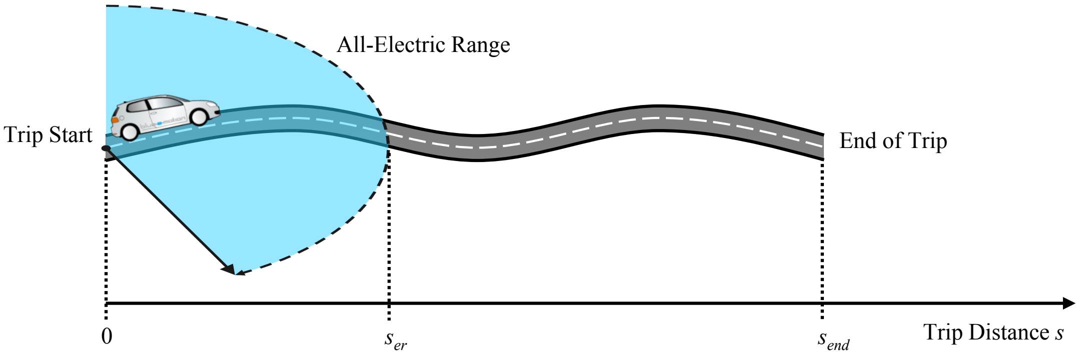

Fig. 1.12. Energy management problem for PHEV. For trips exceeding the all-electric range, the electrical energy is distributed over the entire trip for highest fuel efficiency.

To achieve charge depletion, two different approaches exist. The simplest implementation is referred to as all-electric mode, which begins the trip driving electrically. At charge depletion corresponding with distance s_{er} (Fig. 1.12), it switches to CS operation. This strategy does not necessarily need trip foreknowledge. However, fuel efficiency is lower than using *blended mode* strategies which employ engine use from trip start [21]. The SOC using an AER-focused strategy is depicted in Fig. 1.13, in which the SOC is managed such that it is equal at end of trip and trip start. At second 1117 the all-electric range (here defined when the SOC falls below 0.3) is reached and the engine is started (Fig. 1.15). In contrast, blended mode operation employs the engine from trip start (Fig. 1.16) and restricts engine use to high load trip sections (Fig. 1.18), whereas the all-electric mode has to operate the engine during low load sections in charge mode which causes additional electrical losses (Fig. 1.17). The result is 4.0% lower fuel consumption for this cycle using the blended strategy. However, blended CD strategies depend more on the availability of trip prediction data.

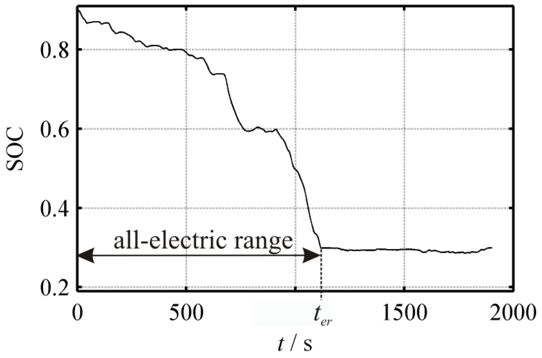

Fig. 1.13. SOC during the BCN-CTS cycle using an AER-focused strategy.

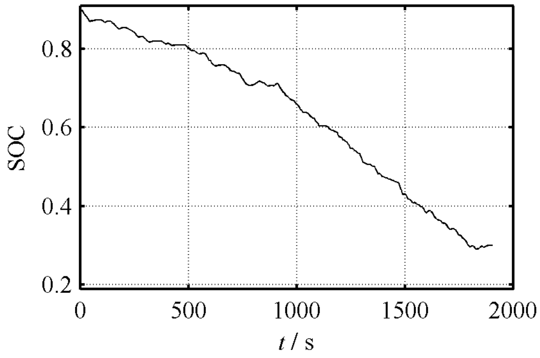

Fig. 1.14. SOC during the BCN-CTS cycle using a blended strategy.

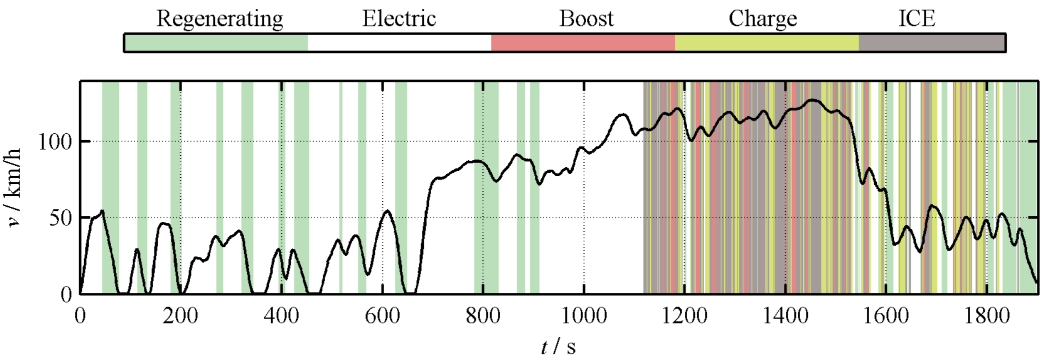

Fig. 1.15. Operation modes during the driving cycle BCN-CTS using an AER-focused strategy.

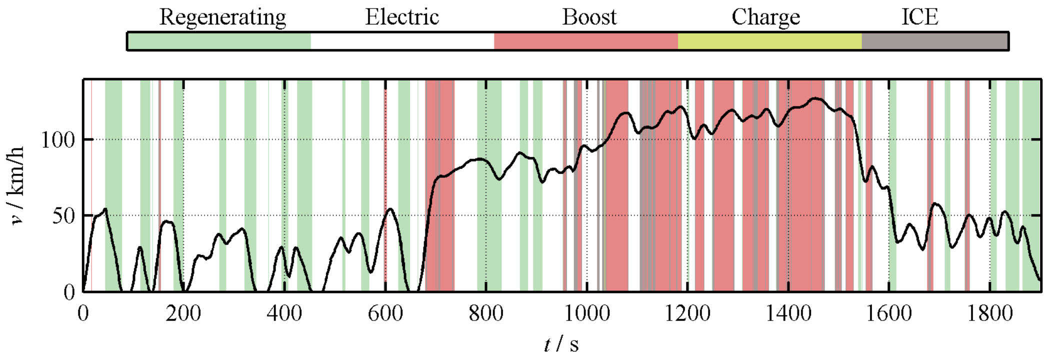

Fig. 1.16. Operation modes during the driving cycle BCN-CTS using a blended strategy.

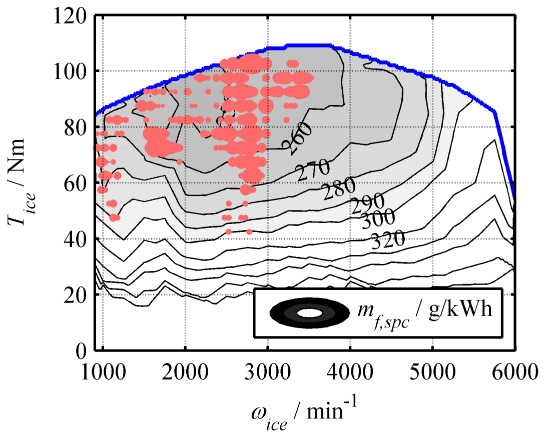

Fig. 1.17. Engine operating points using an AER-focused strategy during BCN-CTS.

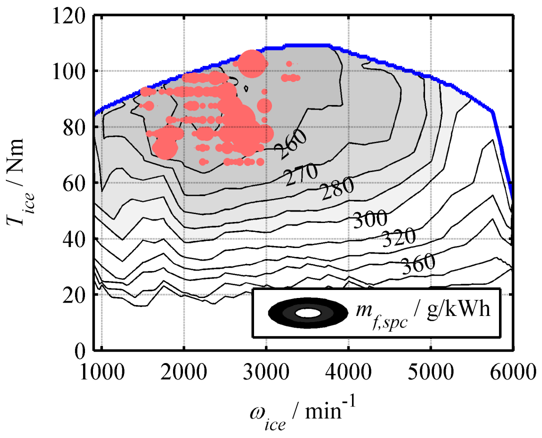

Fig. 1.18. Engine operating points using a blended strategy during BCN-CTS.

Focussing on the mathematical formulation of the control problem, the control of engine, electric motor, and gear can be simplified to a control of the motor torque T_{em} and the gear g. The resulting control vector $\boldsymbol{u}$ is

$$\boldsymbol{u} = \begin{pmatrix} T_{em} \\ g \end{pmatrix} \quad . \tag{1.1}$$

The combustion engine torque T_{ice} can be calculated using the torque demanded by the driver and the electric motor torque T_{em} using

$$T_{ice} = T_{req} - T_{em} \quad . \tag{1.2}$$

The engine state s_{ice} refers to whether the engine is running or switched off and is defined by

$$s_{ice} = \begin{cases} 0 & \text{engine off} \\ 1 & \text{engine on} \end{cases} , \tag{1.3}$$

and can be defined with Eq. (1.2) as function of the control vector $\boldsymbol{u}$:

$$s_{ice} = \begin{cases} 0 & T_{ice} = 0 \\ 1 & T_{ice} > 0 \end{cases} . \tag{1.4}$$

As engine speed ω_{ice} and motor speed ω_{em} are defined by gear ratio and vehicle speed, the engine and electric motor operating points are entirely defined by $\boldsymbol{u}$.

The complexity of the control problem results from two key factors: Firstly, the challenge of solving a predictive fuel efficiency optimization in real time. Secondly, in addition to fuel economy, consideration must be given to engine starts and gear shifts. This explains why engine starts, gear shifting, and complete charge depletion are often neglected in literature.

1.4 State of the Art

Owing to the external recharging capability of PHEVs, not all the electrical energy used in their operation must be generated by the powertrain itself. Thus EMS for PHEV differs from other EMS in that it targets CD operation with negative electrical energy balance. Therefore, for minimal fuel consumption PHEVs require predictive strategies which use information about power load and vehicle speed during the future trip. Once the trip destination has been indicated by the driver, using data of a geographic information system (GIS) the optimal trajectory can be determined using path-finding algorithms. From the known trajectory, the navigation system can deliver information about road type, legal speed limits, traffic, maximum possible speeds due to curves, and road grade to a load prediction algorithm which generates a load profile of the trip [22], [23]. Predicted trip speed v_{cycle}, required wheel power P_{wh} and road grade α_{road} are calculated by the load forecasting algorithm as a function of time (Fig. 1.19).

In the future, predictive capabilities will be enhanced by the availability of additional traffic information from intelligent transportation system (ITS) or vehicle-to-vehicle communication (V2V) processed by traffic flow modelling such as gas-kinetic based models [24]. Driving style influences can also be considered by using neural networks for prediction [22].

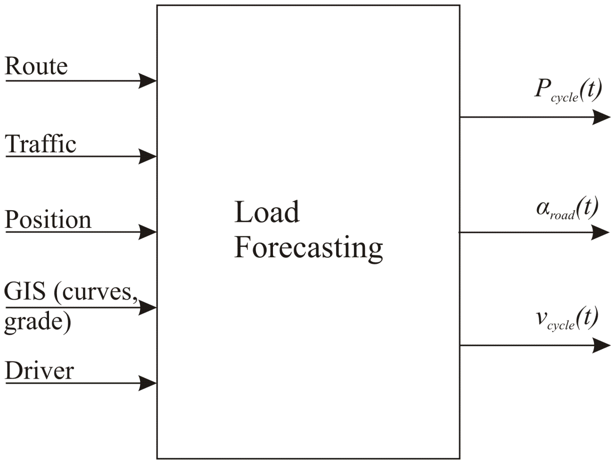

Fig. 1.19. Information used by load forecasting algorithms for trip prediction.

Many EMS concepts have been already studied; an overview of strategies for HEV can be found in [25] and for PHEV in [26]. EMS approaches can be classified into heuristic and optimization based strategies. Among heuristic strategies are rule-based strategies where operation mode is selected according to “if... then...” rules based on vehicle or engine speed and the power or torque requested by the driver. The rules determine the power distribution such that the operating points of engine and electric motor lie in high efficiency regions [18] and can be designed to imitate optimal behaviour during different driving cycles calculated using optimization techniques [27]. The rules can also be based on fuzzy logic as presented in [28] for a parallel powertrain, and in [29] for a series PHEV.

While early development of EMS focused on rule-based strategies, recent focus has been on optimization based EMS. Approaches are often based on Pontryagin’s minimum principle, which was first used for HEVs [30] and later adapted to the requirements of PHEVs [31]. Using this strategy, SOC at end of trip depends on the initial conditions chosen for the Lagrange multipliers of the Hamiltonian function, which is minimized to obtain the optimal control policy.

The same problem results from employing, instead of the Hamiltonian function, a Lagrange approach; where the costate is not known *a priori* and therefore has to be estimated and then adapted during the trip depending on the SOC [32]–[34]. Under certain assumptions, the theory can be used as theoretical background [35] for a strategy using an instantaneous cost function using a weighting factor for electrical and fuel energy [36]. This approach has been used before in [37], where it was derived intuitionally. For optimality, this weighting factor has to be calculated before starting the trip to achieve target SOE at end of trip. Therefore, even though the cost function is instantaneous, trip foreknowledge is still required.

Alternative approaches adapt the weighting factor according to SOE development during vehicle operation by using a penalty function [38]–[40]. For PHEV, an online adaptation of the weighting factor using trip foreknowledge has been presented in [41]. In [42] quadratic programming is used to optimize the weighting factor considering route prediction information with the aim of full battery depletion.

Another common approach, based on the optimality principle of Bellman [43], is time-discrete dynamic programming (DP) [44]. This approach is most often used as a benchmark for other EMS due to its high computational cost [45]. It is used in [46] for a parallel HEV and in [47] for a series HEV. Considering it yields the global optimum with the boundary condition of the SOE at trip start and end of trip, it is also used in combination with stochastic driving cycles for HEV component sizing [48]; deriving rule-based strategies [27]; and training neural networks which imitate the optimization results [49].

Real-time DP implementation in combination with route prediction data has been described in [50], where measures are taken to reduce DP computational cost (Section 3.2). Another real-time implementation of DP is presented in [34], where gear optimization is combined with a torque optimization based on Pontryagin’s minimum principle.

Stochastic dynamic programming (SDP) can be employed when trip foreknowledge is not known. In [51] this technique is used with stochastic driver power demand generated by a Markov process which is optimized for an infinite time horizon to obtain a time-invariant CS strategy.

In [52] SDP is used for a power-split powertrain configuration to implement both CS and CD operation, using as a cost function the ratio of fuel and the price of electrical energy. Using SDP, it is not possible to determine a target SOC at end of trip as the EMS is generic and is optimized for different driving cycles. SDP is also used in combination with Markov chain modelled driving cycles to demonstrate that predictive strategies using trip foreknowledge can reduce fuel consumption in autonomous HEVs [53]. For PHEVs, predictive strategies are even more important, as in order to achieve maximum fuel economy full battery depletion must coincide with end of trip.

Linear programming is used in [54] for the EMS of a series HEV due to its low computational cost. However, the extent of its use is limited due to the requirement of a linear vehicle model. Using mixed integer linear programming, engine starting/stopping can be considered and is used in [55] with a parallel HEV. Gear shifting, however, is not optimized in this study, and instead a standard gear shifting table for a conventional powertrain has been used. This fast technique has not yet been used in combination with gear optimization due to the restrictions of linear models. Another technique yielding sub-optimal results is the $\mathcal{H}_\infty$ control [56], which does not use any *a priori* knowledge about speed and power of the future trip.

The above mentioned studies mainly do not consider drivability aspects such as engine start/stop frequency and gear shifting due to the greater complexity of the vehicle model required. In [57] the mechanical energy required to start the engine from standstill to idle speed is considered. Engine start/stop control has been combined with the above described power weighting factor approach for CS operation [57]. In [58] SDP is employed and drivability aspects are included in the cost function. However, as trip foreknowledge is not used the final SOC cannot be controlled.

In [59] gear shifting losses are considered, and gear shifting limited for a mild hybrid parallel structure. Owing to the challenges of optimizing fuel economy, engine starts and gear shift at low computational cost, the EMS developed in this work considers engine starts and gear shifts indirectly by embedding optimized power distribution and gear shifts within a rule-based strategy.

Optimization results presented are given as torques T_{em} and T_{ice} or their ratio. Problems arise when predicted trip data and real values do not coincide due to overtaking maneuvers, standstill caused by traffic lights, or erroneous traffic information. Erroneous prediction data leads to erroneous torque calculations, and consequently vehicle speed does not correspond with the driver's demand. Using the torque/power ratio instead, vehicle speed is controlled correctly, but resulting torques are no longer optimal. The influence of erroneous prediction data on fuel consumption for a weighting factor based EMS has been evaluated in [60].

1.5 Energy Management Strategy Proposal

Evaluating the existing EMS approaches summarized above, the following requirements for the EMS have been identified:

- use of predictive optimization
- support for charge depletion across the trip using blended mode operation
- consideration given to frequency of engine starts and gear shifts
- robustness against inaccurate prediction data.

To meet these requirements a three step based approach for the EMS is used. Each step is presented in its own chapter. EMS foreknowledge of the future trip regarding vehicle speed, acceleration and road slope is assumed. When the trip destination is known (i.e.

indicated by the driver), the vehicle speed, acceleration, and road grade α_{road} can be predicted (see Section 1.4).

As the focus is on gear and torque/power control, the trip prediction process is not considered in this study. For EMS development prediction data accuracy is assumed, and in Section 5.8 the robustness of the EMS against inaccurate prediction data is evaluated.

Before starting the trip, the first step taken by the EMS is to calculate the optimal power distribution between engine and electric motor for the trip (Chapter 3). Calculation is based on a rapid MILP using a linear vehicle model. From optimal power distribution, the optimal battery power P_{bat} and thus the SOC during the trip are obtained (Fig. 1.13, Fig. 1.14). A necessary boundary condition of the optimization is the SOC at end of trip. As depth of discharge significantly effects the battery life cycle, it is recommended that a full discharge is avoided, and instead energy levels are kept within a limited SOC window. The SOC window adopted for this study is $SOC(t) \in [0.2; 0.9]$. As the objective of the EMS is to substitute fuel for electrical energy as the power source, at end of trip the EMS should reach full battery depletion. In order to guarantee CS operation without recharging at end of trip, a target SOC of 0.3 is selected. Starting the trip with a fully charged battery, 2.4kWh of electrical energy corresponding to $\Delta SOC = 0.6$, can be depleted (Fig. 1.20).

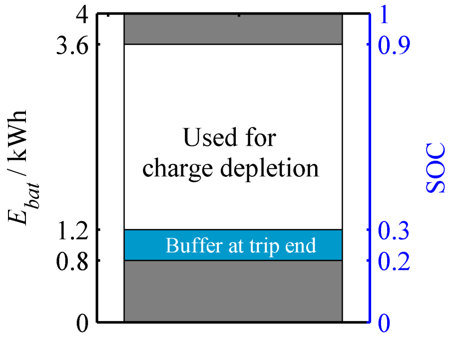

Fig. 1.20. Use of stored electrical energy during a trip. The trip is considered to start with the maximum SOC of 0.9. At end of trip a buffer for CS mode remains.

Knowing the optimal $SOC^*(t)$ for the trip and the power P_{ice} and P_{em}, the second step taken by EMS is to calculate the torque T_{ice}, T_{em} and the gear g .These torques cannot be directly calculated from P_{ice} and P_{em} without knowledge of motor or engine speed, due to $P = \omega T$. Both engine and motor speed depend on vehicle speed v and gear g, which cannot retrieved from the MILP employed by the EMS in the first execution step. In order to determine the gear and torque, a second optimization is carried out using a nonlinear vehicle model (Chapter 3). This optimization is executed repeatedly during the trip within a model predictive control (MPC) framework (Fig. 1.21). Computational load undergoes a rise due to the nonlinear vehicle model and the different optimization algorithm required, and therefore an MPC framework using a receding prediction horizon is employed.

The SOC boundary conditions of the optimization carried out within the MPC framework are given by the function $SOC^*(t)$, calculated in the first execution process before trip start. From this second execution step optimal torque and gear in terms of fuel efficiency are obtained. To provide robustness against inaccurate prediction data, results obtained are used to adapt a rule-based strategy online in a final execution step (Chapter 5). To reduce engine start and gear shift frequency, the operation mode is controlled by the rule-based strategy.

The above described approach combines the fuel efficiency of an optimization based strategy with the reduced number of gear shifts and engine starts of a heuristic approach. In the case of inaccuracy of the prediction data, operation in charge mode is controlled by prior calculated electric motor and engine torque lookup tables. The MPC approach is, when using an control horizon of 60s, capable of achieving the desired SOC at end of trip [61]. The EMS presented above can be used for both CS and CD operation. In both cases, results obtained demonstrate near high fuel efficiency, and reduced engine starts and gear shifts, in comparison with the global optimum.

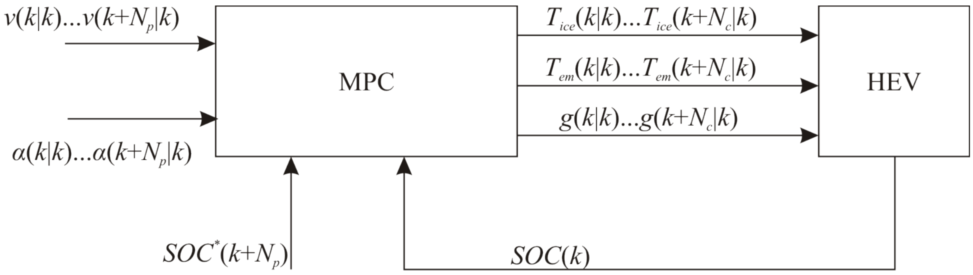

Fig. 1.21. The EMS uses trip prediction data and the current SOC, in an MPC framework, to calculate the optimal torque and gear of the trip within the prediction horizon.

2 Vehicle Model

This chapter discusses, first the characteristics of the exemplary vehicle used in the simulations. Next, the linear and nonlinear model approaches are described, and finally the models are validated with measurements.

The vehicle is a passenger car based on the SEAT Ibiza ST with conventional powertrain. To evaluate the EMS developed in the following chapters, fuel and electrical energy consumption of the vehicle is determined by simulating the longitudinal dynamics of this vehicle.

For simulation of fuel and electrical energy consumption, a quasi-stationary approach is sufficient [62]. Simulation of fuel consumption of the engine and electrical energy consumption of the electric motor is based on measured fuel mass flow and loss lookup tables, which describe the fuel mass flow and electrical losses in respect to the operating point. Carbon dioxide emissions can be calculated from engine fuel mass flow, their relationship being directly proportional. Other exhaust gases generated by the engine, however, cannot be considered using this approach. For detailed exhaust emissions simulation, a dynamic engine model would be necessary to simulate the engine's transient behaviour.

For the different optimization algorithms employed by the EMS proposal, two different vehicle models are necessary. The more complex nonlinear one is in the following referred to as *forward model*. The modelling approach of the forward model corresponds to a real driving situation: a driver, modelled mainly by a PI controller, acts on the accelerator and brake pedal. The inclination of the accelerator pedal is translated by the EMS of a HEV, or by the engine control unit (ECU) in conventional vehicles, into a torque or throttle demand for the combustion engine model (Fig. 2.1).

The DP algorithm (Chapter 3) performs optimization using a simplified *backward model* (Fig. 2.2). With the exception of the driver model, this model is based on the same component models of the forward model. Instead of a driver, the vehicle speed is assumed to correspond at every instant with the driving cycle speed. This assumption reduces the computational cost and hence is used as internal vehicle model for optimization algorithms (as is used later in this work for the DP implementation). Another advantage of the vehicle model is that due to the coincidence of vehicle and cycle speed the model has one state less than the forward model, which greatly reduces the complexity of DP optimization. While the forward model is computationally more intensive, it can, in addition to vehicle fuel consumption simulations, also be used on hardware-in-the-loop (HIL) test benches or for the validation of EMS.

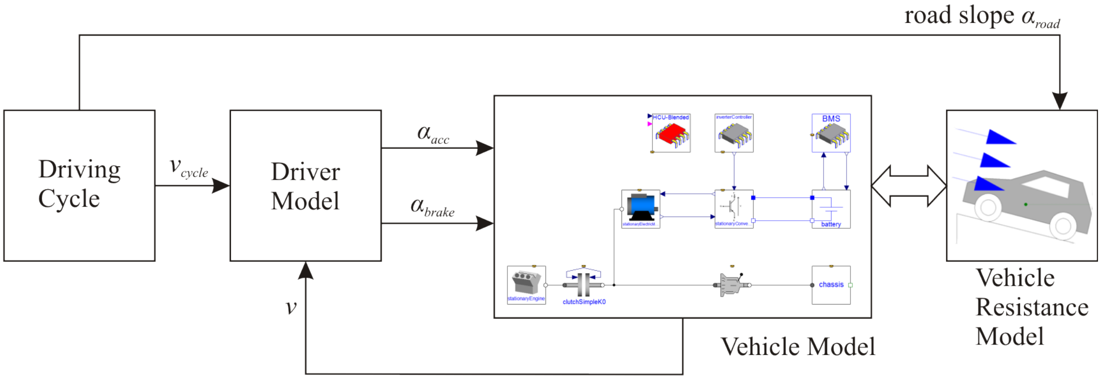

Fig. 2.1. Principle of the vehicle forward model. The driver model controls the pedal variables α_{acc} *and* α_{brake} *depending on the driving cycle speed* v_{cycle} *and vehicle speed* v*.*

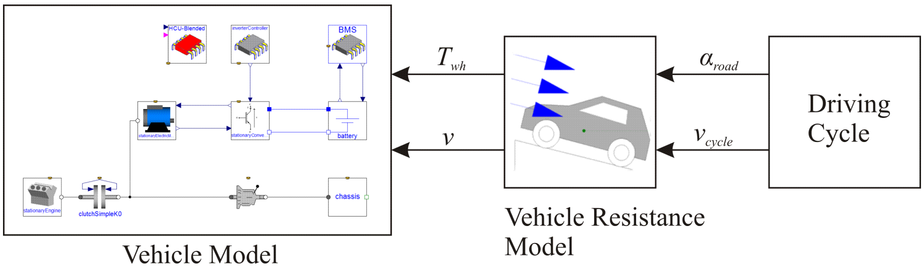

Fig. 2.2. Principle of the vehicle backward model. Vehicle speed corresponds exactly to the driving cycle speed.

2.1 Vehicle Characteristics

The exemplary HEV has vehicle body parameters similar to a conventional SEAT Ibiza ST passenger car and a parallel powertrain configuration in which the electric motor and the combustion engine are mounted on the same shaft. The engine can be separated by a clutch from the rest of the powertrain to avoid engine friction losses when driving electrically (Fig. 2.3). The parallel configuration permits the use of a small engine, as the engine can be supported by the electric motor using boost mode. The exemplary vehicle has a 3cyl, 51kW naturally aspirated engine. The electric motor is a permanently excited synchronous machine with a power rating of 80kW. The high power rating is required to deliver sufficient torque in the field weakening range. The double clutch gearbox has seven gears, such that motor and engine can operate at all vehicle speed in high efficiency regions. Due to the double clutch principle of the ATM transmission, fast gear shifting is assumed. Due to fast gear shifting, the interruption of the power transfer when opening the clutch of a standard ATM is disregarded. Therefore, velocity tracking loss (i.e. the additional power required after shifting and closing the clutch to compensate for the interruption) powershifting ATM does not occur [63] and shifting losses are neglected in the powertrain model. The battery with an energy capacity of 4kWh uses Li-ion technology. Its weight is estimated to be 150kg, taking into account mechanical protection and cooling components. When choosing the battery technology (Li-ion, NiMh), in addition to energy and power density [64], the cycle life as a function of the depth of discharge has to be considered. The total energy has to be chosen considering these parameters [65]. The battery can be recharged by operating the electric machine in generating mode or at end of trip by connecting the built-in charger to the electrical grid.

The vehicle base mass corresponds to the vehicle weight of the SEAT Ibiza ST without the engine and transmission and is adapted regarding the additional components of the electric system as indicated in Table II. The sum of the estimated component masses of the hybrid powertrain yields a total vehicle weight including the driver of 1450kg. The complete simulation parameters are indicated in Table III.

Due to direct mechanical connection of engine and electric motor to the wheels, the torque sum $T_\Sigma = T_{ice} + T_{em}$ is transmitted to the gearbox input when closing the clutch. As engine and electric motor speed are equal, the sum of the mechanical power is applied to the transmission. As depicted in Fig. 2.4, the combination of both machines leads to a high maximal torque at every engine/motor shaft speed. As indicated in Fig. 2.5, the available maximal power rises from 98.2kW at 1500min^{-1} up to a maximum power of 130.6kW at 4000min^{-1}.

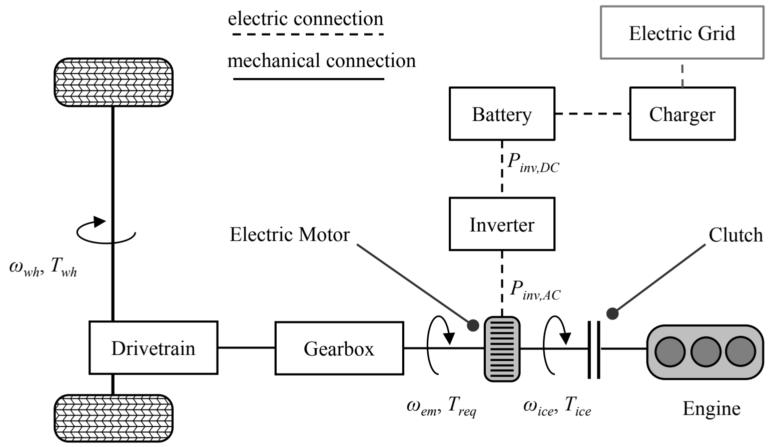

Fig. 2.3. Variables of the parallel PHEV powertrain.

Table II: Estimated vehicle component mass.

Base mass (SEAT Ibiza ST)	950kg
Battery system (4kWh)	150kg
Double clutch transmission (7 speed)	100kg
Engine (3cyl., 51kW)	90kg
Electric motor (80kW)	40kg
Power electronic	40kg

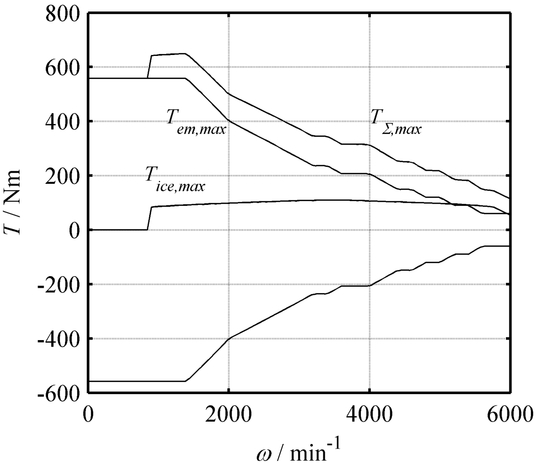

Fig. 2.4. Measured maximal torque of electric motor, combustion engine and its sum $T_{\Sigma,max}$ at the transmission input.

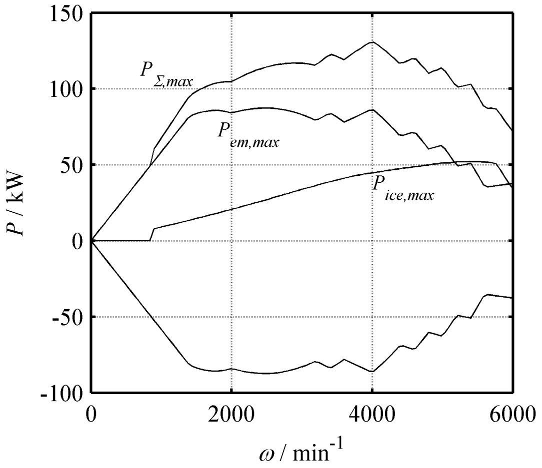

Fig. 2.5. Measured maximal power of electric motor, combustion engine and the sum $P_{\Sigma,max}$ at the transmission input.

The specific fuel consumption $\dot{m}_{f,spc}$ of the engine is defined as

$$\dot{m}_{f,spc} = \dot{m}_f / P_{ice} \quad . \tag{2.1}$$

Minimal specific consumption is reached at a speed of 2000min^{-1} and a torque $T_{ice} >$ 75Nm (Fig. 2.6). The optimal consumption line depicted is defined as

$$T_{ice,spc,min}(\omega_{ice}) = \arg\min_{T_{ice}} \frac{\dot{m}_f(T_{ice}, \omega_{ice})}{P_{ice}(T_{ice}, \omega_{ice})} \quad . \tag{2.2}$$

The electric motor has highest efficiency at speeds between 1000min^{-1} and 4400min^{-1} torque values above 60Nm (Fig. 2.7).

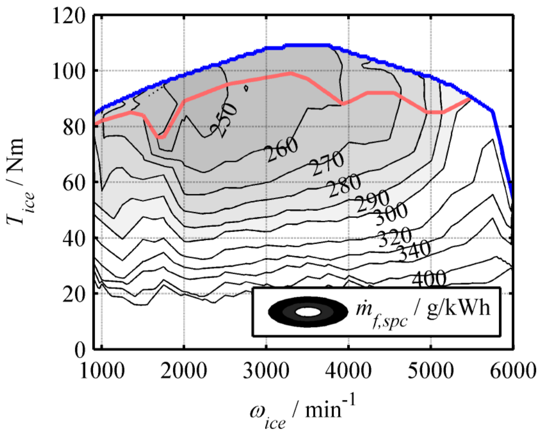

Fig. 2.6. Measured specific fuel consumption map and optimal consumption line $T_{ice,spc,min}$ *of the combustion engine.*

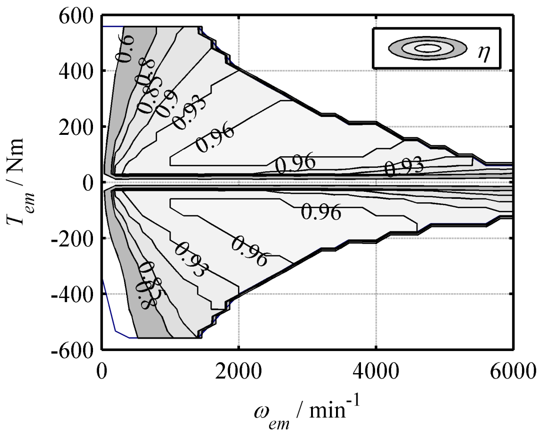

Fig. 2.7. Measured electric motor efficiency map.

2.2 Simulation Tools

There are several specialised simulation environments for the modelling of vehicle powertrains such as ADVISOR [66] or PSAT [67] and environments with specialised libraries such as MATLAB/SIMULINK and MODELICA/DYMOLA [68]. In this project, owing to their higher flexibility in the modelling process, MODELICA/DYMOLA and MATLAB/SIMULINK are employed. Here, flexibility for adaptations is very important, as the models are also employed in a HIL real-time application. MATLAB/SIMULINK is a classical block orientated language, i.e. physical equations have to be transformed regarding the input/output direction of the respective block. The modelling language MODELICA supports acausal modelling, i.e. the blocks do not necessarily have an input/output orientation. This is advantageous in that the physical systems are described in more simple terms. DYMOLA supports modelling with MODELICA by a graphic user interface (GUI) and represents a solver for the resulting differential algebraic equations (DAE). Due to this intuitive modelling and flexibility, it is also used for the design of HEV controllers [69]. The vehicle forward model is later integrated in a Simulink block for HIL validation (Section 2.6). In order to simplify communication with the optimization algorithm of Section 4.2, which has been written as MATLAB script, the linear model (Section 2.4) is directly modelled in MATLAB.

Table III: Values of the simulation parameters.

Symbol	Quantity	Value	Unit
m	vehicle total mass	1450	kg
A_f	vehicle frontal area	2.2	m²
a_g	gravitational acceleration	9.81	m/s²
c_w	drag coefficient	0.325	-
μ_r	rolling resistance	0.01	-
ρ	air density	1.2	kg/m³
r_{wh}	dynamic wheel radius	0.29	m
J_{wh}	total wheel inertia	4	kgm²
g	gear	$\{1; 2; 3; 4; 5; 6; 7\}$	-
g_r	gear ratio (including final ratio)	$\{15.5; 10.1; 6.8; 5.0; 3.8; 3.1; 2.6\}$	-
$P_{ice,max}$	max. mechanical power of ICE	51	kW
$T_{ice,max}$	max. torque of ICE	110	Nm
$P_{em,max}$	max. mechanical power of EM	80	kW
$T_{em,max}$	max. torque of EM	400	Nm
$E_{bat,nom}$	nominal battery capacity	4	kWh
$E_{bat,max}$	max. battery energy level	3.6	kWh
$E_{bat,min}$	max. battery energy level	0.8	kWh
V_0	battery nominal voltage	300	V
R_{bat}	battery internal resistance	366.67	mΩ

2.3 Quasti-Stationary Nonlinear Model

In this section, a quasi-stationary vehicle model is described. Due to the use of measured consumption tables for engine and electric motor and the non-constant transmission ratio the model is nonlinear. The model is created in the environment MODELICA/DYMOLA and used as a forward model for the EMS simulation and its HIL validation. An implementation as a backward model is used by the DP algorithm of Chapter 3. In the backward model, a driver model is omitted assuming that the vehicle speed v corresponds at every instance to the driving cycle speed v_{cycle}:

$$v(t) = v_{cycle}(t) \quad . \tag{2.3}$$

This assumption simplifies its use as internal vehicle model of optimization algorithms due to reduced complexity compared with a forward model, in which vehicle speed is an additional state variable. The vehicle forward model instead includes a driver model based mainly on a PI controller which adapts the accelerator pedal inclination α_{acc} as a function of the deviation of vehicle speed from cycle speed. The demanded torque T_{req} by the driver is a function of the pedal inclinations and engine and electric motor speed:

$$T_{req} = f_{req}(\alpha_{acc}, \alpha_{brake}, \omega_{em}, \omega_{ice}) \quad . \tag{2.4}$$

This control of T_{req} by means of a PI controller is required for HIL simulations, as the used ECU does not support torque control. In the following, the components of the forward and backward models are described and differences indicated. While the forward model is modelled by time continuous equations, the backward model is time discrete. The wheel force F_{wh} is calculated as a function of vehicle speed v and horizontal road angle α_{road} (Table III) by

$$\begin{aligned} F_{wh}(v, \alpha_{road}) = \mu_r m a_g \cos \alpha_{road} + \left(m + \frac{J_{wh}}{r_{wh}^2} \right) a + \frac{1}{2} \rho c_w A_f v^2 \\ + m a_g \sin \alpha_{road} \quad , \end{aligned} \tag{2.5}$$

where a_g is the gravitational acceleration and ρ the air density as indicated in Table III. The wheel torque during the driving cycle is obtained using Eq. (2.5):

$$T_{wh}(v, \alpha_{road}) = F_{wh}(v, \alpha_{road})\, r_{wh} \quad . \tag{2.6}$$

With Eq. (2.5), (2.6) and

$$P_{wh}(v, \alpha_{road}) = T_{wh}(v, \alpha_{road})\, v / r_{wh} \tag{2.7}$$

results that also the wheel power P_{wh} transmitted to the wheels corresponds in the backward model at every instance the cycle power requirement P_{cycle}:

$$P_{cycle}(v_{cycle}, \alpha_{road}) = P_{wh}(v, \alpha_{road}) \quad . \tag{2.8}$$

The torque T_{req} stands in a direct relation with T_{wh} as a function of gearbox efficiency η_{trans} and gear ratio g_r (which includes both speed ratio of both gearbox and final drive):

$$T_{req} = \begin{cases} \dfrac{T_{wh}}{\eta_{trans}\, g_r} & T_{wh} > 0 \\ \dfrac{T_{wh}\, \eta_{trans}}{g_r} & T_{wh} \leq 0 \quad . \end{cases} \tag{2.9}$$

The transmission has 7 speeds from which follows the constraint

$$1 \leq g \leq 7 \tag{2.10}$$

of the gear g. The electric motor speed ω_{em} depends on the vehicle speed v and the gear ratio g_r

$$\omega_{em} = \frac{v}{r_{wh}\, g_r} \quad , \tag{2.11}$$

while the engine speed ω_{ice} corresponds to ω_{em} when the engine is started and the clutch is closed; otherwise it is 0s^{-1}

$$\omega_{ice} = \begin{cases} 0\text{s}^{-1} & \text{engine off} \\ \omega_{em} & \text{engine on} \quad . \end{cases} \tag{2.12}$$

2.3.1 Combustion Engine

The fuel mass flow $\dot{m}_f$ of the engine is modelled using a measured fuel consumption table of a 1.2-litre, 3-cylinder, naturally aspirated engine with a maximal mechanical output power of 51kW. Using a fuel consumption map f_{fuel}, fuel mass flow $\dot{m}_f$ is a function of engine torque T_{ice} and angular speed ω_{ice} of the engine shaft

$$\dot{m}_f = f_{fuel}(T_{ice}, \omega_{ice}) \quad . \tag{2.13}$$

For simplicity, the engine inertia J_{ice} is not considered. The clutch between engine and powertrain is considered as a switch and the clutch power losses are ignored in this model due to its infrequent operation.

2.3.2 Electric Motor and Inverter

Similar to the engine, power losses in the electric motor are modelled by a measured loss table of the electric motor. Electric motor speed ω_{em} and torque T_{em} are used to determine the electrical losses and thus the electrical power input $P_{inv,AC}$

$$P_{inv,AC} = P_{em} + f_{loss}(T_{em}, \omega_{em}) = f_{em}(T_{em}, \omega_{em}) \quad . \tag{2.14}$$

Considering the inverter efficiency $\eta_{inv} = 0.92$, the electrical power at the battery clamp $P_{inv,DC}$ is

$$P_{inv,DC} = \begin{cases} \dfrac{P_{inv,AC}}{\eta_{inv}} & P_{inv,AC} > 0 \\ P_{inv,AC}\, \eta_{inv} & P_{inv,AC} \leq 0 \quad . \end{cases} \tag{2.15}$$

2.3.3 Battery

Energy losses in the battery of the charging and discharging process are modelled by an internal ohmic resistance R_i, which depends on number and configuration of the battery cells. In the backward model, the chemical battery power P_{bat} is calculated as a function of $P_{inv,DC}$ based on [70]:

$$P_{bat} = \frac{{V_0}^2 - V_0\sqrt{V_0^2 - 4P_{inv,DC}R_i}}{2R_i} \tag{2.16}$$

where R_i is a function of the internal resistance of every battery cell $R_{i\,,cell}$ and their number of in parallel n_p and in series n_s

$$R_i = R_{i\,,cell}\,\frac{n_s}{n_p} \tag{2.17}$$

The stored energy in the battery E_{bat} is a function of P_{bat}. As the backward model is a time discrete model, the change of the battery energy state is described by

$$E_{bat}(k) = E_{bat}(k_0) - P_{bat}\,\Delta t \quad , \tag{2.18}$$

where $\Delta t = 1\text{s}$. The battery model of the forward model is modelled with additional variables of battery clamp voltage $V_{inv,DC}$ and battery current

$$I_{bat} = \frac{P_{inv,DC}}{V_{inv,DC}} \tag{2.19}$$

yielding the mesh rule

$$V_{inv,DC} = V_0 - R_i\,I_{bat} \quad . \tag{2.20}$$

The stored chemical battery energy is

$$E_{bat}(t) = E_{bat}(t_0) - V_0\int_0^t I_{bat}(t')dt' \quad . \tag{2.21}$$

The normalized state of battery energy (SOE) is defined as

$$SOE(t) = \frac{E_{bat}(t)}{E_{bat,nom}} \quad . \tag{2.22}$$

In the following, instead of the SOE the state of charge (SOC) is indicated. The SOC in both models is a function of the battery charge $Q_{bat}(t)$ and the nominal battery charge $Q_{bat,nom}$

$$SOC = \frac{Q_{bat}}{Q_{bat,nom}} \quad . \tag{2.23}$$

The open circuit voltage V_0 of the battery cells is influenced by the SOC and drops by 1.9% comparing a SOC of 0.9 and of 0.3. A lower V_0 leads for the same transferred power to higher currents and thus to higher ohmic losses in the battery. Relationship between stored chemical power and clamp power is depicted in Fig. 2.9. Battery power during vehicle operation is due to its higher efficiency mostly in low power regions in which the efficiency difference is less than 0.002. For simplicity, V_0 is therefore considered constant and not as a function of the SOC. With V_0 assumed to be independent of the SOC, the SOC is equal to the state of energy of the battery:

$$SOC = \frac{Q_{bat}}{Q_{bat,nom}} = \frac{E_{bat}}{E_{bat,nom}} = SOE \quad . \tag{2.24}$$

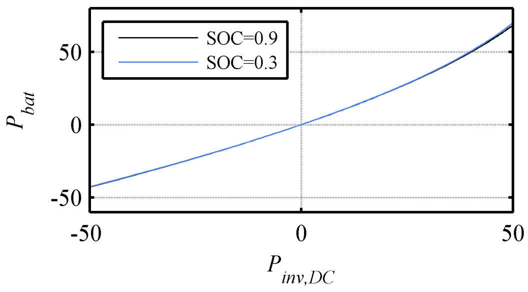

Fig. 2.8. Battery clamp power and chemical power for a SOC of 0.3 and 0.9.

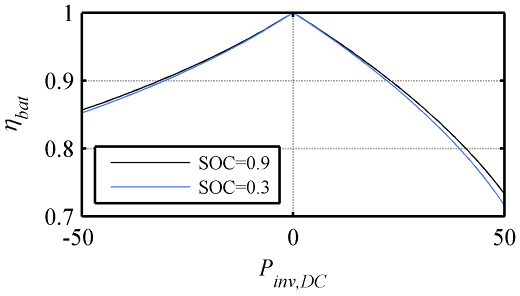

Fig. 2.9. Battery efficiency as a function of its chemical power.

2.4 Quasi-Stationary Linear Model

The proposed EMS calculates as a first step a set point function $SOC^*(t)$ of the necessary constraint for the torque and gear optimization with receding prediction horizon. For calculation of $SOC^*(t)$ mixed integer linear programming (MILP) is employed, which requires a linear vehicle model (Section 4.1). The model of the previous section contains nonlinearities due to the lookup table f_{fuel} of the engine fuel mass flow, the loss lookup table f_{loss} of the electric motor and the transmission ratio. In order to eliminate these nonlinearities, a model of the power transfer in the powertrain is used based on linear descriptions of motor and engine. Such as in the nonlinear backward model, the vehicle speed is equal to the cycle speed. The wheel force F_{wh} is calculated using Eq. (2.5) and the corresponding wheel power is

$$P_{wh} = F_{wh}\, v \quad . \tag{2.25}$$

In order to calculate the mechanical power $P_{req} = T_{req}\omega_{em}$, combined drivetrain and gearbox efficiency η_{trans} is taken into account by

$$P_{req} = \begin{cases} \dfrac{P_{wh}}{\eta_{trans}} & P_{wh} > 0 \\ P_{wh}\,\eta_{trans} & P_{wh} \leq 0 \quad . \end{cases} \tag{2.26}$$

The sign of the power variables are defined as indicated by the arrows in Fig. 2.10.

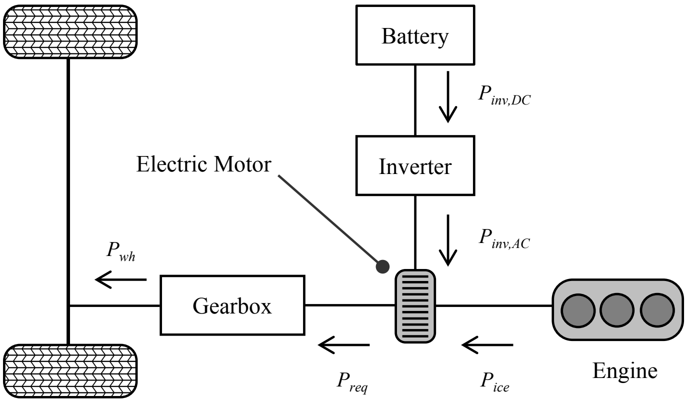

Fig. 2.10. Linear vehicle model variables.

2.4.1 Combustion Engine

To model the fuel mass flow $\dot{m}_f$, from the measured engine fuel consumption table the Willans line is generated [71], which describe fuel rate $\dot{m}_f$ as a function of speed ω_{ice} and mechanical output power $P_{ice} = \omega_{ice}\, T_{ice}$. From the Willans line for different engine speeds a set of linear functions

$$\dot{m}_f = a(\omega_{ice}) + b(\omega_{ice})\, P_{ice} \tag{2.27}$$

is approximated. For simplification, it is assumed that the engine operates at every output power P_{ice} at its highest efficiency, i.e. with minimal fuel consumption. From the linear functions for different engine speeds a convex approximation

$$\begin{gathered} \dot{m}_f(P_{ice}) = \min_i(a_i + b_i P_{ice}) \\ i \in \{1; 2; 3\} \end{gathered} \tag{2.28}$$

is used [54]. The Willans lines for different speeds and the approximation are indicated in Fig. 2.11.

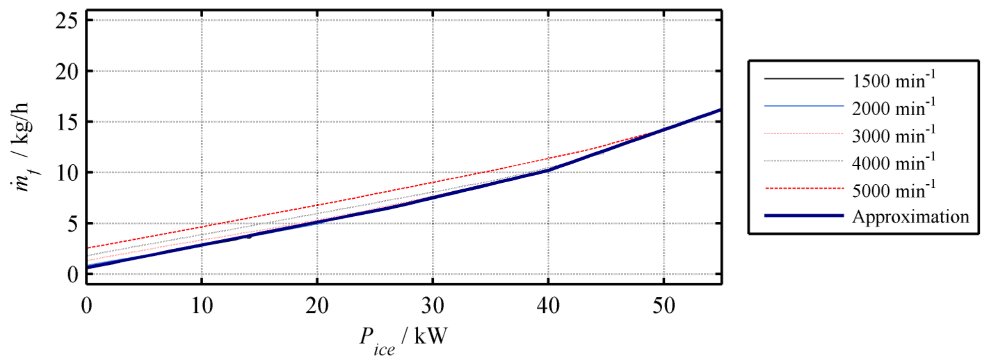

Fig. 2.11. Willans lines of the engine at different engine speeds. The modelled fuel consumption is the approximately the minimum of the Willans lines.

2.4.2 Electric Powertrain Components

The electric machine is modelled by a similar approach as used for the engine model [62], i.e. a set of linear equations. The equation set depends on whether the machine operates in motoring mode $P_{em} = \omega_{em} T_{em} > 0$, (electric mode or boost mode of the vehicle) or in generating mode (charge mode/regenerative braking mode of the vehicle). In motoring mode, the linear power based model is

$$P_{em} = a_{em,mot}(\omega_{em})\, P_{inv,AC} \quad . \tag{2.29}$$

For simplicity, the speed dependence is not considered, such that $a_{em,mot}(\omega_{em})$ corresponds to the approximated electric motor efficiency of $a_{em,mot} = \bar{\eta}_{em}$. The approximation is pictured in Fig. 2.12. In generating mode,

$$P_{inv,AC} = a_{em,gen}(\omega_{em})\, P_{em} \tag{2.30}$$

results (Fig. 2.13). Taking into account the battery efficiency ($\eta_{bat,ch}$ in generating mode and $\eta_{bat,dis}$ in traction mode), defined by

$$\begin{aligned} \eta_{bat,ch} &= P_{inv,DC}/P_{bat} \\ \eta_{bat,dis} &= P_{bat}/P_{inv,DC} \end{aligned} \tag{2.31}$$

and inverter efficiency η_{inv}, the electric system model in motoring mode is

$$P_{em} = a_{em,mot}(\omega_{em})\ \eta_{inv}\, \eta_{bat,dis}\, P_{bat} \quad . \tag{2.32}$$

In generating mode, from Eq. (2.30) results

$$P_{bat} = a_{em,gen}(\omega_{em})\, \eta_{inv}\, \eta_{bat,ch}\, P_{em} \quad . \tag{2.33}$$

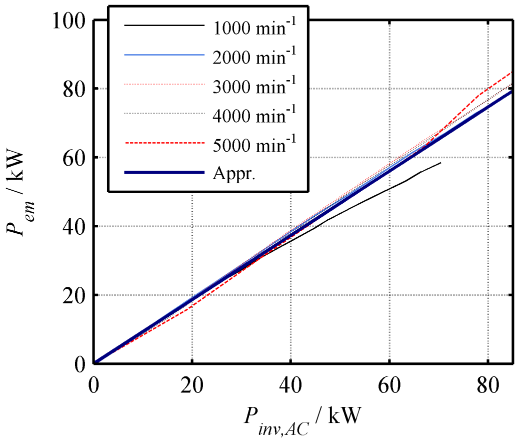

Fig. 2.12. Approximation of the electric machine efficiency in motoring mode ($P_{em} \geq 0$).

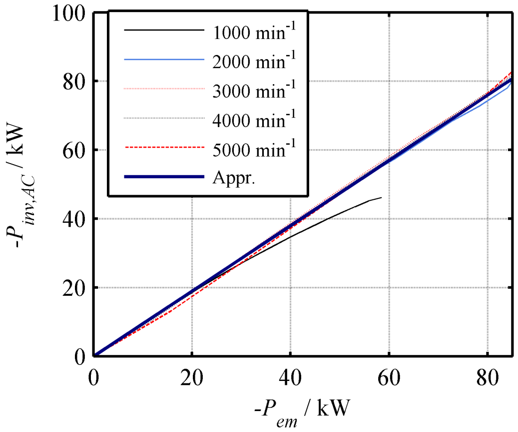

Fig. 2.13. Approximation of the electric machine efficiency in generating mode ($P_{em} < 0$)

2.5 Driving Cycles

To evaluate EMS for PHEV, trip length is an essential factor; a trip being defined trip as a journey made by the vehicle between two recharging stops. For short trips within the all-electric range, the vehicle does not have to use the engine. In this case, the power distribution optimization by the EMS is not necessary. In addition to the trip length, for consumption simulation, the key characteristics of a cycle are traction power and speed. Cycle speed, acceleration and road slope can be summarized by the cycle power P_{cycle} using Eq. (2.8). In addition to its impact on required traction power, cycle speed influences electric motor and engine speed. Another important cycle characteristic is road elevation. The additional traction power required by the potential energy change when driving uphill and the energy generated when driving downhill is an important consideration. For the exemplary vehicle with a mass $m = 1450\text{kg}$ and a driving cycle height difference of $\Delta h_{\Sigma} = 100\text{m}$ results in a potential energy difference of

$$E_{pot} = m\ g\ \Delta h_{\Sigma} = 1{,}422\text{MJ} = 0.395\text{kWh} \quad . \tag{2.34}$$

Therefore, driving cycles used for simulation are chosen in respect of power distribution, road slope and velocity. The slope is either described by the inclination angle α_{road} or the normalized rise Δh (Fig. 2.14).

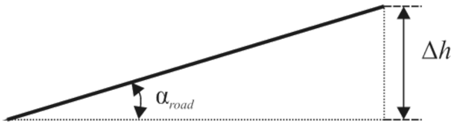

Fig. 2.14. Road slope Δh and angle of inclination α_{road}.

To evaluate CD operation, driving cycles longer than NEDC and FTP-72 cycles are used, as for the exemplary vehicle both are within its electric range. The FTP-72, being a typical real world urban driving pattern with short motorway parts in the USA (Fig. 2.17), is used for CS operation. Due to its short distance of only 12 km and its low power demand, for the exemplary vehicle the cycle is within its all-electric range. This cycle is used to demonstrate the CS capability of the algorithm, which is also a requirement for PHEV, as it cannot always be assured that the battery is charged at trip start. The European official driving cycle NEDC is due its synthetic structure used only for model validation (Section 2.6). The NEDC has periods with constant speed and constant acceleration, which in real driving situations do not occur. For validation, these constant speed phases are very suitable as model and steady state of real components can be compared. For EMS simulation, instead of synthetic driving cycles, real world cycles are used. Real world cycles include more operating points for the powertrain, which is important for evaluation of rule-based strategies, as otherwise there is the risk that it performs well only with the limited number of operating points tested.

In addition to the FTP-72, three other driving cycles which exceed the all-electric range are employed to depict different usage patterns of the vehicles. The challenge is to depict realistic driving cycles on the one hand regarding the vehicle operation at different speed and power, while on the other hand consider length and road elevation. The European Union’s ARTEMIS project [72] led to the development of the CADC (Common Artemis Driving Cycle), which includes realistic accelerations separated into urban, rural and motorway sections.

Driving cycles are selected considering that a common trip driven in passenger cars is from home to work. As for inner city trips the electric range is sufficient, trips from a nearby city are chosen. To simulate a typical trip in a nearby city without motorway connection, the CADC rural section is combined with the urban section. Trips including a motorway section are the recorded driving cycles from Barcelona to a nearby city, e.g. driving cycle BCN-CTS, Fig. 2.15 and its return trip, driving cycle CTS-BCN, Fig. 2.16. In these driving cycles road slope information is also considered, which leads to an additional energy requirement in the case of the BCN-CTS cycle. The very low power demand during the second half of the CTS-BCN cycle caused by low speeds and negative road slope makes the cycle of special interest for CD mode. The cycle characteristics are summarized in Table IV.

Table IV: Simulated driving cycles characteristics.

	BCN-CTS	CTS-BCN	FTP-72	CADC (Rural/Urban)
duration /s	1903	2231	1372	2075
length / km	33.1	33.3	12.0	22.1
$\bar{v}$ / km/h	62.6	53.8	31.4	38.4
v_{max} /km/h	117.4	115.1	91.2	111.5
Δh /m	107.6	138.4	0	0

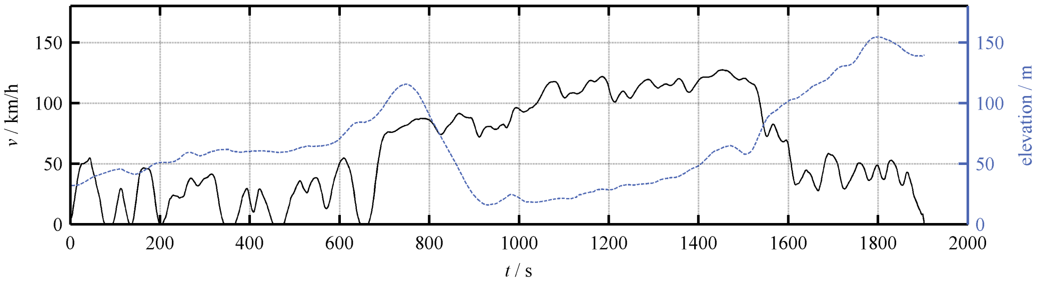

Fig. 2.15. Speed and elevation profile of the driving cycle BCN-CTS.

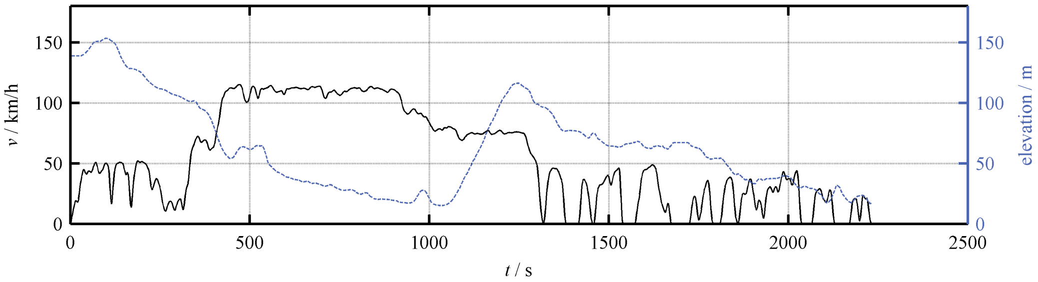

Fig. 2.16. Speed and elevation profile of the driving cycle CTS-BCN.

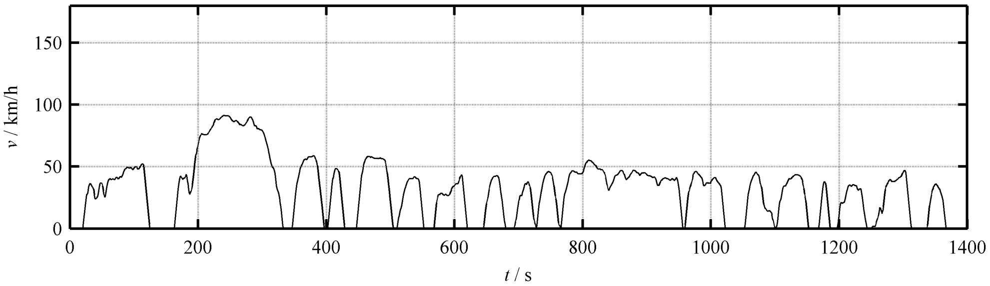

Fig. 2.17. Speed profile of the driving FTP-72 cycle.

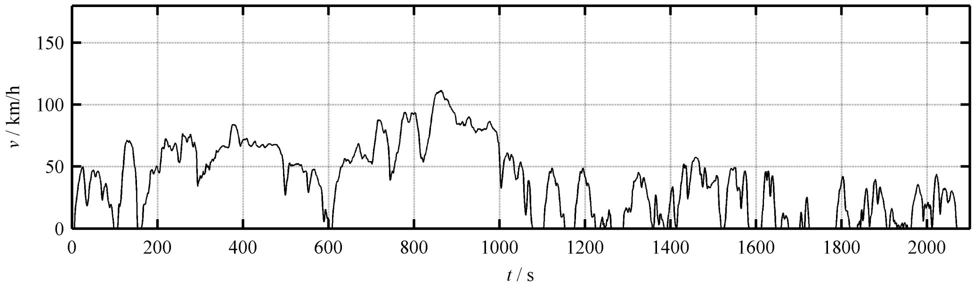

Fig. 2.18. Speed profile of combined rural and urban part of the CADC.

2.6 Model Validation

The used quasi-stationary vehicle model is based on a common approach for vehicle consumption simulation which is described in [62], [73]. Therefore, model validation is not necessary to validate the modelling principle, but to exclude implementation errors. In order to validate the different component models, the nonlinear forward model is compared in terms of fuel consumption and electrical energy consumption to measurements on a hardware-in-the-loop (HIL) engine/electric motor dynamometer and on a chassis dynamometer. The engine/electric motor dynamometer test bench is used for validation of combustion engine, electric motor and inverter models, while the chassis dynamometer is used for validation of gearbox, drivetrain, and vehicle resistance. The nonlinear vehicle forward model is validated against the measurement results, while the backward model and linear vehicle model are validated against this model.

For simplicity, electric motor and combustion engine models are validated separately by adapting the HEV model to a conventional vehicle and an electric vehicle model. In order to validate the electric vehicle model, the clutch between combustion engine and electric motor in the test bench is opened, resulting in the configuration depicted in Fig. 2.26. For validation of the conventional vehicle the clutch is closed, resulting in the configuration of Fig. 2.23. The electric motor remains mounted in the test bench and is considered in the model as an additional inertia and friction element between clutch and drivetrain. In order to validate the remaining components of the powertrain (gearbox, vehicle resistance), offline simulation results of the complete conventional vehicle model are compared to the results from a chassis dynamometer measurement of a complete vehicle (Section 2.6.2).

2.6.1 Test Bench Validation

In order to connect the MODELICA/DYMOLA vehicle model with the test bench for HIL measurements, it is embedded in a SIMULINK model (Fig. 2.19). The model is compiled using MATLAB Real Time Workshop and executed on a dSPACE real time platform. The dSPACE real time platform is based on a DS1006 processor board and has CAN and digital/analogue input/output interfaces. The real time platform communicates with the ECU and the dynamometer load machine through the test bench supervision system (PUMA). Control of clutch and electric motor is handled directly by dSPACE through a CAN connection with the inverter of the electric motor and through a digital signal connection with the clutch (Fig. 2.20). The battery simulator is controlled by a separate control station.

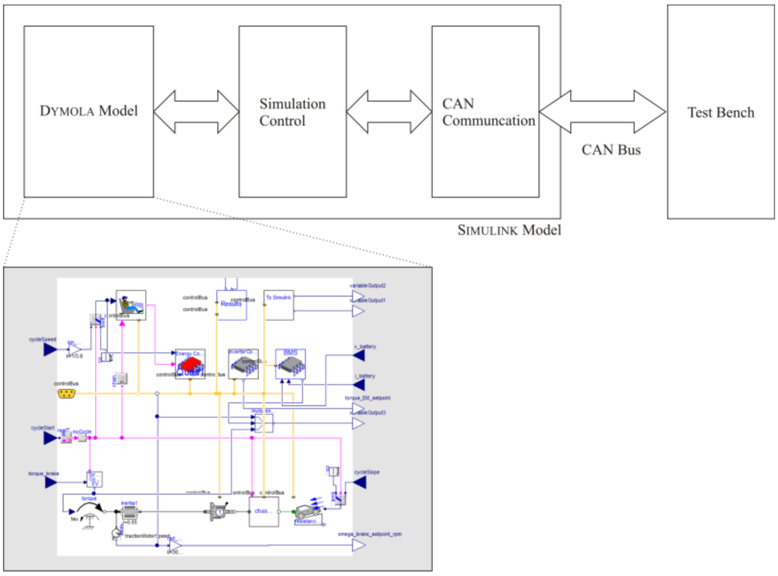

Fig. 2.19. Vehicle model communication with dynamometer test bench.

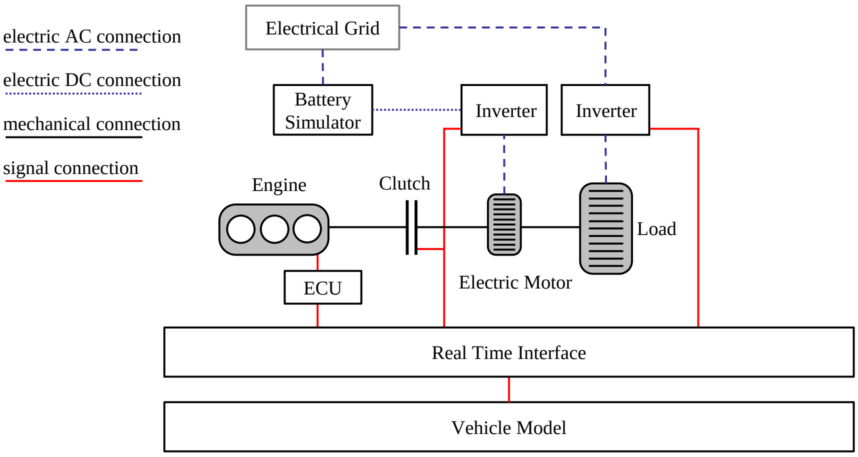

Fig. 2.20. Control structure of the test bench.

The nonlinear forward vehicle model from Section 2.3 is adapted to the respective test bench configuration (conventional or electric powertrain). The respective model of the device under test, i.e. the electric powertrain or the engine, is removed from the vehicle model and substituted with signal connections to the real component mounted in the test bench (see Fig. 2.21 for the conventional powertrain). The engine torque signal T_{ice} measured by the test bench torquemeter is used as model input. The model sends the engine speed set point ω_{ice}^{*} to the load machine and the accelerator pedal position α_{acc} to the engine to control the throttle. In the case of the electric vehicle, instead of α_{acc} the torque requested by the driver T_{req} is sent to the test bench (Eq. (2.4)). Due to its constant speed phases which permit a comparison of model and measurements in steady state, the NEDC driving cycle is simulated (Fig. 2.22). In the following, the measurement results and the offline simulation results are referred to as *HIL* and *offline* respectively.

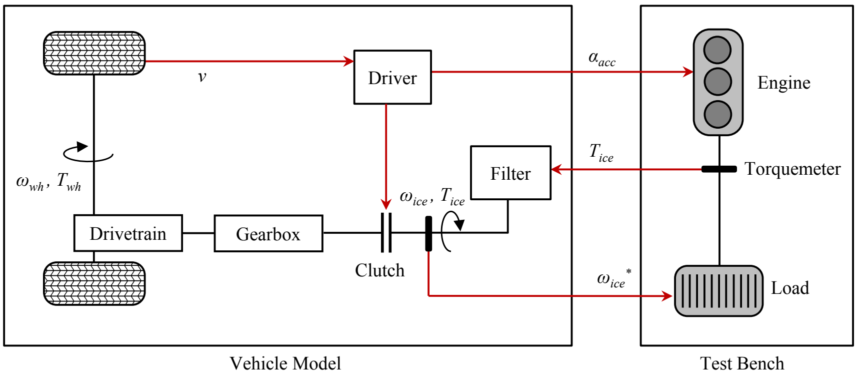

Fig. 2.21. Conventional vehicle model structure for HIL simulation.

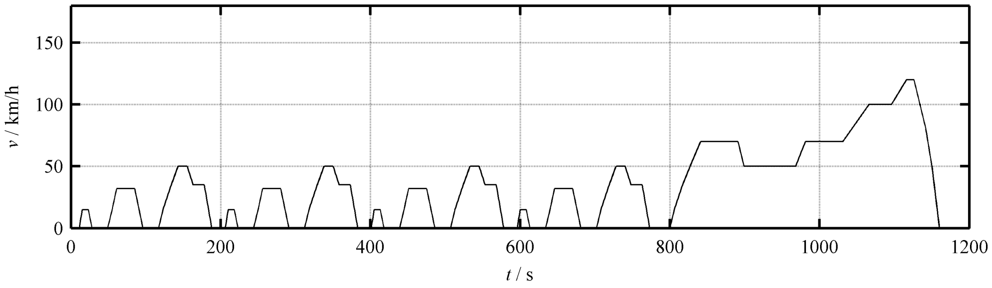

Fig. 2.22. NEDC speed profile.

2.6.1.1 Conventional Powertrain

For validation of the combustion engine model, the engine mounted in the test bench is connected to the powertrain by closing the clutch between engine end electric motor

(Fig. 2.23). Inertia and drag torque of clutch and electric motor are considered in the offline model. For validation, the engine fuel mass flow $\dot{m}_f$ during HIL simulation and the corresponding offline simulation is compared for the urban (Fig. 2.24) and extra urban section (Fig. 2.25). The time axes in the figures indicate the time of the NEDC. As an indicator for the deviation between simulated and measured fuel mass flow, the average absolute error

$$\bar{e}_{abs} = \frac{1}{n}\sum_{i=1}^{n}\left|m_{f,HIL}(i) - m_{f,offline}(i)\right| \tag{2.35}$$

and the root mean square error

$$\bar{e}_{RMS} = \sqrt{\frac{1}{n}\sum_{i=1}^{n}\left(m_{f,HIL}(i) - m_{f,offline}(i)\right)^2} \tag{2.36}$$

are calculated. For the urban section in Fig. 2.24 the average absolute error is $\bar{e}_{abs} = 0.047$g/s and the root mean square error is $\bar{e}_{RMS} = 0.036$g/s. The torque deviation during the urban section stems from the recorded time resolution of the signal. The extra urban section has a higher torque load than the urban part, what results in a higher deviation of fuel consumption with an average absolute error $\bar{e}_{abs} = 0.072$g/s and an average root mean square error $\bar{e}_{RMS} = 0.050$g/s. The NEDC permits, due to its constant speed phases, a direct comparison of consumption at constant engine load points (Table V). During these constant load sections the error decreases with the engine speed. As this operating condition corresponds to the same condition when recording the fuel consumption map of the engine, the difference between measurements and simulation at constant operating points can be partly attributed to a deviation in the real drag torque of the components between torquemeter and engine, i.e. the clutch and the electric motor, and the value introduced in the models. This drag torque is a function of the speed and results indicate that the modelled drag torque underestimates the real component drag torque. As can be seen later, these deviations do not occur with measurements made by the chassis dynamometer.

Table V: Deviation at specific operating points of the engine.

ω_{load}/min^{-1}	T_{load} / Nm	${m_f}_{offline}$ / kg	${m_f}_{HIL}$ / kg	$\Delta {m_f}_{rel}$
1880	28	0.64	0.70	8,6%
2100	21	0.46	0.50	8%
2600	33	0.74	0.79	6,3%

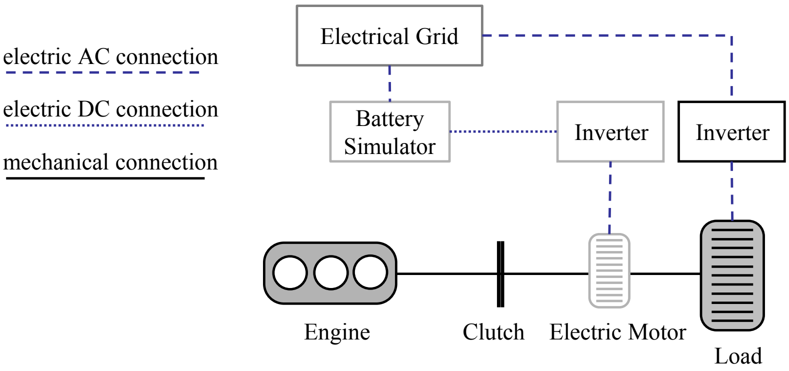

Fig. 2.23. Dynamometer test bench configuration for the conventional powertrain.

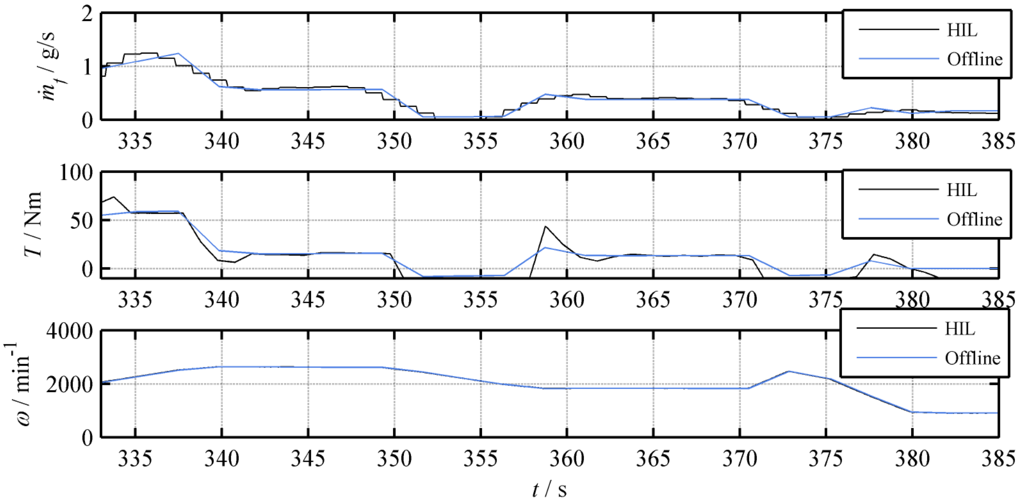

Fig. 2.24. Comparison between HIL measurements of the conventional powertrain and offline simulation results during the urban section of the NEDC.

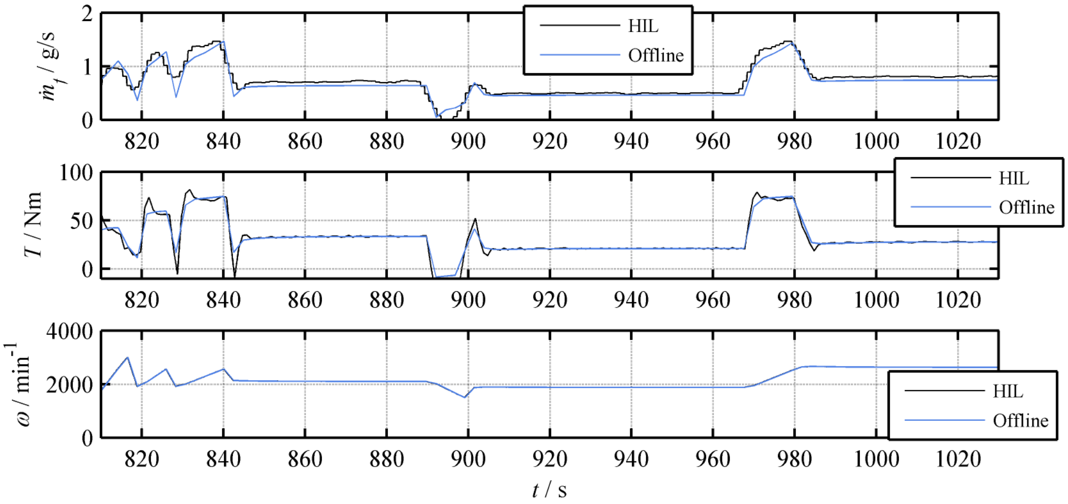

Fig. 2.25. Comparison between HIL measurements of the conventional powertrain and offline simulation results during the extra urban section of the NEDC.

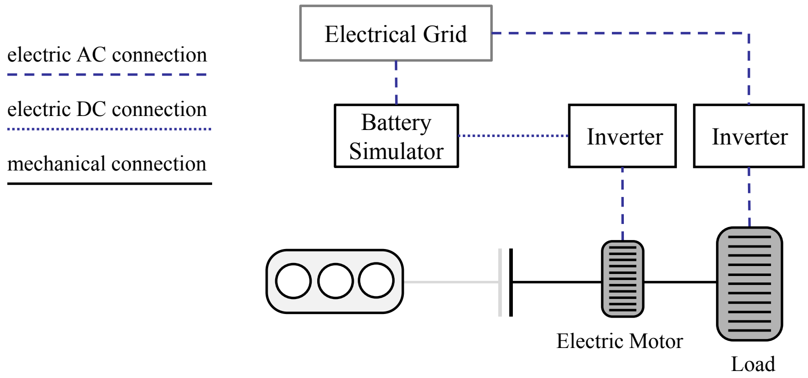

Fig. 2.26. Test bench configuration of the electric powertrain system with the engine decoupled from the powertrain.

2.6.1.2 Electric Powertrain Components

For validation of the electric powertrain components the clutch between engine and electric motor remains open (Fig. 2.26). This test bench configuration corresponds to the powertrain in electric mode of the PHEV and of an electric vehicle. For simplicity, clutch disc inertia has been neglected in the offline simulation. As the motor used in the EMS simulations in the following chapters was not available, HIL measurements are carried out with a different permanently excited synchronous machine with a lower power rating of $P_{em,max} = 50\text{kW}$. For validation, the voltage $v_{inv,DC}$, current $i_{inv,DC}$ and battery clamp power $P_{inv,DC}$ are compared with offline simulation results. Due to restrictions of the experimental electric motor control, only the motoring mode is validated. The battery output voltage $v_{inv,DC}$ of the offline and HIL simulation is set to 300V. The battery simulator maintains the set point to within 1V deviation including at higher load points towards the end of the NEDC (Fig. 2.27 bottom).

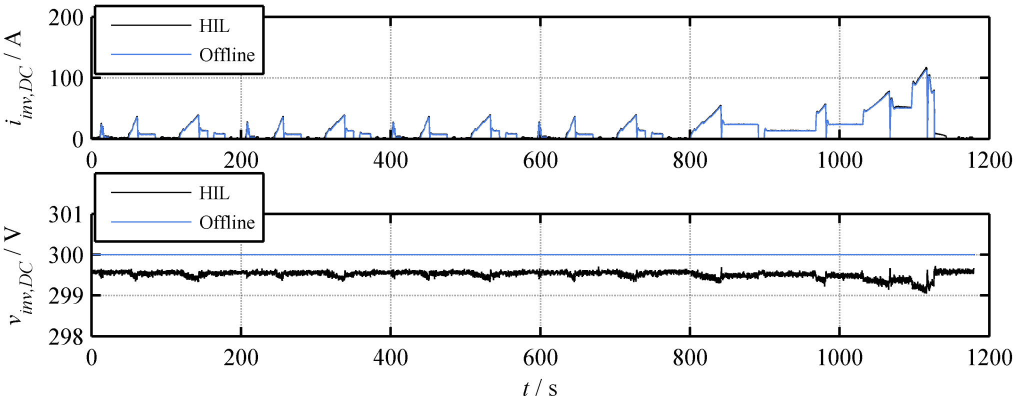

Fig. 2.27. Comparison of output current and voltage of the battery simulator and offline model during the NEDC.

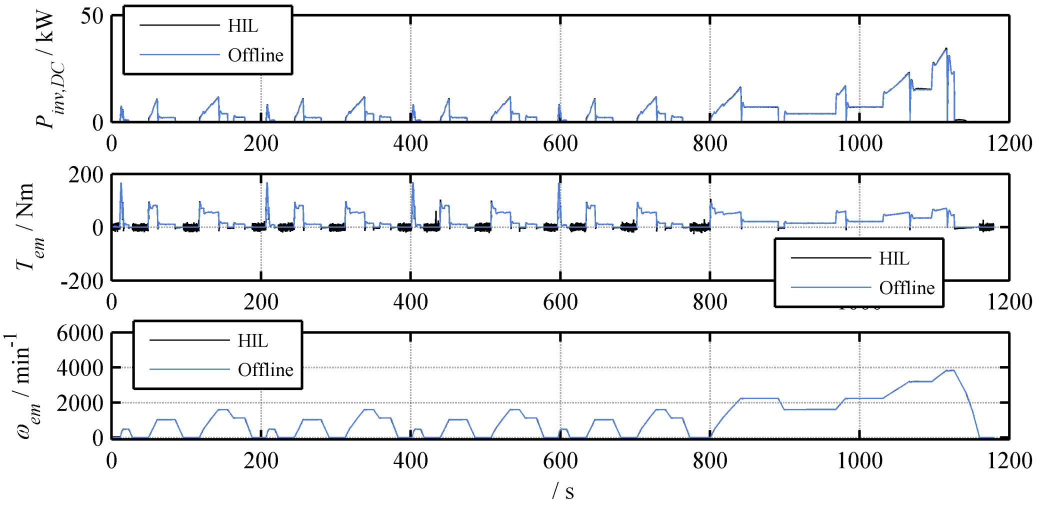

Fig. 2.28. Measured and simulated battery output power $P_{inv,DC}$, electric motor torque T_{em} and electric motor speed ω_{em}.

As deviations in the battery simulator output voltage are below 0.5V in the (Fig. 2.27 bottom), measured output current $i_{inv,DC}$ (Fig. 2.27 above) and output power $P_{inv,DC}$ (Fig. 2.28 above) are proportional. The average absolute error $\bar{e}_{abs}$ is given by

$$\bar{e}_{abs} = \frac{1}{n}\sum_{i=1}^{n}\left|P_{inv,DC,HIL}(i) - P_{inv,DC,offline}(i)\right| \tag{2.37}$$

and the root mean square error by

$$\bar{e}_{RMS} = \sqrt{\frac{1}{n}\sum_{i=1}^{n}\left(P_{inv,DC,HIL}(i) - P_{inv,DC,offline}(i)\right)^2} \ . \tag{2.38}$$

For the NEDC, an average error of $\bar{e}_{abs} = 217.0$W and a root mean square error of $\bar{e}_{RMS} = 123.5$W results. The SOC at end of trip has a deviation of 0.0014 (Fig. 2.29), corresponding to 5.6Wh. This deviation, results in a relative difference of -1.2% of the electrical energy consumption per km (Table VI).

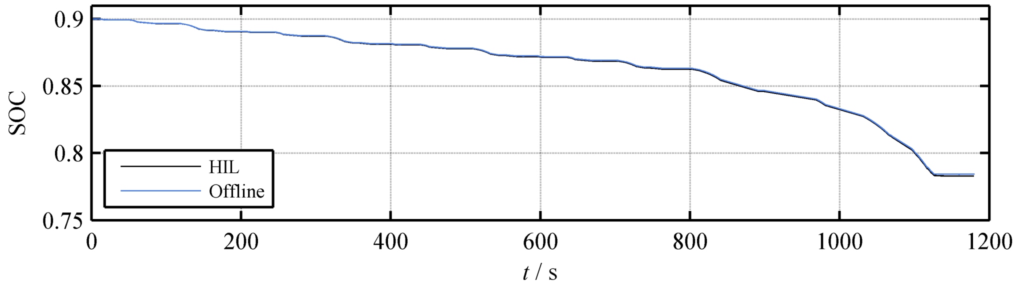

Fig. 2.29. SOC of HIL measurement and offline simulation during NEDC.

Table VI: Average electrical energy consumption of the electric vehicle model for the NEDC.

	HIL	Offline	difference / %
$\Delta E_{bat}/\mathrm{kWh}/100\mathrm{km}$ Total	12.798	12.585	-1.20
$\Delta E_{bat}/\mathrm{kWh}/100\mathrm{km}$ Urban	11.006	10.818	-1.70
$\Delta E_{bat}/\mathrm{kWh}/100\mathrm{km}$ Extra urban	13.750	13.618	-0.96

2.6.2 Chassis Dynamometer Validation

After validating electric system and engine models, the remaining vehicle model components are validated against measurement results from a chassis dynamometer. The front wheels of a complete vehicle are mounted on rollers which are controlled in terms of torque by the chassis dynamometer. The counter torque of the rollers is programmed according to the vehicle resistance. Fuel consumption of the vehicle is measured indirectly by measuring the CO_2 emissions of the vehicle

$$\frac{V_f}{l} = \frac{m_{\mathrm{CO_2}}/\mathrm{kg}}{2.380} \quad . \tag{2.39}$$

CO_2 emissions are collected inside a bag and measured by means of a spectrometer. Therefore, CO_2 gas has to reach the bag to be measured and consequently measured values have a delay and integral behaviour, and cannot directly be compared to the simulated results (Fig. 2.30 left column). The delay depends on the emitted gas volume of the engine, which depends on the load point. Equipment which measures transient emissions by taking into account the integral behaviour and dead times [74] was not available. Therefore, comparison can only be made of the total consumption during a cycle and the value at constant load parts, e.g. during the extra urban cycle section of the NEDC (Fig. 2.30 right column). The vehicle characteristics of the simulation model are adapted to the SEAT Leon used for the measurements (Table VII) for a direct comparison.

Table VII: Test vehicle characteristics measured on the chassis dynamometer.

Gearbox	6 gears, manual
Engine	4cyl, 92kW
Mass	1470kg
Chassis	SEAT Leon passenger car

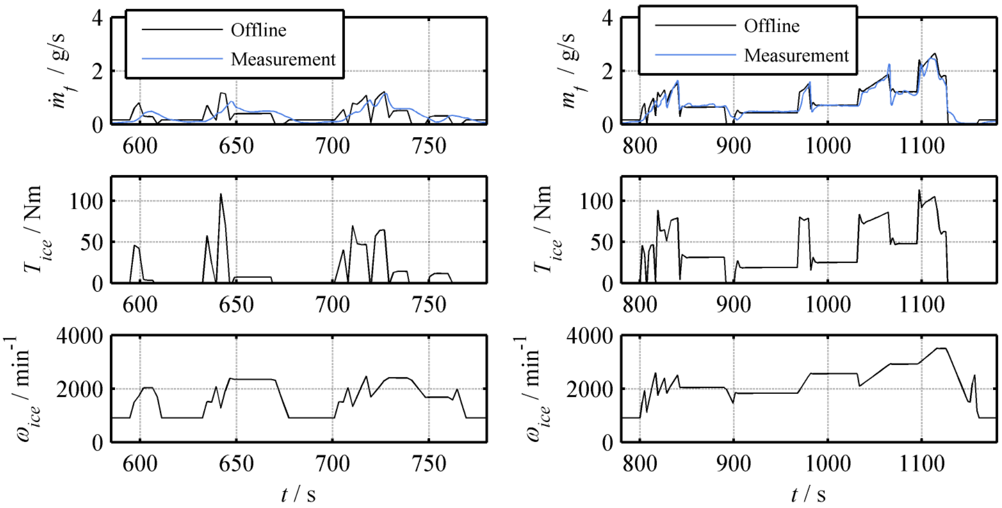

Fig. 2.30. Comparison of simulated and measured fuel mass flow during the fourth urban section and the extra urban section of the NEDC.

At cycle start the engine in the measured vehicle is still at ambient temperature, which leads to higher consumption before nominal operating temperature is reached. Being at operating temperature during the fourth urban cycle section of the NEDC, the fuel mass flow goes down (Fig. 2.31). While the simulated total consumption during the urban part is 8.2% lower than the measured one, during the fourth repetition of the urban pattern it is, by contrast, 1.4% higher. The fuel map in the model is measured with the engine at nominal operating temperature, so comparison must be made with the latter.

The results demonstrate that during the extra urban section the consumption simulation is very accurate for torque values up to 30Nm, while for higher torque demand in the last part of the extra urban cycle, difference in torque increase. This can partly result from using a model with constant gearbox efficiency, while in reality efficiency increases with higher torques. The vehicle resistance on the chassis dynamometer is controlled by a polynomial term as a function of the vehicle speed

$$F_{wh} = c_1 + c_2 v + c_3 v^2 \quad . \tag{2.40}$$

This introduces an additional speed-dependent deviation given by the term $c_2 v$ compared to describing F_{wh} using Eq. (2.5). The mentioned deviation leads to a simulated consumption during the extra urban part which differs by 4.3% from measurement. The last urban part only differs by 0.2%, while due to the cold engine start, the overall urban results differ by -9%.

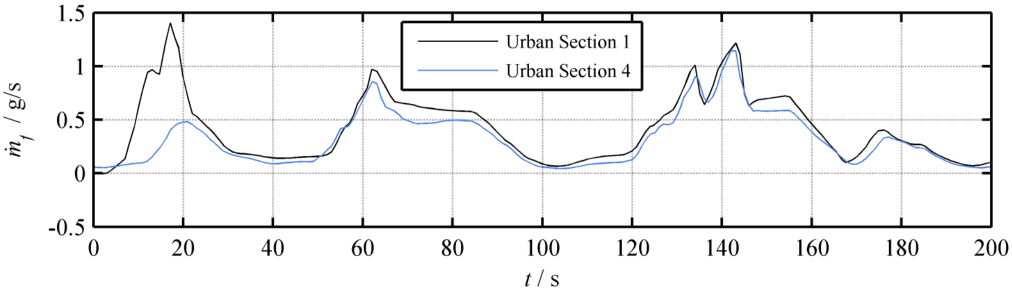

Fig. 2.31. Comparison of measured fuel mass flow on chassis dynamometer during first (engine cold) and fourth urban part (engine warm) of the NEDC cycle.

Table VIII: Comparison of fuel consumption for the NEDC.

	$V_{f,meas}$ / l/100km	$V_{f,offline}$ / l/100km	difference / %
Urban	9.38	8.52	-9.1
Urban (only 4. section)	8.47	8.48	0.2
Extra urban	5.83	6.08	4.3
Total	7.13	6.98	-2.1

3 Predictive Optimization

Predictive optimization in the context of EMS for HEV is the calculation of optimal torque and gear for a known trip. The calculation is therefore based on the assumption that trip forecast data is available. Predictive optimization provides the time-varying function gear g, electric motor power P_{em} and engine power P_{ice} for the future trip. Knowing gear g and vehicle speed, engine and electric motor speed are also known (see Eq. (2.11)) and thus the mechanical power can be calculated using $P = \omega T$. Considering this, it can be seen that control vector

$$\boldsymbol{u}_P(k) = \begin{pmatrix} P_{em}(k) \\ P_{ice}(k) \\ g(k) \end{pmatrix} \tag{3.1}$$

is equivalent the control vector

$$\boldsymbol{u}_T(k) = \begin{pmatrix} T_{em}(k) \\ T_{ice}(k) \\ g(k) \end{pmatrix} \ . \tag{3.2}$$

For parallel powertrain configurations, with Eq. (1.2) the control vector can be simplified to

$$\boldsymbol{u}(k) = \begin{pmatrix} T_{em}(k) \\ g(k) \end{pmatrix} \ . \tag{3.3}$$

The control problem is solved using an algorithm based on a discrete-time dynamic program (DP). As the control problem is time-continuous, a discretization is necessary; however, precise optimization results can be obtained using adequate grid spacing. DP makes possible the use of a control plant model, which is not restricted in terms of linearity or convexity. Furthermore, the model description does not have to be a closed-form expression. One disadvantage of DP, however, is the high computational cost, requiring that measures be taken to reduce the computational load. Due to its global optimal solution finding capability, DP is frequently used for benchmarking purposes – however, it has also been successfully employed for real time use [75]. The algorithm proposed here reduces the computational cost further.

The input values of the DP algorithm are the predicted vehicle speed $v(k)$, vehicle acceleration $a(k)$, road inclination $\alpha_{road}(k)$ and the target SOC at the prediction horizon end $SOC^*(k_p)$. Prediction data is assumed to be accurate. Output values are the engine and electric motor torque and the gear of the control vector $\boldsymbol{u}_T$ (Fig. 3.1).

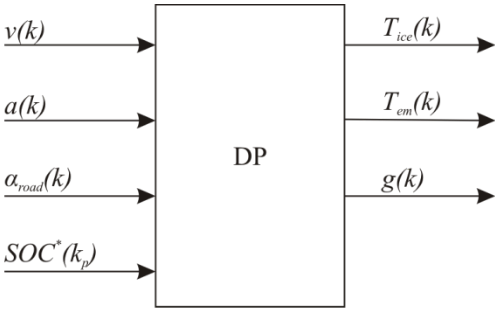

Fig. 3.1. Optimization of torque and gear for a trip (DP input/output).

This chapter introduces in Section 3.1 the basic principle of DP and its implementation for benchmarking purposes. In order to reduce computational cost for real time applications, in Section 3.2 and Section 3.3 an adaptation aimed at accelerating the calculation process is presented. Results of this algorithm applied to a driving cycle are given in Section 3.4.

3.1 Dynamic Programming

Dynamic programming (DP) based algorithms are commonly used to calculate the optimal solution of stochastic or deterministic control problems. Its use for optimal control in HEV for maximal fuel efficiency has been investigated in several publications (e.g. in [76]–[78]), therefore in this section only a short summary of the basic principle is given. DP is based on the optimality principle formulated by Bellman [43], [79]. It states that considering the optimal solution of a problem, every solution of a subproblem also solves this subproblem optimally. With deterministic time-discrete control problems, a shortest path problem [79] results. The computational cost of the shortest path search increases exponentially with the number of states of the optimization problem (model states arise usually from energy stores as inertias or the battery). In order to limit computational cost, the only state (quasi-stationary) backward model employed is the SOC. Even with a single state, computational cost is high compared with algorithms based on quadratic programming (QP) or Pontryagin's minimum principle without additional measures. However, an important advantage of using a time-discrete DP algorithm is more freedom in the area of vehicle modelling, as the model does not have be in closed-form. More importantly, in contrast to approaches based on Pontryagin's minimum principle, it is capable of achieving a defined target SOC at end of the trip.

3.1.1 Algorithm

In the following, calculation is based on the nonlinear backward model described in Section 2.3. In order to simplify notation, the model is described by different functions f_{BW} which are named by the respective model output such that f_{BW,m_f} symbolizes the function for the fuel mass. The functions f_{BW}^{u} thereby describe the backward model as a function of the control vector $\boldsymbol{u}$, while the notation f_{BW} is used for an adaptation which is introduced in the next subsection and uses the control input $\boldsymbol{u}_{\Delta E}$. The discrete system to which the optimization is applied is described by

$$\begin{gathered} x(k+1) = x(k) + f_{BW,x}^{u}\big(\boldsymbol{u}(k), v(k), a(k), \alpha_{road}(k)\big) \\ \text{with} \quad k = 0,1,2,\dots,N \\ \boldsymbol{u}(k) \in U \quad , \end{gathered} \tag{3.4}$$

where $x(k)$ is the state variable and $\boldsymbol{u}(k)$ the control vector at time step k of the set U of all possible control vectors. The control variable $\boldsymbol{u}$ is the control vector from Eq. (3.3) containing the torque of the electric machine T_{em} and the gear g. Using these control variables, the engine torque T_{ice} is indirectly defined by Eq. (1.2) and the engine state by Eq. (1.4). To simplify notation, in this chapter the variable x is used for the battery SOC. The control problem is finding the optimal control sequence

$$\left(\boldsymbol{u}_{\mathrm{i}}^{opt}(x_0)\right) = (\boldsymbol{u}(1), \boldsymbol{u}(2), \dots \boldsymbol{u}(N)) \tag{3.5}$$

from all possible control sequences $\big(\boldsymbol{u}_i(x_0)\big)$ which minimize the general cost function

$$J(x_0) = g_N(x_N) + \sum_{k=0}^{N-1} g_k\big(x(k), \boldsymbol{u}(k)\big) \quad , \tag{3.6}$$

where $x_0 = x(0)$ is the initial system state at time step 0 and $x_N = x(N)$ is the final system state. The term $g_k\big(x(k), \boldsymbol{u}(k)\big)$ defines the cost at time step k as a function of state and control vector. Here the cost function minimizes fuel consumption during the trip,

$$J(x_0) = g_N(x_N) + \sum_{k=0}^{N-1} f_{BW,m_f}^{u}(\boldsymbol{u}(k), v(k), a(k), \alpha_{road}(k)) \quad , \tag{3.7}$$

where $g_N(x_N)$ is a terminal cost of the last state. The application of the optimal control sequence $\big(\boldsymbol{u}_i^{opt}\big)$ results in the minimal value of the cost function

$$J^{opt}(x_0) = \min_{u \in U} J_u(x_0) \quad , \tag{3.8}$$

where Π is the set of all possible control sequences and J_u the sum of the fuel consumption at every time step k when applying the control sequence $(\boldsymbol{u}_i)$. The DP algorithm generally proceeds backward in time, but in deterministic cases it can also proceed forward due to its similarity to a shortest path problem [79]:

$$J^{opt}(x_k) = \min_{\boldsymbol{u}(k)} \left(g_k(x(k), \boldsymbol{u}(k)) + J_{k-1}^{opt}(x(k-1)) \right) \quad . \tag{3.9}$$

In order to achieve the target $SOC^*(N)$, terminal cost is set to

$$g_N(x_N) = \begin{cases} 0 & x_N \geq SOC^*(N) \\ \infty & x_N < SOC^*(N) \quad . \end{cases} \tag{3.10}$$

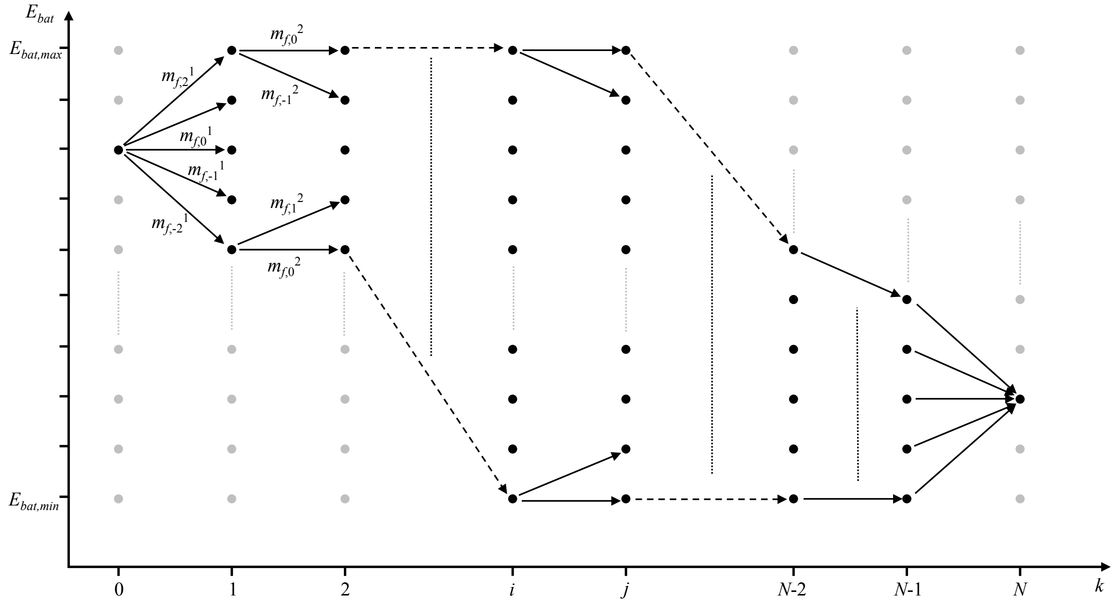

Fig. 3.2. Dynamic programming shortest path search for CD operation. For each time step the transition values $m_{f,t}^k$ are calculated, t being the multiple of the smallest possible state change. Depicted is $E_{bat}(k)$ which corresponds to the state $x(k) = SOC(k)$.

3.1.2 Control Input Adaptation of the Internal Model

In order to use the time-discrete dynamic program, a grid spacing of time and model states (here the SOC) has to be defined. A narrower grid means on one hand higher accuracy, but requires on the other hand more computation time. The SOC grid is defined by defining the grid of E_{bat} by the relationship $SOC \cdot E_{bat,nom} = E_{bat}$. For discretization of E_{bat} a grid spacing of 1kJ is used:

$$E_{bat} = n \cdot 1\text{kJ} \tag{3.11}$$

where $n \in \mathbb{Z}$ such that $E_{bat,min} \leq E_{bat} \leq E_{bat,max}$. For time discretization a spacing of $\Delta t = 1\text{s}$ is used. Considering the grid spacing of time and battery energy, the resulting spacing of the battery power is $\Delta P_{bat} = 1\text{kW}$. Therefore, the resulting average grid spacing of the electric motor power P_{em} is approximately 0.83kW in boost mode (assuming efficiencies of $\eta_{bat} = 0.95, \eta_{inv} = 0.92, \eta_{em} = 0.95$). In regenerative braking mode and charge mode it is about 1.2kW due to the inverse efficiency chain of battery, inverter and electric motor. When applying the control vector $\boldsymbol{u}(k)$ from Eq. (3.3), the resulting battery energy at the next step $E_{bat}(k+1)$ does not necessarily correspond with the grid spacing of E_{bat}. Therefore, the value has to be rounded which causes inaccuracy. In order to avoid this rounding error and to simplify the algorithm implementation, instead of $\boldsymbol{u}$ the control vector ,

$$\boldsymbol{u}_{\Delta E}(k) = \begin{pmatrix} \Delta E_{bat}(k) \\ g(k) \end{pmatrix} \tag{3.12}$$

is used. Using $\boldsymbol{u}_{\Delta E}$ guarantees that the next state $E_{bat}(k+1)$ coincides with the grid. Using ΔE_{bat} as control input, the electric motor lookup table f_{em} from Eq. (2.14) has to be inverted in order to calculate T_{em} as a function of ω_{em} and ΔE_{bat}. The lookup table

$$\begin{gathered} f_{em}\colon (\omega_{em}, T_{em}) \rightarrow P_{inv,AC} \\ \omega_{em}/\text{min}^{-1} \in \{0,100,\dots,6000\} \\ T_{em} \,/\, \text{Nm} \in \{-600,\dots,600\} \end{gathered} \tag{3.13}$$

based on measurement is given. For the calculation of the inverse function ${f_{em}}^{-1}(\omega_{em}, P_{inv,AC})$ the set ω_{em}^{s} is defined as

$$\omega_{em}^{s} \,/\, \text{min}^{-1} = \{10,100,200,\dots,6000\} \quad . \tag{3.14}$$

This set defines the input parameter which f_{em} has in common with its inverse. For every $\omega_{em,i} \in \omega_{em}^{s}$ a corresponding function $f_{\omega_{em,i}}$ can be written as

$$f_{\omega_{em,i}}\colon T_{em} \rightarrow P_{inv,AC} \quad . \tag{3.15}$$

As $f_{\omega_{em,i}}$ monotonically increases for $T_{em} > 0$, the inverse function

$$f_{\omega_{em,i}}^{-1}\colon\ P_{inv,AC,in} \rightarrow T_{em} \tag{3.16}$$

can be interpolated for the new support values of $P_{inv,AC,in}$. Composing the obtained functions $f_{\omega_{em}}^{-1}$ of all $f_{\omega_{em,i}}^{-1}$, the function

$$
\begin{gathered}
T_{em} = f_{em}{}^{-1}(\omega_{em}, P_{inv,AC}) \\
P_{inv,AC} \in P_{inv,AC,in}
\end{gathered}
\tag{3.17}
$$

results. To test the accuracy of the inversion, the function composition

$$
f_{em} \circ f_{em}{}^{-1} \tag{3.18}
$$

is calculated (Fig. 3.5, Fig. 3.3) and the difference $\Delta \mathrm{P}_{inv,AC}$ of output and input values compared (Fig. 3.4). The peaks of the error $\Delta \mathrm{P}_{inv,AC}$ can be disregarded, as they occur in generating mode at low speed with maximum torque. This operating region is not significant for charge mode, as it is below engine idle speed. In regenerative braking mode, $f_{em}{}^{-1}$ is not employed due to using the backward model with f_{em} using Eq. (3.20). Disregarding the peaks, the operating points show an error of $\Delta \mathrm{P}_{inv,AC} < 0.2\mathrm{kW}$ for most operating points. This error is smaller than the maximum possible error of 0.5kJ which can be generated if using the control vector $\boldsymbol{u}(k)$ instead of $\boldsymbol{u}_{\Delta E}(k)$, as the obtained energy change ΔE_{bat} from the vehicle model has to be rounded to the grid spacing defined by Eq. (3.11). Therefore, accuracy increases.

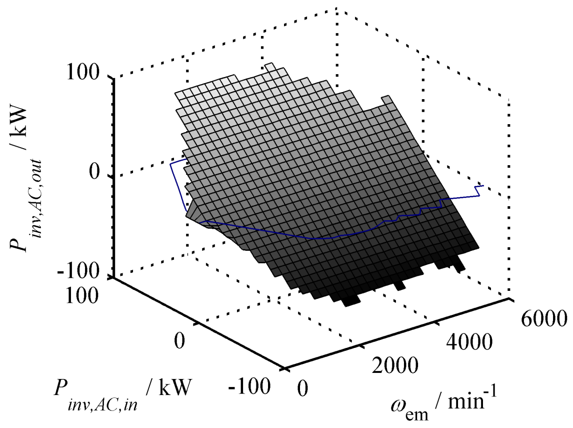

Fig. 3.3. Combination of the electric motor loss table and its inverse. With accurate inversion, the plane $P_{inv,AC,in} = P_{inv,AC,out}$ results.

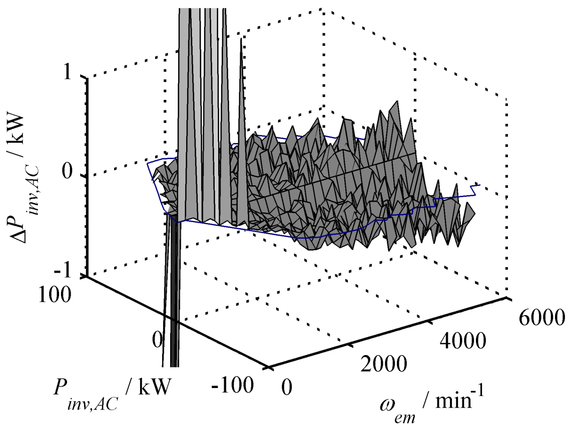

Fig. 3.4. Error $\Delta P_{inv,AC}$ of composition $f_{em} \circ f_{em}{}^{-1}$ (measured table with its inverse).

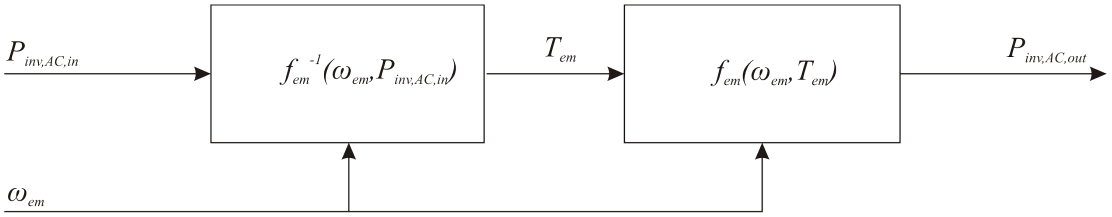

Fig. 3.5. Validation of the inverse 2D lookup table by connecting both tables in series and comparing the input and output value.

The discrete battery energy changes $\Delta E_{bat} = n \cdot 1\text{kJ}$ during one time step (Eq. (3.11)) usually does not coincide with the change $\Delta E_{bat,e-mode}$ when driving electrically. To support electric mode ($T_{ice} = 0$), i.e. to ensure that one value of the discrete points $\Delta E_{bat} = n \cdot 1\text{kJ}$ coincides with electric mode, a displacement

$$E_{bat,shift}(k) = \Delta E_{bat,e-mode}(k) - n_1 \cdot 1\text{kJ} \ , \tag{3.19}$$

where n_1 such that $|E_{bat,shift}| \leq 0.5\text{kW}$, is introduced. With $\boldsymbol{u} = \left(T_{req}, g\right)^T$

$$\Delta E_{bat,e-mode}(k) = \min_{g} f_{BW,\Delta E_{bat}}^{u}(\boldsymbol{u}(k), v(k), a(k), \alpha_{road}(k)) \tag{3.20}$$

results. Using this displacement $E_{bat,shift}$, Eq. (3.11) changes to

$$E_{bat}(k) = n \cdot 1\text{kJ} + E_{bat,shift}(k) \quad . \tag{3.21}$$

This ensures that the grid of $E_{bat}(k)$ at every time step coincides with the change of battery energy when driving electrically. This measure decreases the inaccuracy generated by discretization [38]. For the DP shortest path search algorithm of Eq. (3.9), the corresponding fuel consumption for every energy state change ΔE_{bat} of two subsequent time steps, i.e. the cost $g_k\big(x(k), \boldsymbol{u}_{\Delta E}(k)\big)$, is

$$m_f(\Delta E_{bat}, k) = \min_{g} f_{BW,m_f}(\Delta E_{bat}, v(k), a(k), \alpha_{road}(k), g) \quad . \tag{3.22}$$

The gear and engine and electric motor torque are calculated using

$$g(\Delta E_{bat}, k) = \arg\min_{g} f_{BW,m_f}(\Delta E_{bat}, v(k), a(k), \alpha_{road}(k), g) \tag{3.23}$$

and the engine and electric motor torque using

$$\begin{aligned} T_{ice}(\Delta E_{bat}, k) &= f_{BW,T_{ice}}(\Delta E_{bat}, v(k), a(k), \alpha_{road}(k), g) \\ T_{em}(\Delta E_{bat}, k) &= f_{BW,T_{em}}(\Delta E_{bat}, v(k), a(k), \alpha_{road}(k), g) \quad . \end{aligned} \tag{3.24}$$

Calculating these values, the *cost matrix* and the corresponding control vector of the transitions can be generated and DP algorithm executed (Fig. 3.2). The control sequence $(\boldsymbol{u}_{\mathrm{i}}^{opt})$ obtained by this optimization can be introduced in the forward model for validation of results. In the following, results of applying the optimal control sequence to the forward model simulation, is referred to as global optimum.

3.2 Computational Load Reduction (A-DP)

DP is a generally computational intensive algorithm and thus is often used as benchmark for other real time implementable approaches. Due to its ability to calculate the global optimal solution, in recent years approaches have been presented to increase computation speed for real time implementation. In [80], an optimal set point function $SOC^{*}(t)$ for a trip is calculated using DP (which in this work is obtained by using MILP in Section 4.3). During the trip, an optimization with reduced prediction horizon based on $SOC^{*}(t)$ is executed. Another acceleration method is state space reduction by disregarding SOC states which are not reachable by the shortest path search from the actual $SOC(k)$ and final $SOC(N)$ [45], [50] (i.e. excluding the SOC points which are greyed out in Fig. 3.2). Also in [50] the proposal was made to use a coarser time grid spacing for more distant points of the trip, which could be done in combination with a segmentation of the cycle by road grade or speed changes [81]. This approach is not implemented in this work, as instead a receding prediction horizon (Section 4.5) is used.

In addition to using a receding prediction horizon to accelerate DP, the cost $g(\boldsymbol{u}_{\Delta E}\ )$ of Eq. (3.22), (3.23) is calculated as a function of wheel power P_{wh} and vehicle speed v and stored in lookup tables. The approach of using P_{wh} and v instead of v, a and α_{road} makes the use of lookup tables possible, as otherwise significantly more values have to be stored.

Using lookup tables, the DP algorithm has only to extract the corresponding cost matrix from the lookup tables for a specific trip and execute the shortest path search. Using Eq. (2.5), (2.6), (2.7), (2.8) the vehicle backward model described by $f_{BW}(\Delta E_{bat}, v, a, \alpha_{road}, g)$ can be changed to $f_{BW}(\Delta E_{bat}, v, P_{wh}, g)$. A set of wheel power P_{wh} with a spacing of 1kW

$$\frac{\{P_{wh,table}\}}{\mathrm{kW}} = \{-45, -39, \dots, 0, \dots, 45\} \tag{3.25}$$

and a set of vehicle speed v with a spacing of 1km/h

$$\frac{\{v_{table}\}}{\mathrm{km/h}} = \{0, 1, 2, \dots, 160\} \tag{3.26}$$

are defined. Taking into account the drivetrain and gearbox efficiency, the maximum of $P_{wh} = 45\text{kW}$ corresponds here in ICE mode to the maximum engine power $P_{ice} = 52\text{kW}$. For all combinations (P_{wh}, v) with $P_{wh} \in \{P_{wh,table}\}$ and $v \in \{v_{table}\}$, the minimal fuel consumption is calculated for ΔE_{bat} defined by Eq. (3.11) using

$$m_f(\Delta E_{bat}, v, P_{wh}) = \min_g f_{BW,m_f}(\Delta E_{bat}, v, P_{wh}, g) \tag{3.27}$$

just as the gear by

$$g(\Delta E_{bat}, v, P_{wh}) = \arg\min_g f_{BW,m_f}(\Delta E_{bat}, v, P_{wh}, g) \quad . \tag{3.28}$$

With the gear g from Eq. (3.28) the corresponding torques of the electric motor and the combustion engine are calculated using

$$\begin{aligned} T_{ice}(\Delta E_{bat}, v, P_{wh}) &= f_{BW,T_{ice}}(\Delta E_{bat}, v, P_{wh}, g) \\ T_{em}(\Delta E_{bat}, v, P_{wh}) &= f_{BW,T_{em}}(\Delta E_{bat}, v, P_{wh}, g) \quad . \end{aligned} \tag{3.29}$$

The calculated values of fuel mass flow m_f, gear g, T_{ice} and T_{em} as a function of P_{wh}, v and ΔE_{bat} are saved in lookup tables. The resulting lookup tables are the 3-dimensional arrays $\boldsymbol{F}_{m_f}(\Delta E_{bat}, v, P_{wh})$, $\boldsymbol{F}_{T_{ice}}(\Delta E_{bat}, v, P_{wh})$, $\boldsymbol{F}_{T_{em}}(\Delta E_{bat}, v, P_{wh})$, and $\boldsymbol{F}_g(\Delta E_{bat}, v, P_{wh})$ as indicated in Fig. 3.6. For every pair (P_{wh}, v) the corresponding value $E_{bat,shift}(P_{wh}, v)$ is saved in the 2-dimensional lookup table $\boldsymbol{f}_{E_{bat,shift}}(P_{wh}, v)$. The total number of table elements for the proposed grid defined in Eq. (3.25) and (3.26) is

$$n_{e,\boldsymbol{F}} = 91 \cdot 161 \cdot 119 = 1'743'469 \quad . \tag{3.30}$$

Considering that a total of four tables are necessary, $n_{e,\boldsymbol{F}}$ has to be multiplied by a factor of 4. Including the $91 \cdot 161$ elements of $\boldsymbol{f}_{E_{bat,shift}}$ and saving them in a single precision floating point format which occupies 4 byte per value, a total lookup table size of about 26.6MB results. For use in vehicle onboard units, lookup table size can be significantly reduced using a different variable format. For the gear lookup table $\boldsymbol{F}_g(P_{wh}, v, \Delta E_{bat})$ an entry size of 1 byte instead of 4 byte is sufficient. A further reduction can be achieved by not storing the table entries of $\boldsymbol{F}_{T_{ice}}$, $\boldsymbol{F}_{m_f}$ for $P_{wh} < 0$, as in that driving condition the engine is not used. Additionally, many entries of the tables are empty, such as entries for low vehicle speed, which do not occur in combination with high cycle power.

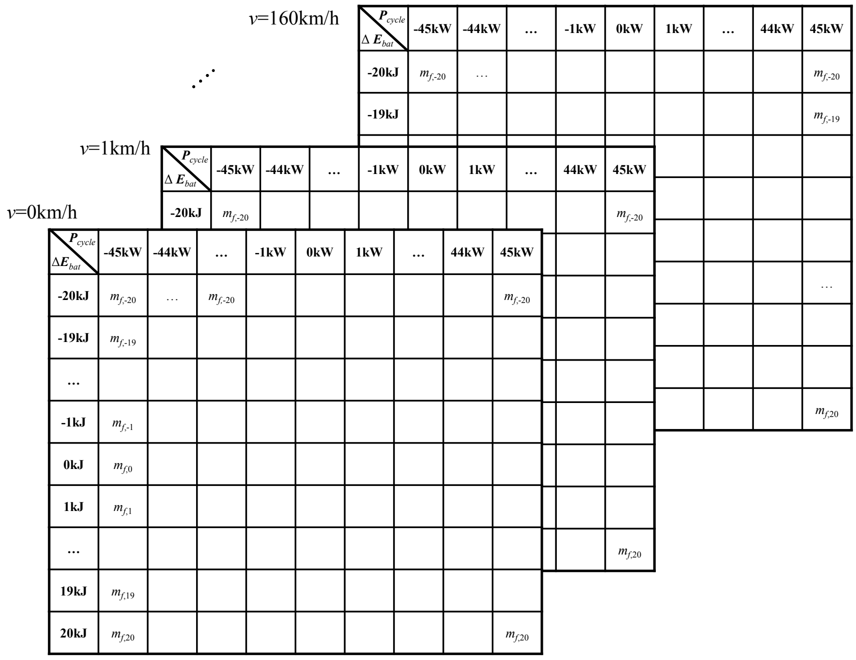

Fig. 3.6. 3-dimensional lookup table array $\boldsymbol{F}_{m_f}$ for the accelerated DP algorithm (A-DP).

3.3 Application for Real Time Implementation

After calculating and saving the lookup tables for a certain vehicle, the precalculated values are used online by the shortest path search. Therefore, in this section the preparation of the optimal cost matrix is described. The cost-to-go matrix describes the cost $g_k(\boldsymbol{u}_{\Delta E}(k)\,)$ for the cycle time steps which are used by the shortest path search.

At first, to take into account the speed v and slope change during two time points k and $k+1$, the cycle speed is averaged by

$$\bar{v}(k) = \frac{v(k)+v(k+1)}{2} \quad . \tag{3.31}$$

Road slope is expressed for averaging by Δh (Fig. 2.14) instead of α_{road}, as the potential energy required is directly proportional to Δh:

$$\overline{\Delta h}(k) = \frac{\Delta h(k)+\Delta h(k+1)}{2} \quad . \tag{3.32}$$

Calculating $\bar{F}_{wh}(k)$ from the values $\bar{v}(k), \overline{\Delta h}(k)$ and $a(k)$ using Eq. (2.5), the wheel power

$$\bar{P}_{wh}(k) = \bar{F}_{wh}(k)\ \bar{v}(k) \tag{3.33}$$

results. To access the lookup tables, $\bar{P}_{wh}(k)$ and $\bar{v}(k)$ are rounded to multiples of 1km/h and 1kW defined by Eq. (3.25) and (3.26):

$$\begin{gathered} v'_{cycle}(k) = \text{round}\left(\frac{\bar{v}(k)}{1\text{km/h}}\right)\text{km/h} \\ P'_{wh}(k) = \text{round}(\bar{P}_{wh}(k)/1\text{kW})\ \text{kW} \quad . \end{gathered} \tag{3.34}$$

The cost-to-go matrix for the shortest path search $\boldsymbol{m_f}$ and the matrices of the corresponding transition values T_{ice}, T_{em}, g are extracted from the respective lookup tables $\boldsymbol{F}_{m_f}$, $\boldsymbol{F}_{T_{ice}}$, $\boldsymbol{F}_{T_{em}}$, $\boldsymbol{F}_g$ as a function of time step and battery energy change:

$$\begin{aligned} \boldsymbol{m_f}(k, \Delta E_{bat}) &= \boldsymbol{F}_{m_f}(P'_{wh}(k), v'(k), \Delta E_{bat}) \\ \boldsymbol{t}_{ice}(k, \Delta E_{bat}) &= \boldsymbol{F}_{T_{ice}}(P'_{wh}(k), v'(k), \Delta E_{bat}) \\ \boldsymbol{t}_{em}(k, \Delta E_{bat}) &= \boldsymbol{F}_{T_{em}}(P'_{wh}(k), v'(k), \Delta E_{bat}) \\ \boldsymbol{t}_g(k, \Delta E_{bat}) &= \boldsymbol{F}_g(P'_{wh}(k), v'(k), \Delta E_{bat}) \quad . \end{aligned} \tag{3.35}$$

The displacement $E_{bat,shift}(k)$ of Eq. (3.19) is extracted from the lookup table $\boldsymbol{f}_{E_{bat,shift}}$

$$E_{bat,shift}(k) = \boldsymbol{f}_{E_{bat,shift}}(P'_{wh}(k), v'(k)) \tag{3.36}$$

which is later adapted to compensate for the rounding error generated by rounding P'_{wh}. To evaluate the effect of the rounding errors generated by Eq. (3.34), error

$$e_P(k) = P_{wh}(k) - P'_{wh}(k) \tag{3.37}$$

and

$$e_v(k) = v(k) - v'(k) \tag{3.38}$$

are defined. The maximal deviation the wheel torque T_{wh}, $e_T = |T_{wh}{}' - T_{wh}|$ caused by $e_P(k)$ is given for $P_{wh} > 0$ by

$$e_{T,max}(v,\ g_r) = \frac{1}{\eta_{trans}\, g_r \frac{v}{r}} 500\text{W} \quad . \tag{3.39}$$

In regenerative braking mode ($P_{wh} < 0$), the error is smaller by the factor η_{trans}^2:

$$e_{T,max}(v,\ g_r) = \max\left|\frac{\eta_{trans}}{g_r \frac{v}{r}}(P'_{wh} - P_{wh})\right| = \frac{\eta_{trans}}{g_r \frac{v}{r}} 500\text{W} \quad . \tag{3.40}$$

The maximal rounding error depends heavily on the gear, as at higher gears the motor torque is translated in a higher wheel torque (Fig. 3.7). Taking into account that high gears are not used in hybrid mode at low vehicle speeds, (gear 7 at a vehicle speed of 50km/h results in $\omega_{ice} = 1170\mathrm{min}^{-1}$) the error exceeds values of 5Nm only for vehicle speeds below 9km/h.

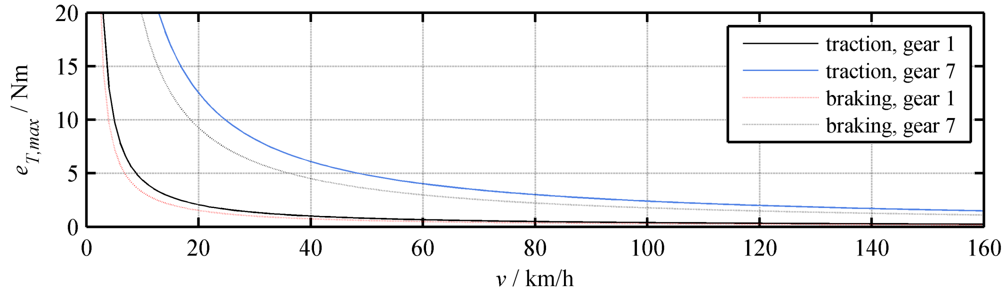

Fig. 3.7. Maximal influence of the rounding error e_P on the torque T_{wh}.

An additional torque error results from $e_v(k)$, whose maximum is for $P_{wh} > 0$

$$e_{T,max}(P_{wh},\ g_r) = \max\left|\frac{P_{wh}}{\eta_{trans}\ g_r}\left(\frac{v - v'}{v\ v'}\right)\right| = \frac{P_{wh}}{\eta_{trans}\ g_r} 0.7\ \cdot 10^{-5} \tag{3.41}$$

In regenerative braking mode ($P_{wh} < 0$), the error is by the factor η_{trans}^2 smaller:

$$e_{T,max}(P_{wh},\ g_r) = \frac{P_{wh}\eta_{trans}}{g_r} 0.7\ \cdot 10^{-5}\ . \tag{3.42}$$

The rounding of v has a smaller effect on the torque error e_T and is negligible as the maximal error is below 0.5Nm (Fig. 3.8). Therefore, only a compensation for the rounding error e_P is introduced.

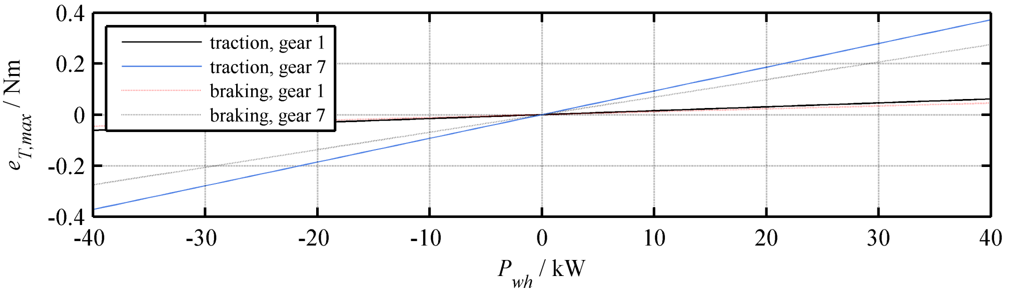

Fig. 3.8. Effect of the rounding error e_v on the torque T_{wh}.

To compensate the effect of e_P on torque and battery energy consumption, a compensation for the electric motor torque T_{em} and the energy offset $E_{bat,shift}$ is calculated which is applied every time step by using average component efficiencies. The effect on the battery energy is approximated by

$$E_{shift,corr}(k) = \begin{cases} E_{bat,shift}(k) + e_P(k)\,\Delta t\,\eta_{trans}\,\tilde{\eta}_{em}\eta_{inv} & P_{wh} < 0 \\ E_{bat,shift}(k) + \dfrac{e_P(k)\,\Delta t}{\eta_{trans}\,\tilde{\eta}_{em}\eta_{inv}} & P_{wh} \geq 0 \end{cases} \tag{3.43}$$

where $\Delta t = 1\text{s}$ is the time grid spacing and $\tilde{\eta}_{em} = 0.8$. The torque T_{em} is corrected by

$$T_{em,corr}(k) = T_{em} + e_P(k)\frac{\eta_{trans}}{\frac{g_r v}{r_{wh}}} \quad P_{wh} < 0 \quad . \tag{3.44}$$

Adapting $E_{shift,corr}$ and $T_{em,corr}$ by Eq. (3.43) and (3.44), achieved results are close to standard DP results from Section 3.1 (Table X, Table XI), but with significantly reduced computational costs.

3.4 Results of the Accelerated DP (A-DP)

The lookup table based accelerated DP (A-DP) algorithm of Section 3.2 is validated with the FTP-72 cycle, employing CS operation, and the BCN-CTS cycle, employing CD operation. The obtained results are compared to the global optimal results obtained by standard DP (S-DP) from Section 3.1. For comparison, the obtained control sequence $(\boldsymbol{u}_{\mathrm{i}}^{opt})$ is applied to the vehicle forward model. The driver model of the vehicle forward model corrects differences between vehicle and cycle speed of the A-DP caused by the rounding error e_T by adjusting T_{em} by means of a PI controller. Rounding errors of the cycle power e_P and speed e_v generated by the lookup tables result in slightly different costs at every time step, despite their correction by Eq. (3.43). The difference in the cost $g_k(\boldsymbol{u}(k))$, i.e. the fuel mass m_f at time steps k, leads to different decisions of the shortest path search algorithm. The torque differences between both algorithms are defined as follows:

$$\begin{aligned} \Delta T_{em} &= T_{em}^{A-DP} - T_{em}^{S-DP} \\ \Delta T_{ice} &= T_{ice}^{A-DP} - T_{ice}^{S-DP} \\ \Delta T_{req} &= T_{req}^{A-DP} - T_{req}^{S-DP} \end{aligned} \tag{3.45}$$

T^{A-DP} being the result of lookup tabled based DP, and T^{S-DP} the result of S-DP. Different decisions of the shortest path algorithm lead to different values for the electric motor torques $T_{em}^{A-DP}(k)$ and $T_{em}^{S-DP}(k)$ of the A-DP and S-DP (Fig. 3.11), and the engine torque (Fig. 3.12). While smaller deviations of ΔT_{em} and ΔT_{ice} can result from the error e_T, the peaks indicate that another control input $\boldsymbol{u}$ is chosen by the shortest path algorithm. This leads to engine starts at different time points as indicated in Fig. 3.9 for the FTP-72 cycle. While at second 43 of the FTP-72 driving cycle only the S-DP algorithm starts the engine, at second 80 only the A-DP algorithm starts the engine. This leads to the peaks of ΔT_{em} in Fig. 3.9. These different decisions do not necessarily have huge impact on the overall results, as already small cost differences can result in the choice of another path through the battery energy states. The same peaks observed during the FTP-72 cycle occur also during the BCN-CTS cycle (compare Fig. 3.11 bottom, Fig. 3.12 bottom).

Differences of ΔT_{req} (Fig. 3.9 bottom) are either caused by a rounding error or by a different gear choice. Therefore, strong deviations of T_{ice} and T_{em} , such as during engine starts can lead, at the same time point, to a peak of ΔT_{req}, as the engine start at second 43 results in the selection of a different gear. The rounding error e_p of the wheel power P_{wh} affects the torque difference ΔT_{req} more at low vehicle speeds than at high vehicle speeds (Fig. 3.10). Between seconds 1450-1500, at a vehicle speed between 119.2 and 127.4km/h, the torque difference $|\Delta T_{req}|$ is smaller than 2Nm. In the cycle section with smaller vehicle speed the torque difference rises shortly to values $|\Delta T_{req}| < 12.6$Nm and changes from second 212 to values $|\Delta T_{req}| < 5$Nm. It must be considered that the effect of the rounding errors e_P and e_v on battery energy level is partly compensated across the cycle, considering the alternating nature of the sign of the error value (Fig. 3.13, Fig. 3.14).

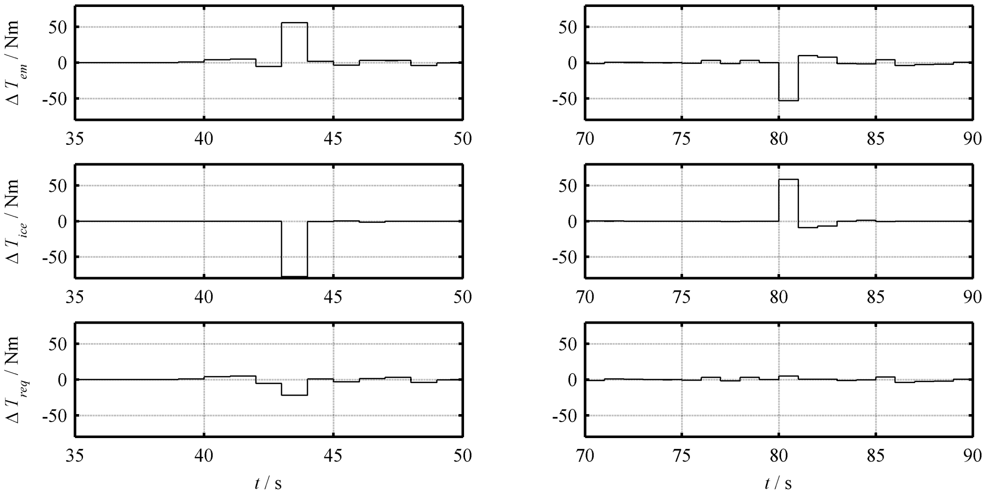

Fig. 3.9. Difference between torque obtained by S-DP and A-DP for the FTP-72 cycle at seconds 35-50 and 70-90.

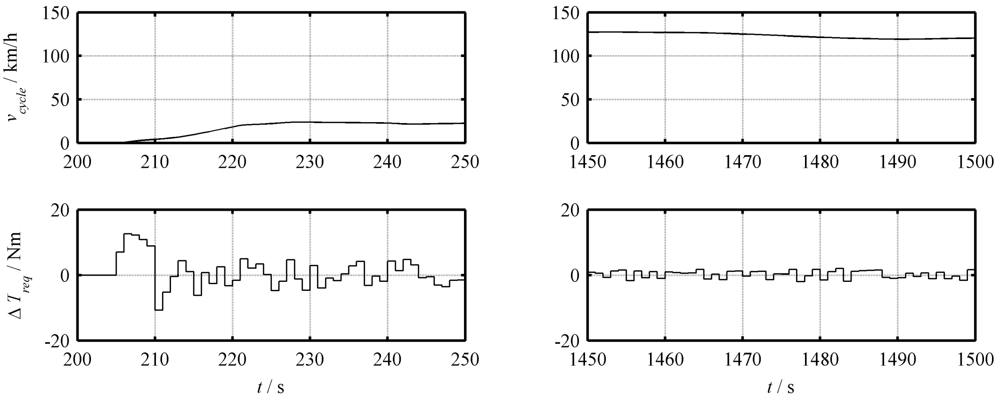

Fig. 3.10. Difference between torque obtained by S-DP and A-DP for the BCN-CTS cycle during seconds 200-250 and 1450-1500.

Using the A-DP algorithm, a drastic reduction in calculation time is achieved. A computation time improvement by a factor of between 49 and 55 is achieved by the A-DP when not considering the calculation time of the lookup tables (Table IX). This is reasonable, as the purpose of the algorithm is for use in vehicle onboard units for real time implementation, and calculation of the lookup tables has only to be executed once for a specific vehicle. The relatively high calculation times of S-DP stem from the implementation of the backward model in Dymola, which is called from the DP algorithm implementation in Matlab. Using the Dymola implementation, calculation time increases on one hand, but on the other hand more complex component models can be used such as lookup table based loss models for gearbox and inverter. Furthermore, A-DP can benefit from improved models without any increase in computation time. A further reduction of the computational cost can be achieved by the reduction of the prediction horizon length [82]. A method using a receding prediction horizon is presented in the following chapter.

Table IX: Calculation times on an Intel i3 (1.8GHz) running Windows x64

	FTP-72	BCN-CTS
S-DP	18906s	44732s
A-DP	387s	808s
Computation time improvement factor	49	55

Evaluating EMS for PHEV is not straightforward when comparing results with different SOC at end of trip. Having consumption of both fuel and electrical energy, as an indicator, consumption weighted against the respective CO_2 emissions is compared. The fuel is weighted against the CO$_2$ emissions when consumed by the engine, while the electrical energy is weighted against the CO$_2$ emitted at the power plant. As electrical energy generation varies considerably between regions, data on the average emissions caused in the EU in 2009 are used (396g/kWh [7]). The resulting CO$_2$ mass is

$$m_{\mathrm{CO}_2} = m_{\mathrm{CO}_2,elec} + m_{\mathrm{CO}_2,f} = \frac{\frac{110\mathrm{g}}{\mathrm{MJ}} \Delta E_{bat}}{\eta_{ch}} + \frac{31.733\mathrm{g}}{\mathrm{kg}} m_f \quad . \tag{3.46}$$

For battery recharging via the electrical grid a charging efficiency $\eta_{ch} = 0.95$ is assumed. The difference of the CO$_2$ emissions per km between standard and A-DP is 0.08% for both the BCN-CTS and FTP-72 cycles (Table X, Table XI). The SOC during the cycles obtained by A-DP is close to the results achieved with S-DP (Fig. 3.13 and Fig. 3.14). The SOC at the end of trip is close to the S-DP, reaching a final SOC of 0.299 for the BCN-CTS cycle and 0.298 for the FTP-72 cycle and thus the electrical energy consumption is slightly higher. The difference in the results of the S-DP applied to the forward model (compare Table X, Table XI) stem from the discretization of the change of the energy levels at every step and the discrete time steps (Fig. 3.2), and can be reduced by a finer grid spacing of time and battery energy level.

Table X: Simulation results for the BCN-CTS cycle.

	S-DP	A-DP	difference / %
SOC_{end}	0.3007	0.2988	-
V_f / l/100km	3.35	3.35	0.03
ΔE_{bat} / kWh/100km	7.249	7.264	0.20
m_{CO_2} / g/km	108.0	108.1	0.07

Table XI: Simulation results for the FTP-72 cycle.

	S-DP	A-DP	difference / %
SOC_{end}	0.2999	0.2979	-
V_f / l/100km	3.63	3.62	-0.22
ΔE_{bat} / kWh/100km	0.005	0.071	-
m_{CO_2} / g/km	87.5	87.6	0.07

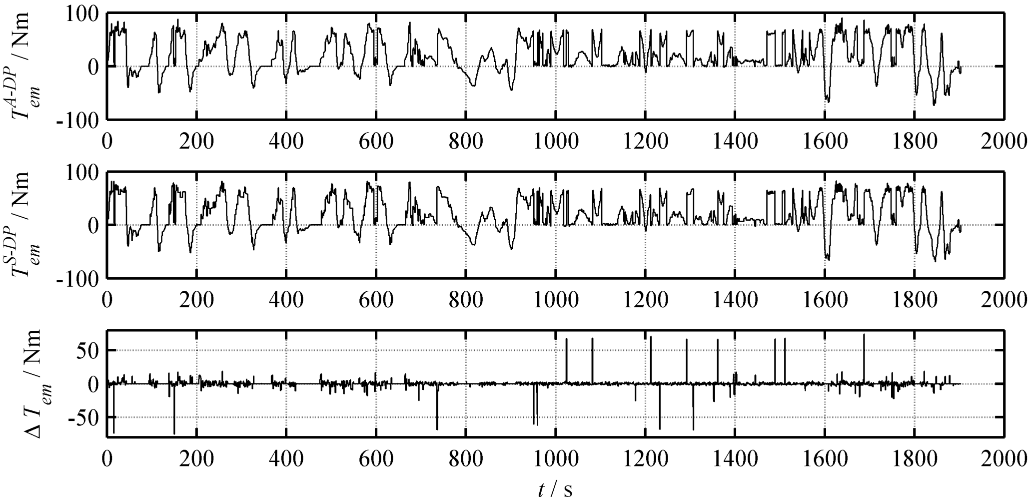

Fig. 3.11. Electric motor torque T_{em} obtained by A-DP (above), S-DP (middle) and the difference ΔT_{em} (bottom) during the BCN-CTS cycle.

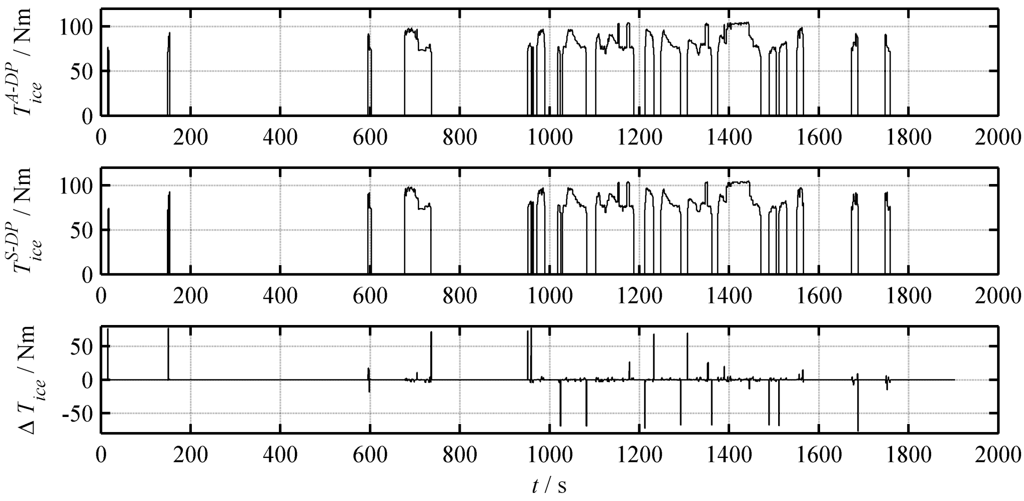

Fig. 3.12. Engine torque T_{ice} obtained by A-DP (above), S-DP (middle) and the difference ΔT_{ice} (bottom) for the BCN-CTS cycle.

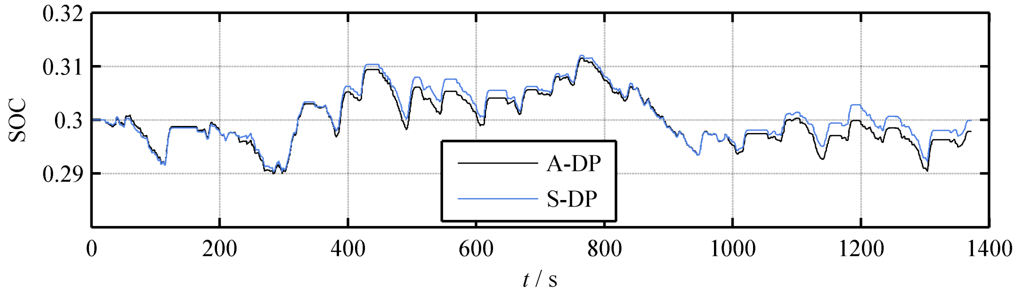

Fig. 3.13. SOC during driving cycle FTP-72 obtained by S-DP and A- DP.

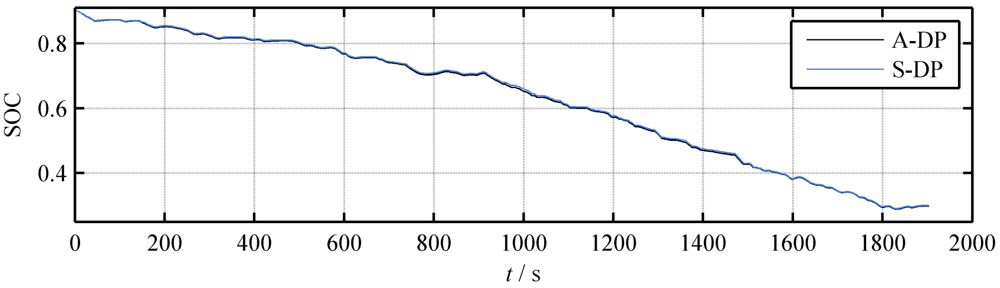

Fig. 3.14. SOC during driving cycle BCN-CTS obtained by S-DP and A-DP.

3.5 Conclusions

DP algorithms have been already employed with success in various publications. Due to the high computational cost of the DP algorithms, they are typically either employed offline for benchmarking purposes or online for HEV with a small energy store and CS operation. The computational cost of DP is reduced considerably by a small energy store and CS operation due to the relatively short prediction horizon, and the fewer battery energy states which need to be considered by the algorithm.

For online EMS, a reduction in computational cost is achieved by using less complex closed-form models. In order to decouple model complexity and accuracy from computational cost, a lookup table based algorithm for DP is proposed. The lookup tables are calculated once for a specific vehicle configuration. To reduce calculation time, the proposed algorithm combines the use of lookup tables with known approaches such as state space limiting. The main task of the DP algorithm is execution of the shortest path search, while lookup tables are used to obtain the required cost g_k. As such, the proposed algorithm is considerably faster than a standard DP. Calculation time is reduced by a factor of 49, and by a factor of 55 for the FTP-72 and BCN-CTS cycles respectively.

As the use of lookup tables generates rounding errors, these errors are compensated for online when applying the extracted lookup table values. Using this compensation, simulation results are close to standard DP. Fuel consumption deviation is 0.22% for the FTP-72 cycle and 0.03% for the BCN-CTS cycle. Deviation of CO_2 emissions is 0.07% for both cycles. The reduction in computational cost achieved by the proposed algorithm is not affected by the complexity of the vehicle model. As such, more precise stationary loss models for electric motors, combustion engines, inverters and transmissions can be used. As the calculation time for DP algorithm shortest path search increases exponentially with prediction horizon length, to further reduce calculation time the algorithm is used within an MPC framework with a receding prediction horizon in the following chapter.

4 Implementation of a Receding Prediction Horizon

For PHEVs to achieve highest fuel efficiency, full battery depletion must coincide with end of trip. The most fuel efficient method for operating in charge-depleting (CD) mode is to employ a predictive EMS using a blended strategy (compare Section 1.3). However, while potential fuel saving increases with predictive strategies, this does cause a considerable increase in computational load. For predictive real time implementable EMS, it is therefore desirable to use a prediction horizon which is shorter than the total trip length. Therefore, in this chapter the implementation of a receding prediction horizon inside a model predictive control (MPC) framework is proposed.

When using an MPC framework as indicated in Fig. 1.21, the optimization process is repeated several times during the trip with a reduced prediction horizon length. For every optimization process the SOC constraint of the end of the prediction horizon has to be known. This is especially important for CD operation, as the SOC during the trip changes considerably. Optimizing with a prediction horizon which includes the entire trip, the resultant SOC value is $SOC^*(k_N) = 0.3$. Using instead a receding prediction horizon, the constraint value is unknown and has to be determined before starting the trip by calculating a SOC set point function for the whole trip (Fig. 4.1). The resultant function is highly determining in the fuel economy of the vehicle.

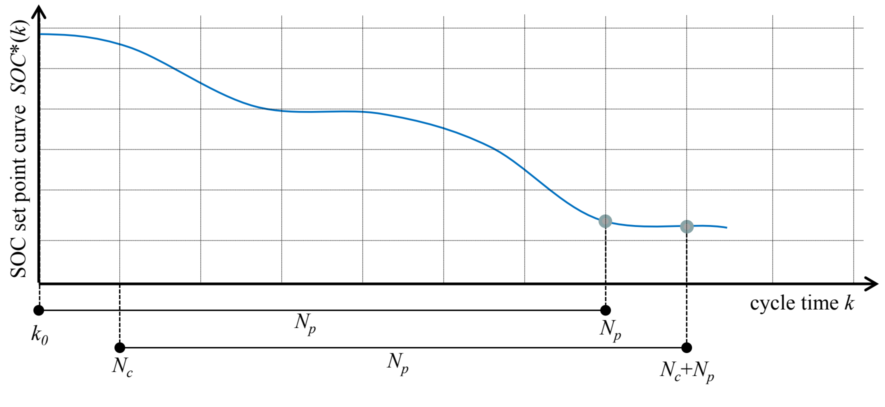

Fig. 4.1. Exemplary set point function $SOC^*(k)$ *for optimization using a receding prediction horizon.*

Due to the condition that this set point function has to be calculated for the entire trip, the algorithm presented in Chapter 3 cannot be employed as the computational load would be too high. Instead, a different optimization based on a simpler vehicle model is proposed, which does not consider torques and gear, but only the power flow between the components. This optimization is performed using a MILP algorithm which calculates the optimal $SOC^*_{MILP}(k)$ for the trip using the available prediction data. The function SOC^*_{MILP} is used to set the final SOC constraint for the optimization of gear and torque by DP Eq. (3.10)

$$x(N) = SOC^*_{MILP}\left(k_0 + N_p\right) \quad . \tag{4.1}$$

where k_0 is the start time of the optimization process and N_p is the prediction horizon length. In such a way the prediction horizon can be reduced significantly, whilst still achieving results close to minimal fuel consumption. It is assumed that trip prediction data for vehicle speed and road grade is available to the EMS.

4.1 Mixed Integer Linear Programming

Mixed integer linear programming (MILP) is an extension of linear programming (LP) [83], both being subclasses of convex optimization problems [84]. MILP permits in addition to continuous variables also the use of integer variables as part of the optimization problem. This is important for the powertrain model of HEV, as the engine state (on and off) influences considerably fuel consumption and cannot be described by continuous variables. As its state is binary, it can be expressed by an integer variable with upper and lower bound. An approach using LP for a series HEV is presented in [54] and an algorithm using MILP for torque optimization disregarding the gear in [55]. The to LP related quadratic programming (QP) is used in [45] for a non-predictive strategy and in [42] for optimizing the power weighting factor (compare Section 1.4). A MILP is described similar to a LP by [85]:

$$\begin{aligned} \text{minimize} \quad & (\boldsymbol{c}_1^T \boldsymbol{x}_1 + \boldsymbol{c}_2^T \boldsymbol{x}_2) \\ \text{subject to} \quad & \boldsymbol{A}_1 \boldsymbol{x}_1 + \boldsymbol{A}_2 \boldsymbol{x}_2 \leq \boldsymbol{b} \\ & \boldsymbol{x}_1 \geq \boldsymbol{0} \\ & \boldsymbol{x}_2 \geq \boldsymbol{0} \quad , \boldsymbol{x}_2 \in \mathbb{N}_0 \quad . \end{aligned} \tag{4.2}$$

In this formulation $\boldsymbol{x} = (\boldsymbol{x}_1, \boldsymbol{x}_2) = (x_1, x_2, \dots, x_n)$ is an *n*-dimensional column vector of nonnegative variables, $\boldsymbol{c}$ is an *n*-dimensional column vector, $\boldsymbol{A}$ is a $m \times n$ matrix, and $\boldsymbol{b}$ is an *m*-dimensional column vector. The constraints $\boldsymbol{A}_1 \boldsymbol{x}_1 + \boldsymbol{A}_2 \boldsymbol{x}_2 \leq \boldsymbol{b}$ define a *feasible region* of $\boldsymbol{x}$. This kind of optimization problem is known as *constraint problem* [83].

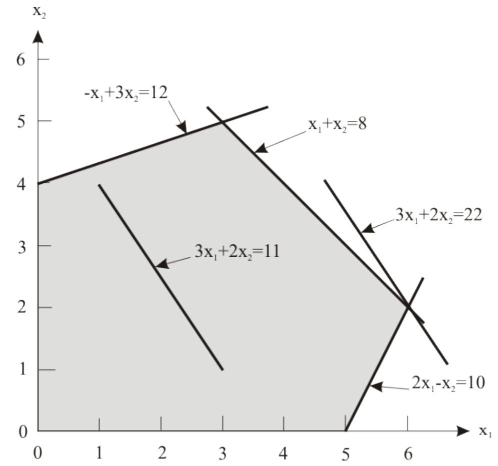

Fig. 4.2. Example of a set of feasible solutions with level sets of the objective function ($3x_1+2x_2$) [86].

In respect to the number of elements of $\boldsymbol{x}$ three classes of problem sizes are distinguished: the small-scale problem with five or less variables, the intermediate–scale problem and the large-scale problem with a hundred or more variables. The problem arising from the EMS optimization is, following this classification, a large-scale problem. In order to solve a MILP problem, it is firstly converted into the LP problem

$$\begin{aligned} \text{minimize} \quad & \boldsymbol{c}^T\boldsymbol{x} \\ \text{subject to} \quad & \boldsymbol{A}\boldsymbol{x} \leq \boldsymbol{b} \\ & \boldsymbol{x} \geq \boldsymbol{0} \end{aligned} \tag{4.3}$$

for which a variety of different solvers exist. A frequently used algorithm to solve the LP problem is the simplex algorithm, which cause especially for large-scale problems high computational costs. Some more recent methods, which are more appropriate for solving large-scale problems, are the *interior-point methods*. The interior-point methods are based on concepts of nonlinear programming techniques [83] and are a class of different methods, of which an important subclass are the path following methods. The methods are based on a reformulation of the original LP problem into a *barrier problem*

$$\text{minimize}\; c^T\boldsymbol{x} - \mu \sum_{j}^{n} \log x_j \quad , \tag{4.4}$$

which corresponds for $\mu = 0$ to the original problem. For $\mu \rightarrow \infty$ the function approaches the boarder of the feasible region, thus defining a path called *central path* (Fig. 4.3). A path following algorithm is an iterative search algorithm and updates the current solution $\boldsymbol{x}_k$ by finding a way through the interior of the feasible region by using an approximation p of the path direction [86]:

$$\boldsymbol{x}_{k+1} = \boldsymbol{x}_k + p(\boldsymbol{x}_k, \mu_k) \tag{4.5}$$

where μ_k is the interior path parameter selected by the algorithm.

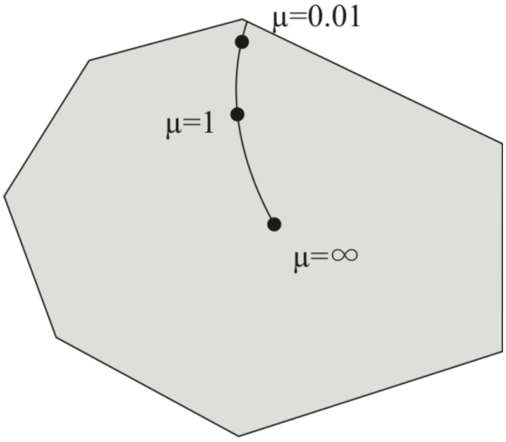

Fig. 4.3. Interior path of path following method [86].

For MILP problems, the vector $\boldsymbol{x}_2$ containing the integer variables increases the complexity of the problem. Solving a MILP problem is done by a *LP-relaxation* of the problem, i.e. the integer constraint of $\boldsymbol{x}_2$ is in a first step disregarded. The obtained LP problem of the relaxation is then computed using the path following algorithm, considering the integer variables $\boldsymbol{x}_2$ continuous. The *cutting plane algorithm* permits the search for an integer solution by adding to the LP-relaxation additional constraints which are only fulfilled by integer values. For higher efficiency, the cutting plane algorithm is combined with a method known as *branch-and-bound*. When the solution of the LP problem does not fulfil the condition that all elements of $\boldsymbol{x}_2$ are integer values, the algorithm creates two new subproblems of the original, which exclude the obtained solution by additional constraints. That is, if the solution for $\boldsymbol{x}_2$ yields e.g. $\boldsymbol{x}_2 = 9.4$, the two new subproblems have as constraint

$$\begin{aligned} &\text{subproblem 1:} \quad \boldsymbol{x}_2 \leq 9 \\ &\text{subproblem 2:} \quad \boldsymbol{x}_2 \geq 10 \quad . \end{aligned} \tag{4.6}$$

These two subproblems are two new branches and are subsequently solved and are split in new subproblems. In this manner a tree structure with advancing limitation of the solution set results. The name part *bound* results from the fact that the solution of a relaxation is a lower bound of the problem:

$$\min\{\boldsymbol{c}_1^T\boldsymbol{x}_1 + \boldsymbol{c}_2^T\boldsymbol{x}_2 | \boldsymbol{x}_1, \boldsymbol{x}_2 \in \mathbb{R}\} \leq \min\{\boldsymbol{c}_1^T\boldsymbol{x}_1 + \boldsymbol{c}_2^T\boldsymbol{x}_2 | \boldsymbol{x}_1 \in \mathbb{R}, \boldsymbol{x}_2 \in \mathbb{N}_0\} \quad . \tag{4.7}$$

By using the bound Eq. (4.7), branches of subproblems can be cut and the complexity of the problem reduced. A detailed description can be found e.g. in [85]. In this work, a solver using the combination of both branch-and-bound and cutting plane algorithm is employed, known as *branch-and-cut* algorithm. The integer condition of the state variable therefore adds additional complexity to the problem compared to programs with only continuous variables, but the efficient LP-solvers still permit the computation of the EMS optimization within a few seconds on a typical desktop computer.

4.2 Optimization Problem Formulation

A MILP requires a linear problem formulation. Therefore, the vehicle description can either include engine and motor torque or the gear. Relation between angular wheel speed ω_{wh} and electric motor speed ω_{em}

$$\omega_{em} = g_r \, \omega_{wh} \tag{4.8}$$

as well as the corresponding torques (being $\eta_{trans} = 1$)

$$T_{em} = T_{wh}/g_r \tag{4.9}$$

is due to the non-constant gear ratio g_r nonlinear. The same nonlinear relation, as in Eq. (4.8) exists for the engine, as electric motor and engine are mounted on the same shaft. One solution could be excluding the gear from the optimization problem, as performed in [55]. Considering that in this work the gear is included in the optimization problem, here the power based powertrain model from Section 2.4 is instead used. Using the power based model, with $P = T\omega$, the nonlinear Eq. (4.8) and (4.9) result (again for $\eta_{trans} = 1$) in

$$P_{em} = P_{wh} \quad . \tag{4.10}$$

Therefore, gear, angular speed and torque do not form part of the MILP (Section 2.4). By the additional constraint

$$0 \leq \boldsymbol{x}_2 \leq 1 \tag{4.11}$$

the integer variable corresponds to a binary variable defined as

$$\boldsymbol{x}_2 = \begin{cases} 0 & \text{false} \\ 1 & \text{true} \end{cases} \quad . \tag{4.12}$$

In such a way, the binary variable s_{ice} refers to the engine state

$$s_{ice}(k) = \boldsymbol{x}_2 = \begin{cases} 0 & \text{engine off} \\ 1 & \text{engine on} \end{cases} , \tag{4.13}$$

where k is a discrete time point with a step width of 1s. As all elements $(x_1, x_2, \dots, x_N)$ of $\boldsymbol{x}$ must be positive, electric machine mechanical power P_{em} and electrical power are split into the two positive variables, respectively:

$$\begin{aligned} P_{em}(k) &= P_{em}^{+}(k) - P_{em}^{-}(k) \\ P_{inv,AC}(k) &= P_{inv,AC}^{+}(k) - P_{inv,AC}^{-}(k) \quad . \end{aligned} \tag{4.14}$$

Separating P_{em} in the two components $P_{em}^{+}(k)$ and $P_{em}^{-}(k)$, using Eq. (1.2) gives

$$P_{req} = P_{em}^{+} - P_{em}^{-} + P_{ice} \quad . \tag{4.15}$$

A separation of P_{ice} into two variables is not necessary, as for negative values the clutch is disengaged to separate the engine from the rest of the powertrain. In motoring mode ($P_{em}(k) > 0$) using Eq. (2.29) gives

$$P_{em}^{+}(k) = a_{em,mot} \, P_{inv,AC}^{+}(k) \quad . \tag{4.16}$$

In generating mode using Eq. (2.30) gives

$$P_{inv,AC}^{-}(k) = a_{em,gen} \, P_{em}^{-}(k) \quad . \tag{4.17}$$

The influence of the motor power on battery charge is described by

$$P_{bat}(k) = \frac{E_{bat}(k-1) - E_{bat}(k)}{\Delta t} \quad . \tag{4.18}$$

To prevent engine use in regenerative braking mode ($P_{req} < 0$, Eq. (2.26)), the inequality constraint

$$s_{ice}(k) \; P_{req}(k) \geq 0 \tag{4.19}$$

is used. P_{req} is calculated as a function of cycle power $\bar{P}_{cycle}$ from Eq. (3.33) and η_{trans} using Eq. (2.26).

The MILP objective function to minimize is

$$\begin{bmatrix} P_{em}^{opt}(k) \\ P_{ice}^{opt}(k) \\ s_{ice}^{opt}(k) \\ E_{bat}^{opt}(k) \end{bmatrix} = \arg \min_{P_{em}(k), s_{ice}(k)} [f_{LM}(P_{em}(k), s_{ice}(k)] \quad . \tag{4.20}$$

where f_{LM} stands for the linear vehicle model described above and in Section 2.4. The component constraints are

$$\begin{aligned} 0 \leq P_{em}^{+}(k) &\leq P_{em,max} \\ 0 \leq P_{em}^{-}(k) &\leq -P_{em,min} \\ 0 \leq P_{ice}(k) &\leq P_{ice,max}\, s_{ice}(k) \\ E_{bat,min} \leq E_{bat}(k) &\leq E_{bat,max} \quad . \end{aligned} \tag{4.21}$$

The initial and final boundary conditions for the battery energy are defined by

$$\begin{aligned} E_{bat}(k_0) &= SOC_0\, E_{bat,max} \\ E_{bat}(N) &\geq SOC_N\, E_{bat,max} \end{aligned} \tag{4.22}$$

where k_0 is the initial time step and N the last time step of the driving cycle.

4.3 Definition of the SOC Set Point Function

From the MILP described above the optimal power distribution between engine and electric motor in terms of fuel consumption is obtained, and, consequently, the battery energy level corresponding to the state of charge due to $E_{bat} = E_{bat,nom}\, SOC$ to the state of charge. In the following discussion, the state of charge across a trip obtained by the MILP is $SOC_{MILP}^{*}(k)$.

The A-DP algorithm from Section 3.2 is in Section 4.4 employed in an MPC framework using a receding prediction horizon (Fig. 1.21) to control gear g, T_{ice} and T_{em}. In Section 4.4 the combination of a receding prediction horizon and the A-DP algorithm from Section 3.2 is analysed employing SOC_{MILP}^{*}.

The DP algorithm requires the boundary condition $SOC^{*}(N)$ to define the terminal cost in Eq. (3.10), i.e. the target SOC. Using a receding prediction horizon, $SOC^{*}(N)$ is not the target SOC at the end of trip, and has therefore to be defined by a function $SOC^{*}(k)$. For best results, $SOC^{*}(k)$ should coincide with the global optimal SOC. An inaccurate set point function can result in sub-optimal fuel efficency. However, $SOC^{*}(k)$ has to be calculated before starting the trip, considering the whole trip length. Therefore, the calculation is a trade-off between accuracy and calculation time.

Accuracy of $SOC^*(k)$ is crucial, especially when using short predictions horizons. Using long prediction horizons of 600s or more, even sub-optimal $SOC^*(t)$ show good results, as demonstrated in [61] with a linear function of the trip distance. In the following, to facilitate the use of short prediction horizons and thus decrease computational load of the gear and torque control, the MILP is instead employed for calculation of the function $SOC_{MILP}^*(k)$. $SOC_{MILP}^*(k)$ is calculated for the driving cycles BCN-CTS, CTS-BCN, FTP-72 and the CADC. The accuracy of $SOC_{MILP}^*(k)$ is evaluated by comparing them to the global optimal SOC. Deviation from the global optimum (calculated by S-DP) is analysed to formulate proposals to improve results.

Instead of an optimization based function $SOC^*(k)$ also a linear (in terms of trip distance) function $SOC_{lin}^*(k)$ can be used [61]. Comparing the function $SOC_{lin}^*(k)$ with SOC_{MILP}^* and the global optimum for the BCN-CTS cycle, SOC_{MILP}^* is significantly closer to the global optimum (Fig. 4.4). This results from consideration of the power requirement of the cycle, i.e. includes information about the power load during the cycle and vehicle component efficiencies. SOC_{MILP}^* also coincides well with the global optimum for the cycles FTP-72 and CADC (Fig. 4.4, Fig. 4.5, Fig. 4.7), only during the CTS-BCN cycle a greater deviation between second 600 and second 1250 can be observed (Fig. 4.6).

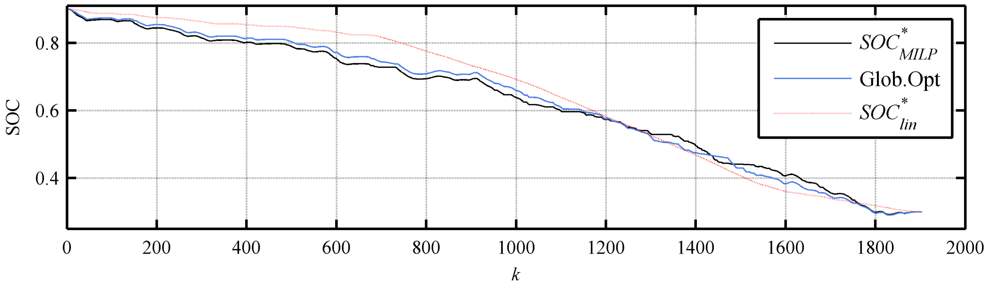

Fig. 4.4. The SOC set point functions $SOC_{lin}^*(k)$ and $SOC_{MILP}^*(k)$ for the BCN-CTS cycle compared to the global optimal SOC.

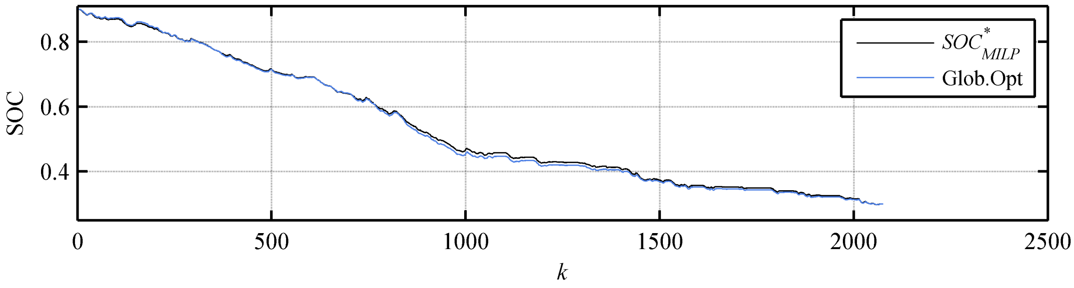

Fig. 4.5. SOC set point function for the CADC compared to the global optimum.

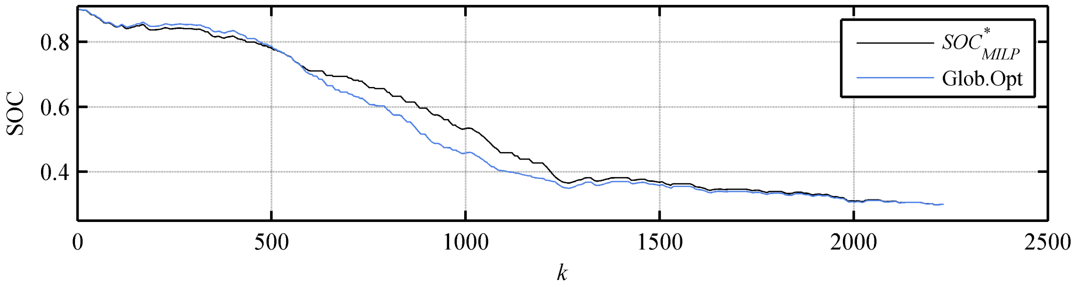

Fig. 4.6. SOC set point function for CTS-BCN cycle compared to the global optimum.

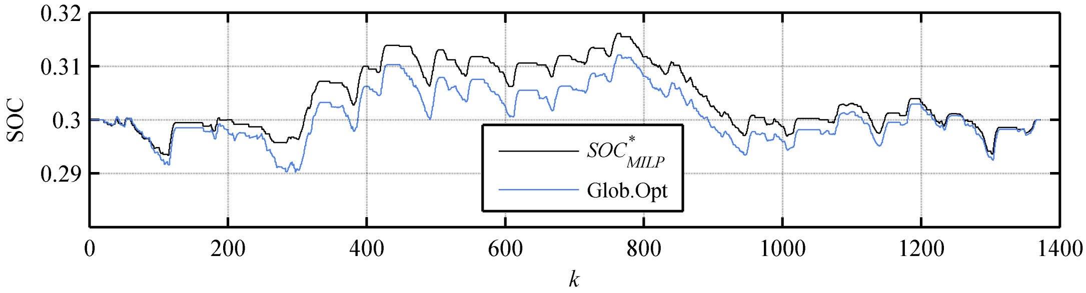

Fig. 4.7. SOC set point function for FTP-72 cycle compared to the global optimum.

In the following, the reasons for deviations of the SOC from the global optimum are analysed, and proposals are made to improve results. Deviation of SOC^*_{MILP} from global optimum results from the different power distribution between engine and electric motor across the cycle. The corresponding power distribution between P_{em} and P_{ice} for SOC^*_{MILP} is depicted in Fig. 4.15. During the cycle, engine starts distribution is similar to that of the global optimum (Fig. 4.16).

During the cycle CTS-BCN, The MILP has a shorter engine run time of 401s, instead of 437s. This can be observed between second 1200 and 1230, in which the MILP does not run the engine. Considering engine run time and mechanical energy E_{ice} generated during the trip (Table XII), for the MILP an average mechanical power of $\bar{P}_{ice,MILP} = 21{,}3\text{kW}$ results, compared to $\bar{P}_{ice,glob-opt} = 19{,}3\text{kW}$ for the global optimum. A shorter engine run time and a higher average engine power is also observed for the cycles BCN-CTS and CADC. This different power profile of the engine compared to the global optimum results in deviations of the SOC across the cycle. An important reason for the deviation of engine power is the difference between the specific fuel consumption as a function of engine power P_{ice} of the MILP engine model (Fig. 4.11), and the model used for calculating the global optimum (Fig. 4.10). While the convex engine model used for the MILP has its minimal specific consumption at $P_{ice} = 26.7\text{kW}$, the fuel table based nonlinear model has minimal fuel consumption in a lower power region at approximately $P_{ice} \approx 14\text{kW}$. The preferred use of the load point for minimal fuel consumption can be observed also for the cycles CADC (Fig. 4.13) and BCN-CTS (Fig. 4.15).

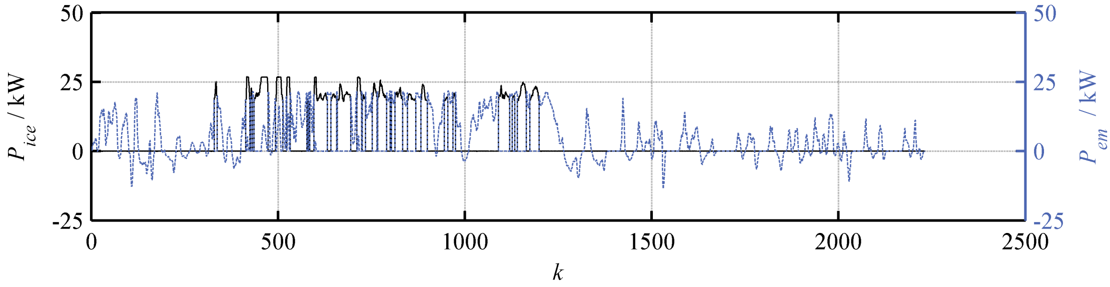

Fig. 4.8. Power distribution for the cycle CTS- BCN obtained by the MILP.

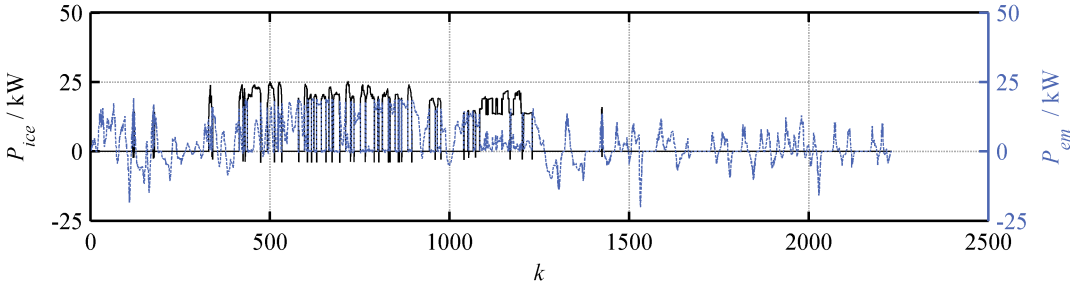

Fig. 4.9. Power distribution for the cycle CTS-BCN obtained by the DP.

In addition to differences in the engine model, the MILP is based on a simplified battery model using constant battery efficiency. The constant efficiency can lead, particularly in combination with the engine model characteristics, to increased energy buffering in the battery. For further evaluation, the indicator $E_{bat,\Sigma}$ is defined, which depicts the energy flow through the battery but neglects influence of the battery efficiency:

$$\begin{aligned} E_{bat,in} &= \sum_{k} \left| P_{inv,DC}(k)\,\Delta t \right| \qquad P_{bat}(k) < 0 \\ E_{bat,out} &= \sum_{k} P_{bat}(k)\,\Delta t \qquad P_{bat}(k) > 0 \\ E_{bat,\Sigma} &= E_{bat,in} + E_{bat,out} \ . \end{aligned} \tag{4.23}$$

Generally, using the battery in charge mode should be limited to driving situations in which a significant increase in engine efficiency is achieved. If not, losses in the electric components can exceed the engine efficiency gain. Comparing the battery energy flow $E_{bat,\Sigma}$ of the MILP and the global optimum, the battery is used more intensively by the MILP with an increase of $E_{bat,\Sigma}$ between 4.0 and 5.3% (Table XII). Advantageous is a battery use at a relatively low battery power. Assuming a constant battery output voltage, the output power is proportional to the output current. As the ohmic losses of the battery increase quadratically with the current, battery efficiency decreases at higher output power. This effect is intensified by output voltage drop resulting from increased power delivery. This decrease in battery efficiency at high power is significantly higher than increases in electric motor or inverter efficiency. However, the MILP uses a battery model with constant battery efficiency; therefore high battery power is not penalized. This, and that the engine model has minimal specific fuel consumption at higher load points, explains the increased battery use. The constant battery efficiency of the MILP also leads to peaks of P_{em} during BCN-CTS between second 1000 and 1500. However, during the FTP-72 cycle, battery power flow is about 10.7% lower. Due to the low power profile of the trip, the battery model used for calculation of the global optimum driving electrically yields a battery efficiency of 0.97 (Table XIII). Therefore, to improve achieved results further, battery efficiency should be considered as power dependent.

The increased battery loss during the FTP-72 is compensated for by a higher mechanical energy E_{ice} produced by the engine. The strong increase in E_{ice} during the CADC is caused instead by a long period of engine operation at its point of minimal specific consumption, which is higher than the power requirement. Therefore, more electric energy is buffered and more losses in the electric system occur. This demonstrates the importance of fuel consumption model accuracy, particularly as the accuracy is considered by the objective function of the MILP and thus influences MILP results strongly. While fuel consumption coincides well with the global optimum for the BCN-CTS and CTS-BCN with deviations of 0.4% and 2.0%, deviation for FTP-72 and CADC is higher (Table XIV).

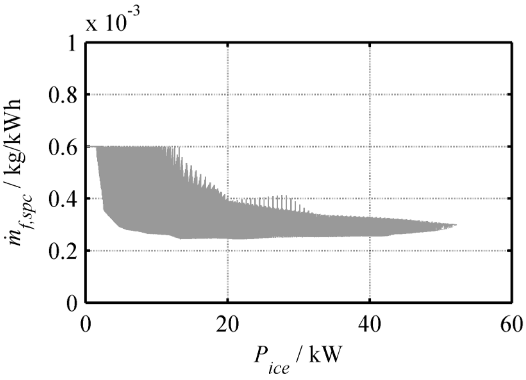

Fig. 4.10. Specific consumption of the engine model used for calculation of the global optimum.

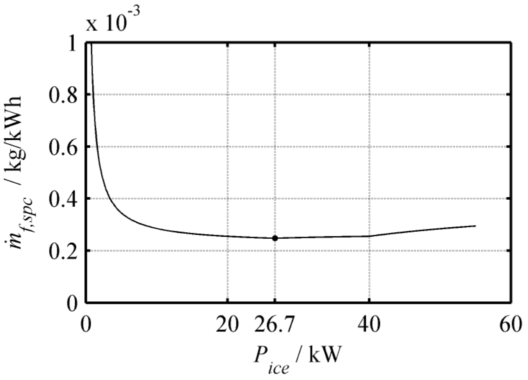

Fig. 4.11. Specific consumption of the convex engine model.

For the FTP cycle, fuel consumption is 7.3% higher with increased engine energy of 4.7% (Table XII). This results partly from the modelled fuel power curve in combination with the cycle's low power profile, as fuel consumption of the MILP model is higher when $P_{ice} < 9\text{kW}$, in comparison with the model used for calculation of the global optimum (Fig. 4.12). This model deviation is reinforced by CS operation during the FTP-72 cycle, as there is no stored battery energy which can be distributed across the trip to avoid engine operation in low efficiency regions. For the CADC the relationship is the reverse, the fuel consumption is 4.3% higher in contrast to 7.7% more produced energy. This means that the MILP operates the engine for longer at the operating point with minimal specific fuel consumption (Fig. 4.13).

Summarising, even though the SOC obtained across the cycle is already close the global optimum, from analysis of the results, three proposals are made to further improve results.

- Due to constant electric component efficiencies, results obtained by MILP depend heavily on the minimal fuel consumption operating point of the engine. Therefore, the convex description used should be modified to move the highest efficiency to a lower power region.
- Fuel consumption at low engine power does not correspond precisely with measured engine consumption. This can be prevented by adding a fourth straight line to the convex model to better approximate the low power region. As the use of such additional constraints to the MILP can increase calculation time, its impact should be evaluated.
- Improving constant battery model efficiency is a priority. Using a convex approach such as used for the engine model, this power dependence can be in-

cluded in the MILP. This results in an additional inequality constraint for the MILP, and as such its impact on calculation time has to be evaluated. Successful implementation of this proposal may eliminate the necessity of the first proposal.

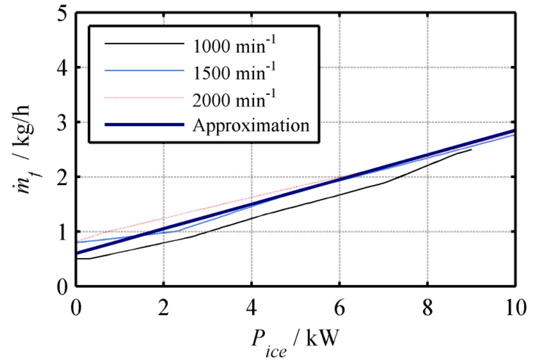

Fig. 4.12. Engine model approximation at low engine power.

Table XII: Mechanical engine energy and electrical energy flow to and from the battery obtained by the MILP compared to the global optimum and relative difference d.

Cycle	$E_{ice,MILP}$ / MJ	$E_{ice,glob-opt}$ / MJ	d / %	$E_{bat,\Sigma,MILP}$ / MJ	$E_{bat,\Sigma,glob-opt}$ / MJ	d / %
FTP-72	4.597	4.389	4.7	3.249	3.637	-10.7
BCN-CTS	11.966	11.813	1.3	10.411	10.007	4.0
CTS-BCN	8.561	8.445	1.4	12.079	11.588	4.2
CACD	2.822	2.620	7.7	15.319	14.548	5.3

Table XIII: Average component efficiencies of electric motor ($\bar{\eta}_{em}$) and battery ($\bar{\eta}_{bat}$) of the global optimum.

	FTP-72	BCN-CTS	CTS-BCN	CACD
$\bar{\eta}_{em}$	0.950	0.947	0.949	0.956
$\bar{\eta}_{bat}$	0.974	0.955	0.948	0.939

Table XIV: Fuel consumption obtained by the MILP compared to the global optimum.

Cycle	$V_{f,MILP}$ /l/100km	$V_{f,glob-opt}$ /l/100km	d / %
FTP-72	3.89	3.62	7.3
BCN-CTS	3.36	3.35	0.4
CTS-BCN	2.41	2.36	2.0
CACD	1.17	1.12	4.3

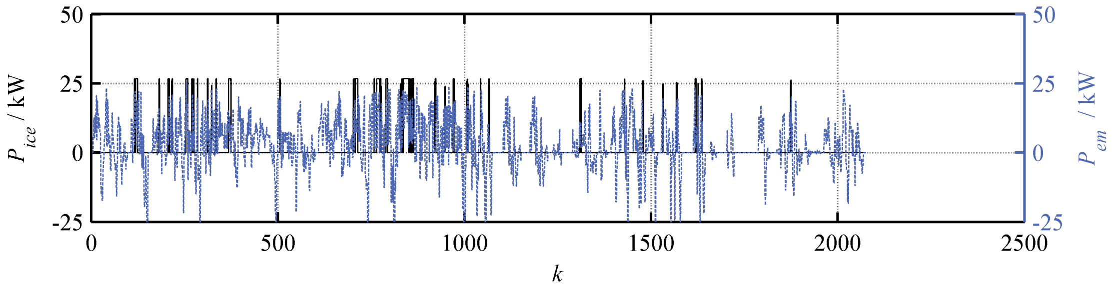

Fig. 4.13. Power distribution obtained by the MILP for the CADC.

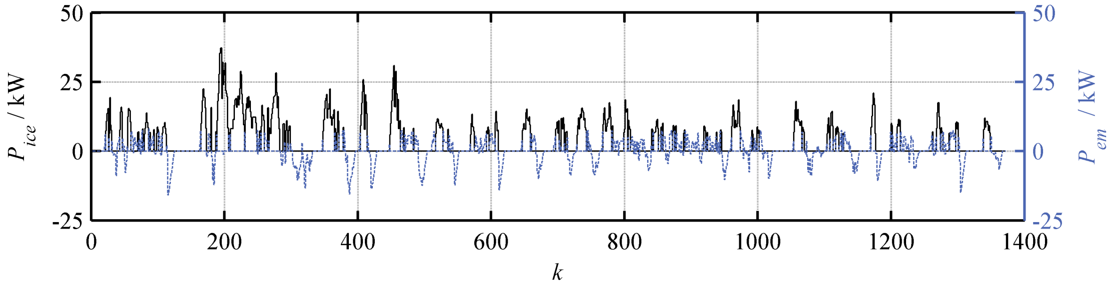

Fig. 4.14. Power distribution obtained by the MILP for the FTP-72 cycle.

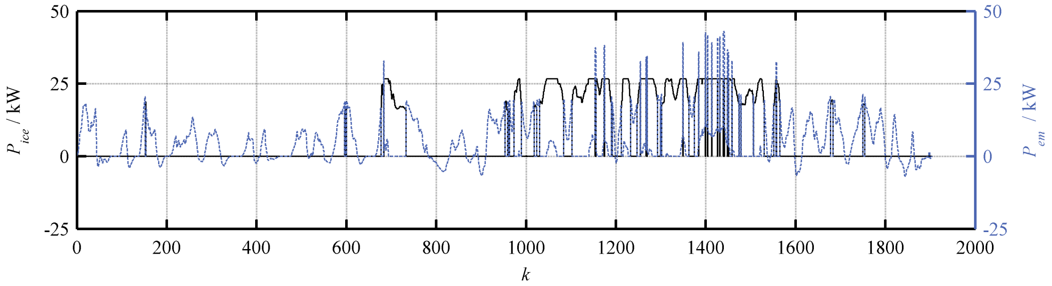

Fig. 4.15. Optimal power distribution during the BCN-CTS cycle obtained by the MILP.

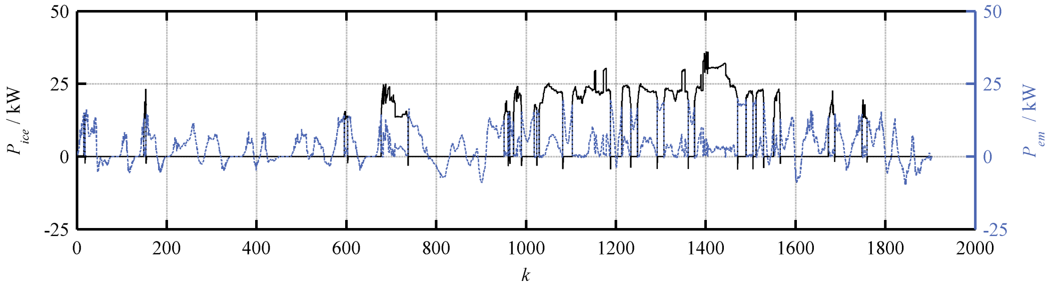

Fig. 4.16. Global optimal power distribution during the BCN-CTS cycle.

Calculation times are between 2.4s for the FTP-72 cycle and 21.7s for the CTS-BCN cycle (Table XV). MILP can theoretically lead to long calculation times and high memory use due to its integer values and the resulting split into sub-problems to be solved. However, typical optimization problems can be solved quickly by employing the branch-and-cut algorithm. Using the time step $\Delta t = 1\text{s}$, for the CTS-BCN cycle result 2231 integer states to optimize, which results in increased calculation time. In order to further accelerate the algorithm, an important number of the integer states can be initialised for trip sections with $v = 0$ and for high power trip sections.

Table XV: Calculations times of the MILP (Intel i3 (1.8GHz) running Windows x64).

	FTP-72	BCN-CTS	CTS-BCN	CACD
t / s	2.4	9.5	21.7	8.1

4.4 Implementation of an MPC Framework

The functions $SOC^*_{MILP}(k)$ obtained in Section 4.3 are used in this section to implement a receding prediction horizon in an MPC framework [87]. Using an MPC framework, a predictive optimization is started every N_c using the A-DP algorithm from Section 3.2. While applying the control sequence $(\boldsymbol{u}_i)$ for a control horizon, the control sequence for the next control horizon is simultaneously being calculated (Fig. 4.17). Therefore, the control horizon length N_c has to be chosen such that during this time span the predictive optimization for the employed prediction horizon length (and in a later step the adaptation of a rule-based strategy in Chapter 5) is finalized. Taking n as the count number of the repeatedly executed MPC, the control obtained by an optimization starting at nN_c can only be applied from $(n+1)N_c$. Therefore, an optimization which starts execution at nN_c uses the prediction window

$$[(n+1)N_c\,;(n+1)N_c + N_p] \tag{4.24}$$

where N_p is the prediction horizon length considered by the optimization. Due to this delay, using a shorter control horizon N_c has two advantages. Firstly, it has more precise knowledge of the optimization constraint $SOC^*((n+1)N_c\ )$, which is a necessary boundary condition for the predictive optimization. Secondly, assuming application in a real world driving situation, the trip prediction data can be refreshed more frequently and thus is more precise. While a shorter N_c is advantageous, it must be chosen long enough that optimization for the next control horizon can be terminated. The proposed algorithm is validated with $N_c = 120$ and $N_c = 60$. For simplicity, it is assumed that the predictive optimization starting at nN_c has precise knowledge of the initial boundary condition $SOC((n+1)N_c)$. This assumption corresponds to assuming that calculation time $t_{calc} = 0\text{s}$. In Section 5.5 it is demonstrated that results obtained using this assumption are valid.

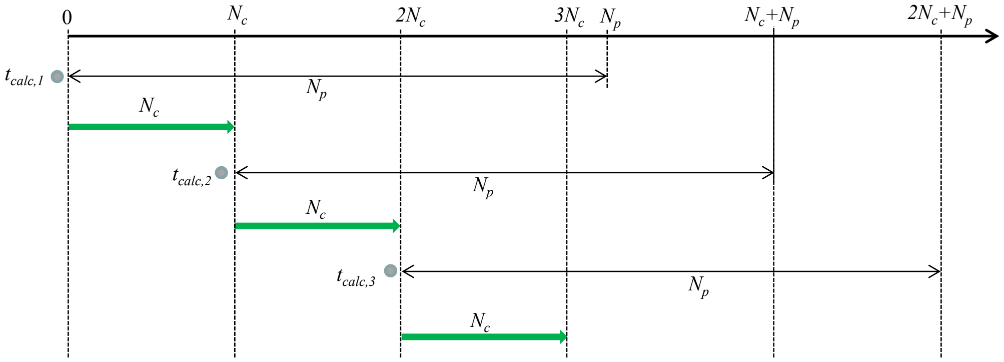

Fig. 4.17. Idealized calculation of the predictive optimization using an MPC framework. $t_{calc,i}$ *is the calculation time required for the optimization of* $[(i-1)N_c; (i-1)N_c + N_p]$.

4.5 Simulations with Receding Prediction Horizon

Simulations are carried out for the FTP-72 cycle employing CS mode, and for the BCN-CTS cycle employing CD mode. Results ($\boldsymbol{u}_i^{opt}$) obtained from the MPC framework based optimization are introduced in the vehicle forward model for comparison with the global optimum results (calculated by S-DP algorithm from Section 3.1). As electrical energy consumption can vary due to the receding horizon, for comparison the CO_2 mass m_{CO_2} emissions per km is also calculated using Eq. (3.46). Simulations are executed with different prediction horizon lengths of 200s, 300s, 450s and 600s. The control horizon is chosen $N_c = 120\text{s}$ and is for $N_p = 60\text{s}$ reduced to $N_c = 60\text{s}$ (to fulfil $N_c \le N_p$). The respective relative difference between EMS results and the global optimum are indicated in Table XVI and Table XVII. Relative difference for each prediction horizon length N_p is given by

$$d_{N_p} = \frac{x_{N_p} - x_{glob-opt}}{x_{glob-opt}} \quad . \tag{4.25}$$

The prediction horizon length influences fuel efficiency and computational cost. Due to the employed DP based optimization, computational cost increases exponentially with the prediction horizon length (Fig. 4.18, Fig. 4.19). Computational cost is also influenced by idle times ($v = 0\,\text{km/h}$) and trip sections with $P_{wh} < 0$. During these sections, the engine does not operate as the power source, reducing the decision tree of the shortest path search to one edge describing the regenerated braking energy (Fig. 3.2), and thus the algorithm has to evaluate fewer possible SOC changes from one time step to the next. This is why the calculation time for the BCN-CTS corresponds to the worst case scenario for computation time, as in its middle section there are rarely phases with regenerative braking, i.e. $P_{cycle} < 0$. Therefore, maximal calculation time is almost double the average.

Calculation times indicated are obtained by executing the MPC framework on an Intel i3 1.8GHz processor running Windows x64. Maximal calculation time for predictive optimization during the computationally more intensive BCN-CTS cycle for a prediction horizon length of 600s (i.e. $N_p = 600$), is $t_{calc,max} = 66.1$s, compared to 808s using an infinite prediction horizon (Table XIX). For $N_p = 60$, maximal calculation time goes considerably down to $t_{calc,max} = 1.5$s, which is a further reduction of over 98%. Maximal calculation time for the FTP-72 cycle $t_{calc,max}$ is 1.0s for $N_p = 60$, and 22.7s for $N_p = 600$ (Table XVIII). However, calculation time $t_{calc,max}$ obtained for the BCN-CTS cycle has more significance than the values for the FTP-72 cycle, as the case of $N_p = 60$ and $N_p = 60$ corresponds to the worst case scenario described above. The observed exponential increase of computation time with increasing prediction horizon length is characteristic of the DP algorithm.

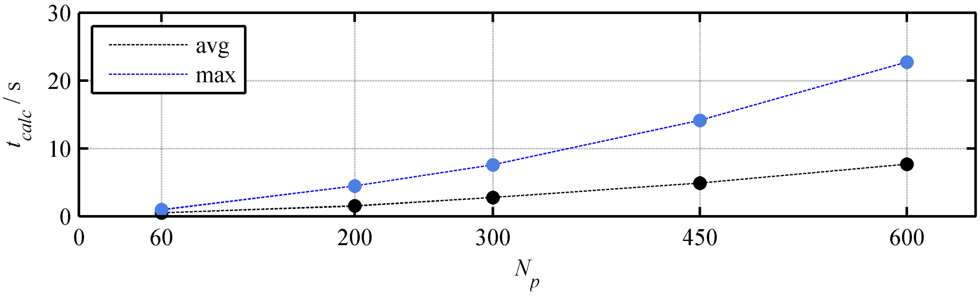

Fig. 4.18. Calculation time of the DP during the FTP-72 cycle as a function of the prediction horizon length.

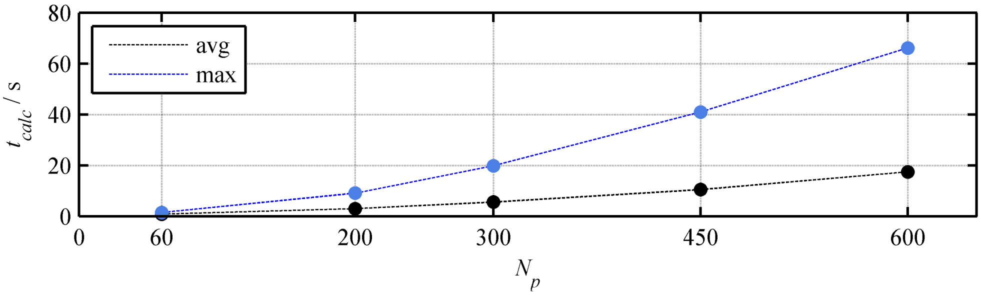

Fig. 4.19. Calculation time of the DP during the BCN-CTS cycle as a function of the prediction horizon length.

Prediction horizon length has only a slight impact on fuel consumption. For the FTP-72 cycle, deviation of CO_2 emissions per km increase from 0.3% with a prediction horizon length of 600s to 0.7% with a horizon length of 60s. For the BCN-CTS cycle, deviation of m_{CO_2} from the global optimum increases from 0.2% ($N_p = 600$) to 0.3% ($N_p = 200$) to 0.5% ($N_c = 60, N_p = 60$). This increase stems from a rise in fuel consumption of 0.30%, compared to 0.04%. As a longer prediction horizon is more tolerant of inaccuracies in SOC^*_{MILP}, results from a prediction horizon length of 450s and 600s come closer to the global optimum; however, results of all prediction horizon lengths are close to the global optimum for both cycles.

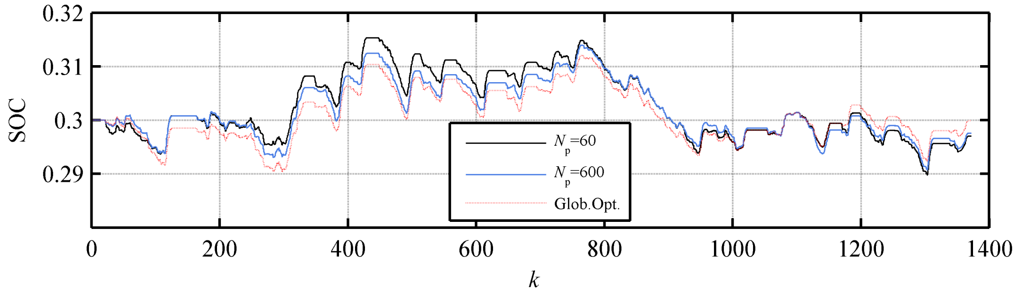

Fig. 4.20. SOC during FTP-72 cycle employing CS mode for different prediction horizon lengths and the global optimum.

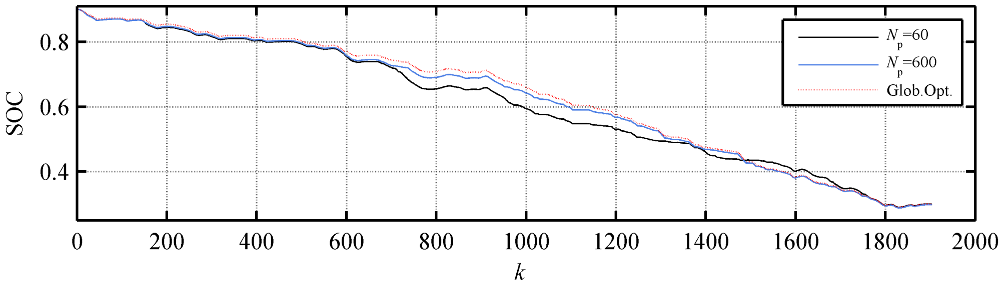

Fig. 4.21. SOC during BCN-CTS cycle employing CD mode for different prediction horizon lengths and the global optimum.

Table XVI: Relative deviation from the global optimum for different prediction horizon lengths (FTP-72 cycle).

	d_{300} / %	d_{300} / %	d_{300} / %	d_{450} / %	d_{600} / %
V_f / l/100km	0.1	0.0	0.0	-0.1	-0.1
m_{CO_2} /g/km	0.7	0.3	0.3	0.3	0.3

Table XVII: Relative deviation from the global optimum for different prediction horizon lengths (BCN-CTS cycle).

	d_{60} / %	d_{200} / %	d_{300} / %	d_{450} / %	d_{600} / %
V_f / l/100km	0.7	0.3	0.2	0.1	0.0
ΔE_{bat} / kWh/100km	0.1	0.4	0.4	0.4	0.4
m_{CO_2}/ g/km	0.5	0.3	0.2	0.2	0.1

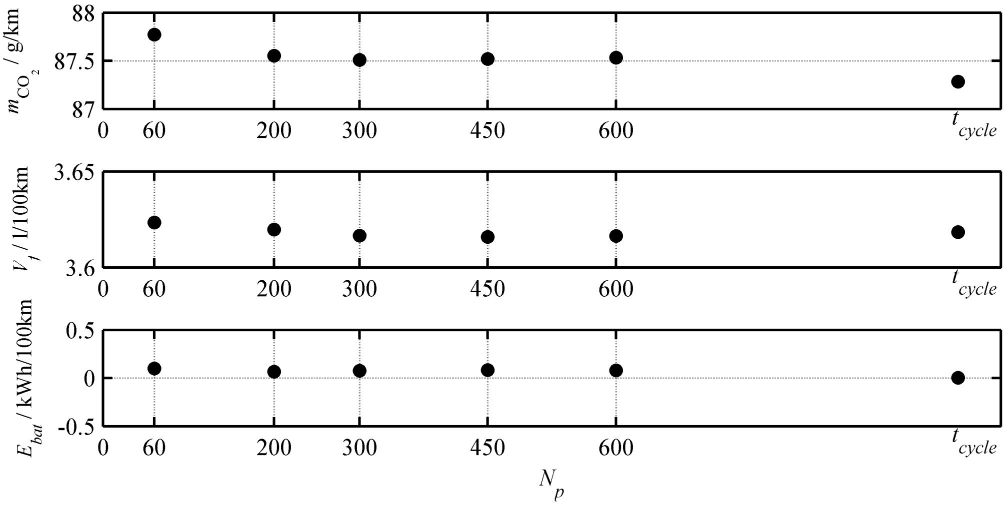

Fig. 4.22. Results for FTP-72 cycle as a function of the prediction horizon length. The values on the right end are the global optimal results using an infinite prediction horizon.

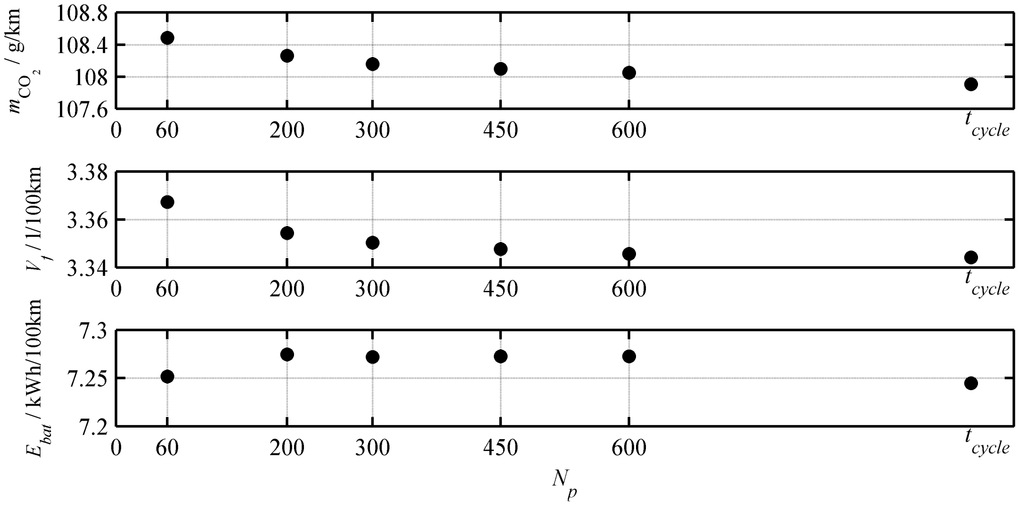

Fig. 4.23. Results for the BCN-CTS cycle as function of the prediction horizon length.

Table XVIII: Simulation results for FTP-72 cycle for different prediction horizon lengths.

	$N_p = 60$	$N_p = 200$	$N_p = 300$	$N_p = 600$	Glob. opt.
V_f / l/100km	3.62	3.62	3.62	3.62	3.62
ΔE_{bat} / kWh/100km	0.100	0.067	0.076	0.081	0.005
m_{CO_2} /g/km	87.8	87.6	87.5	87.5	87.3
$t_{calc,max}$ / s	1.0	4.5	7.6	22.7	387

Table XIX: Simulation results for BCN-CTS cycle for different prediction horizon lengths.

	$N_p = 60$	$N_p = 200$	$N_p = 300$	$N_p = 600$	Glob. opt.
V_f / l/100km	3.37	3.35	3.35	3.35	3.34
ΔE_{bat} / kWh/100km	7.252	7.275	7.272	7.272	7.245
m_{CO_2}/ g/km	108.5	108.3	108.2	108.1	107.9
$t_{calc,max}$ / s	1.5	9.1	19.8	66.1	808

4.6 Conclusions

In this chapter a method to calculate the optimal SOC in terms of fuel efficiency for a future trip is presented. The SOC is calculated with a rapid MILP assuming trip foreknowledge. By calculating the SOC set point function before trip start, it can be used in an MPC framework for implementation of a receding prediction horizon. Through utilisation of the SOC set point function CD operation of the PHEV is supported. While the obtained SOC set point function coincides well with results obtained using DP in Chapter 3 for the FTP-72, BCN-CTS and CADC cycles, the function obtained for the CTS-BCN cycle differs in the middle section. Deviation is caused by the linear vehicle model description used for the MILP algorithm and proposals for improvement are made.

Using the SOC set point function within the MPC framework, and carrying out the torque and gear optimization using the accelerated DP algorithm described in Section 3.2, results obtained indicate that the prediction horizon length can be reduced considerably with little reduction in fuel economy. Simulations are carried out with prediction horizon lengths of 60s, 200s, 300s, 450s and 600s. Using a prediction horizon length of 60s, computation time is reduced by 98% when compared to a prediction horizon length of 600s and by approximately 99.8% when compared to an entire trip length prediction horizon. Computation time reduction depends heavily on the employed optimization algorithm within the MPC framework. The impact of the prediction horizon is particularly high, given that calculation time for the employed DP algorithm increases exponentially with prediction horizon length.

Fuel economy is closest to the global optimum in terms of fuel efficiency, calculated by DP, using the longest simulated prediction horizon length of 600s, and reduces only slightly for shorter horizons. Even the shortest simulated length of 60s still yields fuel economy close to the global optimum. Deviation from the global optimum for fuel consumption and CO_2 emissions is below 0.7%, with deviation of electrical energy consumption below 0.5% for the cycles FTP-72 and BCN-CTS.

In the middle trip section of the CTS-BCN cycle, the SOC set point function deviates from the global optimum, which results in the EMS having to employ the less efficient charge mode, and consequently fuel consumption and CO_2 emissions increase. The consequences of this are discussed in the next chapter and show the importance of the accuracy of the SOC set point function. Where trip prediction data relating to speed and road grade are accurate, results obtained are valid.

Finally, using MILP for calculation of a SOC set point function allows not only the use of the A-DP approach, but also the reduction of the prediction horizon length for any other optimization algorithm having the initial and final SOC of the prediction horizon as boundary conditions.

5 Adaptive Rule-based EMS

In the previous chapter a predictive EMS has been presented, which combines an A-DP algorithm with a model predictive framework for the implementation of a receding prediction horizon. In order to achieve charge depletion, a SOC set point function $SOC^*(t)$ is calculated before starting the trip (Section 4.3). The calculation of $SOC^*(t)$ as well as optimization with a limited prediction horizon depend on trip foreknowledge by the EMS which is obtained from route indication by the driver in combination with road and traffic data evaluated by predictive trip algorithms (Section 1.5). However, even as available technologies improve significantly and new technologies such as ITS and V2V will help further enhance prediction, a level of inaccuracy of prediction data will remain. In addition to accuracy of prediction data, aspects other than fuel consumption have to be considered by an EMS. This includes gear shift frequency, acceleration behaviour and for drivetrain structures which permit the decoupling of the engine from the powertrain by means of a clutch, the number of engine starts. The reduction in engine starts can be achieved by adapting the cost function of the optimization algorithm, such as used by an instantaneous cost function EMS based in [57] which considers the energy required to accelerate the engine from standstill to idle speed. A similar cost could also be considered by the cost function of the optimization presented in Section 3.1. As the objective is a strategy which, in addition to reduction engine starts, is robust to erroneous prediction data, a rule-based strategy is instead chosen.

Rule-based strategies are generally designed manually, i.e. without the use of optimization algorithms but with consideration given to the system component efficiency such as in [88]. Due to their manual design, these approaches such as fuzzy controllers are known as *intuitive strategies*. The rules of such an EMS can refer to the actual torque demand, the SOC and the velocity (Fig. 5.1). Often the rules are defined to imitate the behaviour of optimization based strategies or its parameters are optimized by using offline solutions such as *genetic algorithms* [89].

An advantage of intuitive strategies is their explicitly defined rules, which provide an easier understand of powertrain behaviour in specific driving situations, thus simplifying the process of solving any problems that may arise. Furthermore, frequency of engine starts and gear shifting is more reliably controlled. However, vehicle fuel consumption generally increases as a result of sub-optimal (in terms of fuel efficiency) engine start and gear shifting behaviour regarding fuel consumption, i.e. the operation of engine and motor in lower efficiency regions. Another disadvantage of current rule-based strategies is the additional challenges they present in achieving optimal battery

SOC for the trip. With fixed, predefined rules, future SOC development depends heavily on the cycle type. Rules adapted by a non-predictive optimization do not reliably achieve the target SOC and thus yield sub-optimal fuel efficiency results.

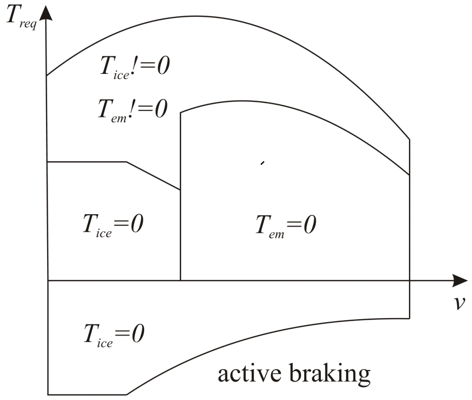

Fig. 5.1. Typical rule-based EMS for parallel HEV in terms of motor torque and vehicle speed according to [73].

Although rule-based CD approaches are possible by adapting the rules regarding the upcoming cycle section type (e.g. urban or extra urban) [90], for achieving a defined target SOC such rule adaptation can only be carried out with the support of optimization algorithms. In [91] a CD rule-based strategy for PHEV is presented with a fixed discharge rate, i.e. trip prediction data is not used. In this approach the final SOC depends therefore on the trip profile. In [92] another CD rule-based strategy is presented, using as *a priori* information only the trip length. Therefore, the strategy cannot consider the power requirements of terrain elevation and motorway sections and other high power demands sections during the cycle.

In the following Sections 5.1-5.4 the EMS approach for a rule-based strategy with high fuel efficiency in CD and CS mode is presented. The results which can theoretically be achieved with rule adaptation based on a global optimization are presented in Section 5.5. In Section 5.7, the rule-based approach is combined with the real time implementable EMS of Section 4.4 to analyse the influence on fuel economy. Finally, the robustness of the results is tested for inaccurate prediction data in Section 5.8.

5.1 Rule-based EMS Structure

The proposed rule-based EMS first selects the operation mode depending on power request P_{req} by the driver and vehicle speed v. The available modes are regenerative braking mode, electric mode, charge mode and boost mode (Section 1.2.2). In the following, the ICE mode ($T_{ice} \neq 0\text{Nm}, T_{em} = 0\text{Nm}$) is considered a special case of the boost mode. In electric and regenerative braking mode, the engine is switched off and decoupled from the powertrain by opening the clutch. In charge and boost mode (referred to as hybrid modes in the following due to use of both engine and electric motor), the engine is started and the clutch is closed. The electric motor supports the engine by a positive torque (boost mode) or generating electrical energy by a negative torque (charge mode). The rules for the mode selection are depicted in Fig. 5.2. If the power request P_{req} exceeds the power P_{boost}, boost mode is entered. P_{boost} corresponds to the optimal consumption line $T_{ice,spc.min}$. In addition to P_{boost} there is a lower limit P_{hybrid} which separates electric mode from hybrid mode P_{hybrid} is adapted during the trip by a SVM implementation (Section 5.4) based on the optimal control sequence ($\boldsymbol{u}_i^{opt}$) obtained by the predictive optimization. Whether hybrid mode ($\boldsymbol{u}_i^{opt}$) from and the predictive optimization is used, or a rule-based choice of torque and gear, depends on the accuracy of the prediction data. When the predictive optimization for the next control horizon N_c results in operation in electric mode only, the engine is only started when the power demands exceeds P_{boost} (Fig. 5.2, right). A flow chart of these rules is depicted in Fig. 5.4. In order to avoid frequent engine starts, a hysteresis of 4kW between electric mode and hybrid mode is implemented.

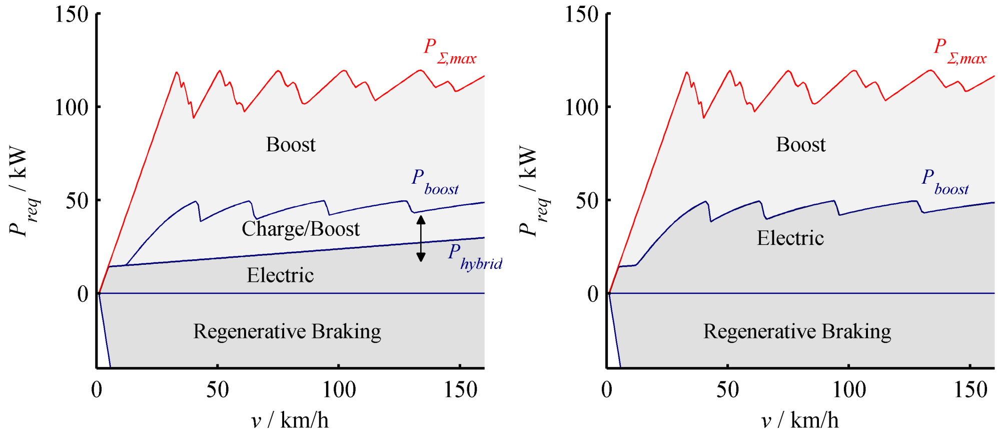

Fig. 5.2. Operation modes as a function of vehicle speed v and power request P_{req}. P_{hybrid} is adapted during the cycle. $P_{\Sigma,max}$ is the maximal power which can be delivered if engine and electric motor operate at maximal power. The dark gray marks the electric mode, whereas the lighter gray area marks the hybrid modes with engine use.

The rules are embedded in the EMS, whose logical sections are depicted in Fig. 5.3. The trip forecast using GPS/GIS information is beyond the scope of this work, the focus of which is restricted to vehicle control. At trip start, the MILP calculates the SOC set point function SOC^{*}_{MILP} based on the forecasted trip data. During the trip, the MPC is executed every nN_c. Firstly, the predicted vehicle speed $v(\cdot\,|nN_c)$ for the prediction horizon N_p

$$v(\cdot\,|nN_c) = (v(k|nN_c), v(k+1|nN_c), \dots, v(k+N_p|nN_c)) \tag{5.1}$$

at time step k just as the road inclination $\alpha_{road}(\cdot\,|nN_c)$ is used to calculate the future power request by the driver $P_{req}(\cdot\,|nN_c)$. Using $P_{req}(\cdot\,|nN_c)$ and $v(\cdot\,|nN_c)$, gear g and torques $T_{em}(\cdot\,|nN_c)$ and $T_{ice}(\cdot\,|nN_c)$ are obtained by the A-DP algorithm from Section 3.2 using SOC^*_{MILP} for the required boundary condition of the SOC at the end of the prediction horizon. From the torque $T_{ice}(\cdot\,|nN_c)$ and $T_{em}(\cdot\,|nN_c)$ the operation mode for every time step is determined (see operating points in Fig. 5.15). The optimal separator P_{hybrid} between electric mode and hybrid is then obtained using SVM.

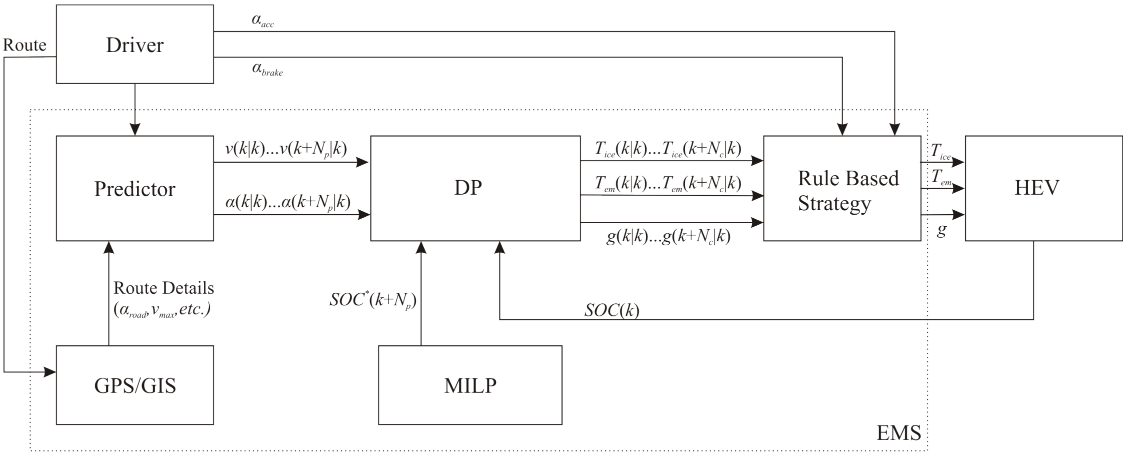

Fig. 5.3. Block diagram of the complete EMS.

5.2 Hybrid Mode Control

Due to the time-continuous implementation of the rule-based EMS, in the following for rule description a notation based on time t is used. The relationship between k and t is given by $t = k\ \cdot 1\text{s}$. Values obtained by the time-discrete optimization algorithm DP and MILP are, when necessary, linearly interpolated.

The first decision of the rule-based strategy at every execution step is the selection of either electric mode or hybrid mode, which comprise boost and charge mode. The selection is done regarding the limits P_{hybrid} and P_{boost} (Fig. 5.4). Hybrid mode is selected when P_{req} exceeds one of these limits. In hybrid mode, when the driving condition corresponds to the predicted, i.e.

$$v(t) \in [v(t|nN_c) - 5\text{km/h};\ v(t|nN_c) + 5\text{km/h}] \tag{5.2}$$

$$P_{req}(t) \in \left[P_{req}(t|nN_c) - 5\text{kW};\ P_{req}(t|nN_c) + 5\text{kW}\right]$$

values of T_{em}, T_{ice} and g obtained by the predictive optimization are used (Fig. 5.4). In the case that the actual driving situation does not correspond with the predicted one, T_{em}, T_{ice} and g are controlled by rules. In the following, the rules are described which define powertrain control in case of inaccurate prediction data. In the charge/boost mode region of Fig. 5.2, the SOC is compared to SOC_{DP}^{*} which is obtained by the predictive optimization. If

$$SOC(t) \leq SOC_{DP}^{*}(t) - 0.005 \quad , \tag{5.3}$$

charge mode is entered to approach $SOC_{DP}^{*}(t)$. In contrast, when

$$SOC(t) > SOC_{DP}^{*}(t) - 0.005 \quad , \tag{5.4}$$

boost mode is entered. This ensures that the SOC remains close to the set point function SOC_{DP}^{*} and consequently SOC_{MILP}^{*}.

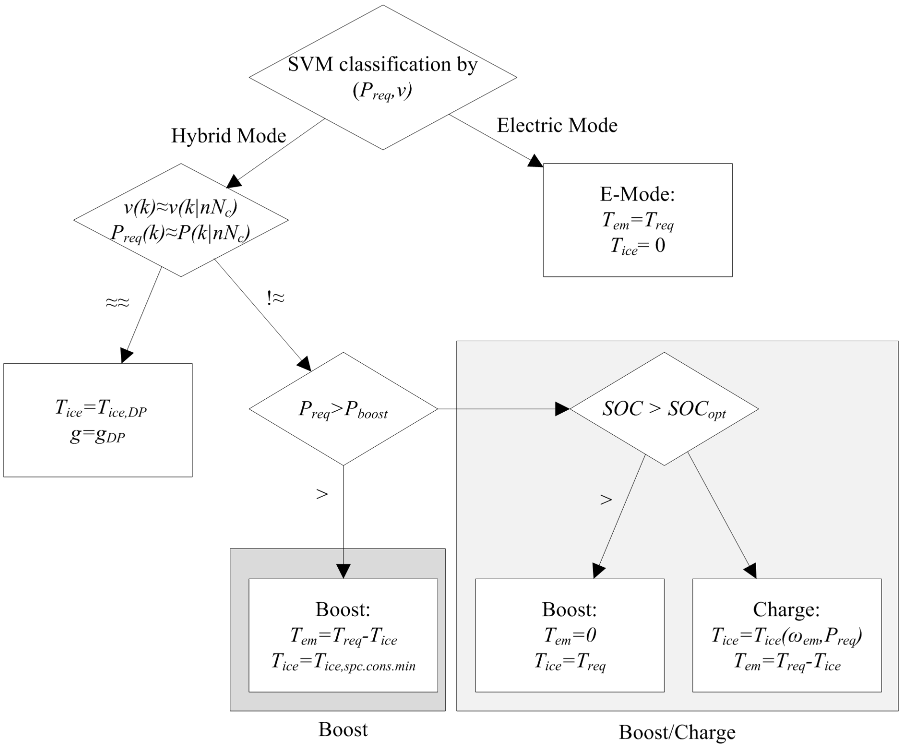

Fig. 5.4. Flowchart of the rule-based strategy.

5.2.1 Boost Mode

If boost mode is entered because of $P_{req} > P_{boost}$, the engine is supported by the electric motor:

$$\begin{aligned} T_{ice}(t) &= T_{ice,spc,min}(\omega_{ice}) \\ T_{em}(t) &= T_{req}(t) - T_{ice}(t) \quad . \end{aligned} \tag{5.5}$$

On the contrary, when entering boost mode because of Eq. (5.4), i.e. with a lower torque request than $T_{ice,spc,min}$, the engine torque is

$$T_{ice}(t) = T_{req}(t) \quad . \tag{5.6}$$

5.2.2 Charge Mode

To guarantee fuel efficient operation in charge mode, torque is minimized in terms of the fuel consumption – battery power ratio $\dot{m}_f/P_{bat}$ as a function of the motor speed ω_{em} and power request P_{req}:

$$\begin{aligned} T_{ice}(\omega_{em}, P_{req}) &= \arg\min_{P_{bat}} \left(\frac{\dot{m}_f(P_{bat}, \omega_{em}, P_{req})}{P_{bat}} \right) \\ T_{em}(\omega_{em}, P_{req}) &= \arg\min_{P_{bat}} \left(\frac{\dot{m}_f(P_{bat}, \omega_{em}, P_{req})}{P_{bat}} \right) \quad . \end{aligned} \tag{5.7}$$

The corresponding values of T_{ice} and T_{em} are calculated for the vehicle characteristics and stored in lookup tables (Fig. 5.5, Fig. 5.6).

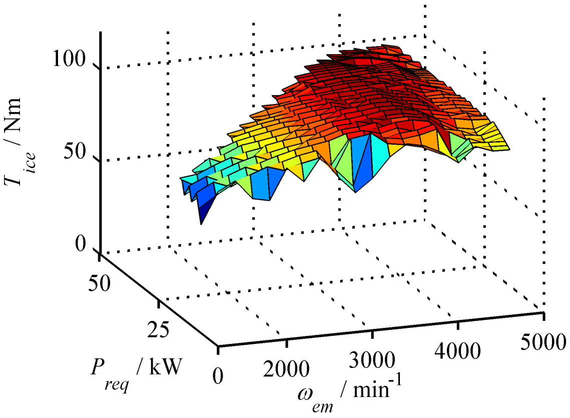

Fig. 5.5. T_{ice} with minimal ratio min($\dot{m}_f/P_{req}$) as function of ω_{em} and P_{req}.

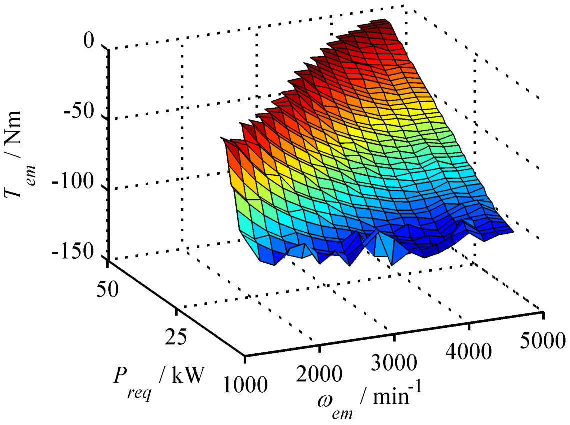

Fig. 5.6. T_{em} with minimal ratio min($\dot{m}_f/P_{req}$) as function of ω_{em} and P_{req}.

Using lookup tables, rounding errors are generated; here by the grid spacing of P_{req} and ω_{em}. The maximum error $\left|T_{req}' - T_{req}\right|$, T_{req}' being the value stored in tha lookup table, generated by the rounding error of P_{req} is, considering the grid spacing of P_{req} of 1kW is (Fig. 5.7)

$$e_{T,max}(\omega_{em}) = \max_{P'_{req},P_{req}} \left|\frac{1}{\omega_{em}}\left(P'_{req} - P_{req}\right)\right| = \frac{1}{\omega_{em}} 500\mathrm{W} \tag{5.8}$$

The maximum error resulting from the grid spacing of ω_{em} of $50\mathrm{s}^{-1}$ is given by (Fig. 5.8)

$$e_{T,max}\left(P_{req}\right) = \max_{\omega_{em},\omega'_{em}} \left|P_{req}\left(\frac{\omega_{em} - \omega_{em}'}{\omega_{em}\,\omega'_{em}}\right)\right| \approx P_{req} \cdot 2.45\;10^{-4}\mathrm{s}\ . \tag{5.9}$$

To compensate for the error, only the torque T_{ice}' is extracted from the lookup table whereas the electric motor torque is a function of the driver request $T_{em} = T_{req} - T_{ice}'$

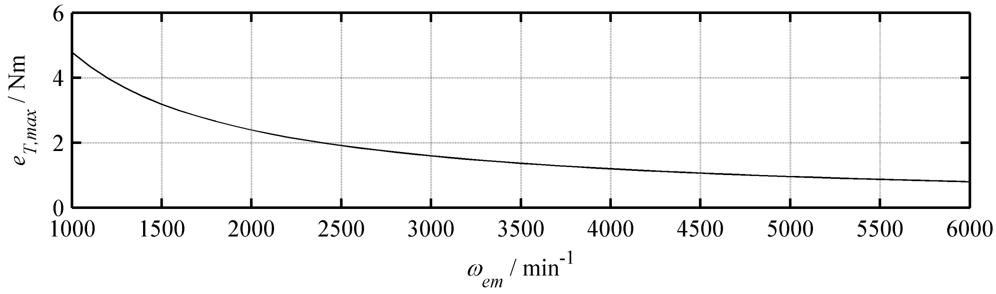

Fig. 5.7. Torque error caused by using lookup tables as a function of ω_{em}.

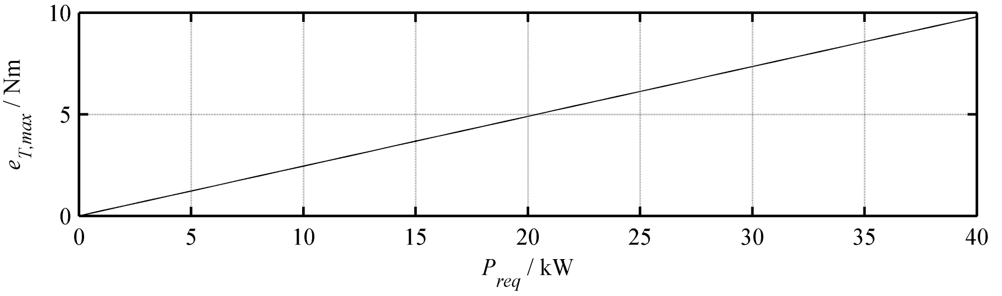

Fig. 5.8. Torque error caused by using lookup tables as a function of P_{req}.

5.3 Gear Shift Control

When operating in hybrid mode and the real driving situation corresponds to the predicted (see Eq. (5.2)), the gear from ($\boldsymbol{u}_i^{opt}$) obtained by the predictive optimization is used. In the opposite case, the EMS uses two different gear schedules, one for electric mode and one for hybrid mode. Using gear schedules in parallel HEVs is more challenging than in conventional vehicles, because in addition to engine efficiency also efficiency of the electric powertrain components has to be considered. It is recommendable to use at least two different schedules, one for driving electrically and one for engine supported driving, because the high efficiency regions of engine and electric motor are distributed quite differently. The gear schedule used here for electric mode is optimized in terms of electric motor efficiency (Fig. 5.12). From a measured efficiency table $\eta_{em}(T_{em}, \omega_{em})$ and using Eq. (2.5) the optimal gear can be calculated as a function of electric motor power and vehicle speed

$$g_{em}(P_{em}, v) = \arg\max_{g} \eta_{em}(P_{em}, v, g) \quad . \tag{5.10}$$

In hybrid mode, efficiency considerations become more difficult. As both engine and electric motor are operating, the optimal gear depends on the respective operating point of both machines. An approach is using a third gear shifting schedule for hybrid mode, as proposed in [93], [94]. Another approach is to use gear shifting schedules which depend on three input parameters, namely vehicle speed, engine and motor torque [95]. A generalized shifting schedule for hybrid mode can only be optimized for a specific power distribution between electric motor and engine. To analyse the influence of battery power on the optimal schedule, from the DP lookup tables of Section 3.2 the gear table $\boldsymbol{F}_g$ is evaluated for three power distribution cases with a battery power P_{bat} of 0kW, 10kW and -10kW. The gear is selected in terms of fuel efficiency

$$g_{hybrid} = \arg\min_{g} \dot{m}_f(P_{wh}, v, P_{bat}) \quad . \tag{5.11}$$

The value can be extracted from the lookup table $\boldsymbol{F}_g(P_{wh}, v, \Delta E_{bat})$ of Eq. (3.35) using $\Delta E_{bat} = P_{bat} \Delta t$. The case $P_{bat} = 0\text{kW}$ is close to the case regarding only the engine efficiency depicted in Fig. 5.13. A difference results from the grid shift of the lookup table due to the battery power $E_{bat,shift}$ in electric mode by (Eq. (3.19)). Therefore, the axis dimension $\tilde{P}_{ice}$ corresponds not exactly, but only within the margin $\pm 0.5\text{kW}$ to the value of P_{ice}:

$$\left|\tilde{P}_{ice} - P_{ice}\right| \leq 0.5\text{kW} \quad . \tag{5.12}$$

The limitation of the gears by a vertical line results from the engine speed limitation done by the calculation of DP to values of $\omega_{em} \in [900; 4000]$.

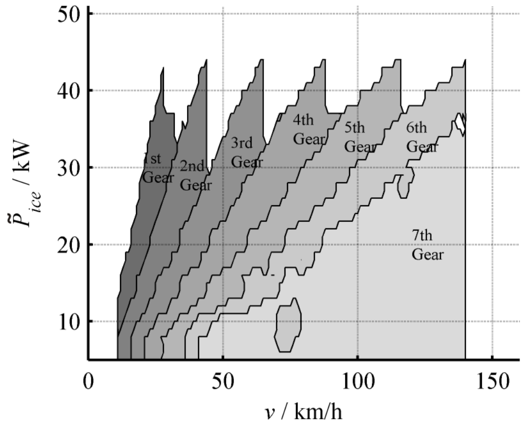

Fig. 5.9. Optimal gear g_{hybrid} in terms of fuel mass flow in ICE mode with $P_{bat} = 0kW$.

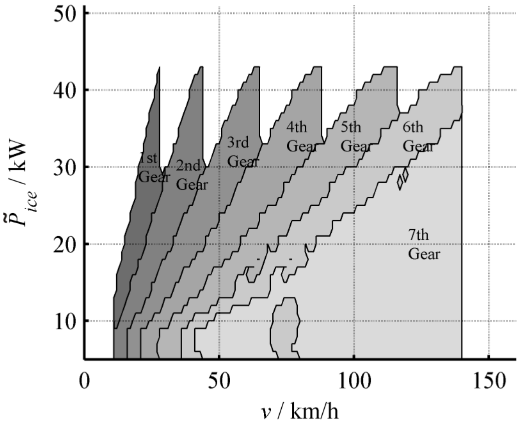

Fig. 5.10. Optimal gear g_{hybrid} in terms of fuel mass flow in boost mode ($P_{bat} = 10kW$).

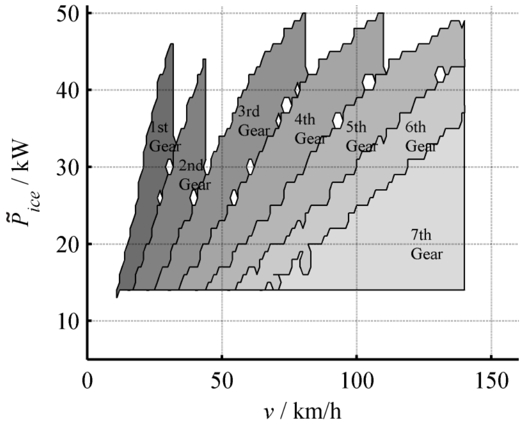

Fig. 5.11. Optimal gear g_{hybrid} in terms of fuel mass flow in charge mode ($P_{bat} = -10kW$).

The resulting gear schedules $g_{hybrid}(P_{ice}, v)$ as a function of P_{bat} (Fig. 5.9, Fig. 5.10, Fig. 5.11) show frayed limits due to its extraction from the lookup tables and interpolation to the grid $\tilde{P}_{ice}$. Nevertheless, the different cases can be compared. As the gear schedules are quite similar for different P_{bat}, charge, boost and ICE mode the same schedule is used. Using only two gear schedules results in less gear shifts, as every change of the active gear schedule can lead to additional gear shifts. Therefore, in hybrid mode the influence of the electric motor efficiency is neglected and instead only the engine efficiency is optimized. The gear decision depends on P^*_{ice} and v to operate the engine at highest efficiency (Fig. 5.13), i.e. lowest specific fuel consumption:

$$g_{ice}(P^*_{ice}, v) = \arg\min_{g} \dot{m}_{f,spc}\,(P^*_{ice}, v, g) \quad . \tag{5.13}$$

P^*_{ice} is here defined by

$$P^*_{ice} = \begin{cases} T_{req}\omega_{ice} & \text{charge mode} \\ T_{ice}\omega_{ice} & \text{boost mode} \end{cases} \quad , \tag{5.14}$$

to prevent gear shift events caused by changes of T_{ice} when changing between boost and charge mode by Eq. (5.3), as in charge mode the engine torque is extracted from table $T_{ice}(P_{req}, \omega)$ of Eq. (5.7), while in boost mode T_{ice} depends directly on the torque demand by the driver. Both gear shifting schedules include a hysteresis of $\Delta P_{req} = 4\text{kW}$ (not depicted).

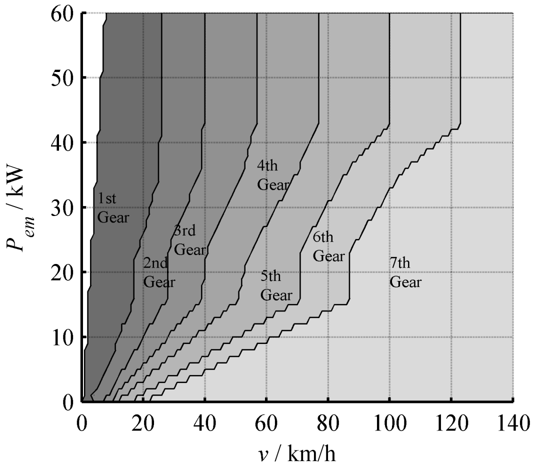

Fig. 5.12. Gear shifting schedule g_{em} in electric mode.

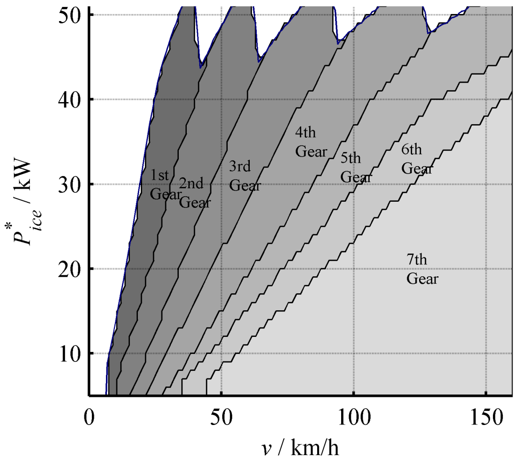

Fig. 5.13. Gear shifting schedule g_{ice} in hybrid mode.

5.4 Support Vector Machine

Automatic classification of operating mode as either electric or hybrid mode is done using a support vector machine (SVM). The SVM is a concept of the statistical learning theory [96], an area of research which was pioneered by Vapnik and Chervonenkis in the 1960s. It is used for pattern recognition, i.e. to find a separator for *pattern* belonging to two different classes. Firstly, the separator is calculated using patterns whose class known. Once found the separator, patterns of unknown class can be classified. The separator, an optimal hyperplane, can be found computational efficient by formulating a quadratic programming problem. The patterns, also called *observations*, are named by $\boldsymbol{x}_i$ and can be of any set X. The class y_i is usually defined as element of the set $y_i \in \{-1,1\}$. These pairs of pattern and their class are given by

$$\left\{(\boldsymbol{x}_1, y_{1,}), \dots, (\boldsymbol{x}_m, y_{m,}) | \boldsymbol{x}_i \in \mathrm{X}, y_i \in \{-1,1\}\right\} \quad . \tag{5.15}$$

The pattern $\boldsymbol{x}_i$ is defined here by the values P_{req} and v. The operating points in the 2-dimensional feature space can be separated linearly (Fig. 5.15), i.e. using a *linear kernel* function [97]. A SVM with linear kernel function separates both classes by the hyperplane (Fig. 5.14)

$$< \boldsymbol{w}, \boldsymbol{x} > +b = 0 \tag{5.16}$$

where $\boldsymbol{w} \epsilon \mathbb{R}^n, b \epsilon \mathbb{R}$ and the operator $<,>$ defining the canonical dot product. The canonical dot product for $\boldsymbol{x} \epsilon \mathbb{R}^n$ is defined as

$$< \boldsymbol{x}, \boldsymbol{x}' \geq \sum_{i=1}^{n} [\boldsymbol{x}]_i [\boldsymbol{x}']_i \tag{5.17}$$

where $[\boldsymbol{x}]_i$ denotes the ith entry of $\boldsymbol{x}$. The separating hyperplane of a SVM is called optimal hyperplane, as it separates the patterns of the two classes in such a way, that the distance (margin) of the training patterns to this hyperplane is maximized:

$$\max \min\{\|\boldsymbol{x} - \boldsymbol{x}_i\| \mid < \boldsymbol{w}, \boldsymbol{x} > +b = 0, i = 1, \dots, m\} \quad . \tag{5.18}$$

In order to relax the constraints, a *soft margin* is introduced by using slack variables ξ_i. This relaxation is necessary, as in practice the classes cannot be separated perfectly. After rescaling the normal vector $\boldsymbol{w}$ and the bias b of the hyperplane such that the points closest to the hyperplane satisfy $y_i(\langle \boldsymbol{w}, \boldsymbol{x}_i \rangle + b) \geq 1$, using the slack variables results

$$y_i(\langle \boldsymbol{w}, \boldsymbol{x}_i \rangle + b) \geq 1 - \xi_i \quad , \quad 1 \leq i \leq m \tag{5.19}$$

so that some patterns $\boldsymbol{x}_i$ can violate the separation by the hyperplane. Normalizing $\boldsymbol{w}$, the maximization problem Eq. (5.18) can be formulated as minimization problem of $\|\boldsymbol{w}\|$ which is equivalence to minimizing $\|\boldsymbol{w}\|^2$. Considering the slack variables, the optimal hyperplane is defined by

$$\min \frac{1}{2} \|\boldsymbol{w}\|^2 + \sum_{i=1}^{m} \xi_i \quad , \boldsymbol{w} \in \mathbb{R}^2 \tag{5.20}$$

This problem can be solved using quadratic programming (compare with MILP in Section 4.1) with the constraints of Eq. (5.19) (for more details see e.g. [97]).

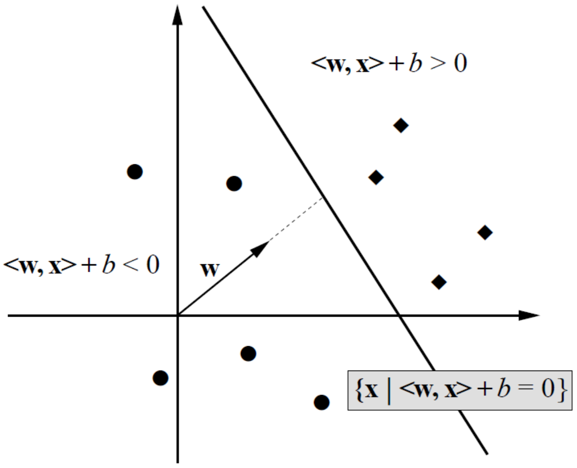

Fig. 5.14. Optimal hyperplane separator of patterns from two different classes [97].

In the present case, the patterns $\boldsymbol{x}_i$ are formed by the *m* optimized operating points of the powertrain for the next prediction horizon. The operating points are specified by sum of engine and electric motor power P_{req} and the vehicle speed v

$$\boldsymbol{x}_i = \begin{pmatrix} v \\ P_{req} \end{pmatrix} \quad . \tag{5.21}$$

The classification of the training patterns into the two classes *electric mode and hybrid mode* is made considering the corresponding torque T_{ice} of the operating point. If $T_{ice} = 0$, the pattern is from class 1 (electric mode). If $T_{ice} \neq 0$, the pattern is from class -1 (hybrid mode). After calculating the hyperplane defined by $\boldsymbol{w}$ and b, future operating points can be classified using the function

$$y_i = f(\boldsymbol{x}_i) = \operatorname{sgn}(\langle \boldsymbol{w}, \boldsymbol{x}_i \rangle + b) \quad . \tag{5.22}$$

As the patterns defined in Eq. (5.21) have only two characteristics and thus $\boldsymbol{x} \in \mathbb{R}^2$, the hyperplane is a straight line. The average classification error, i.e. the number of patterns that are misclassified by the hyperplane (outliers), are 2.56% for the FTP-72 cycle and 1.42% for the BCN-CTS cycle. The separator is used in the EMS by adding a hysteresis of ±2kW to prevent chattering of the engine, as whenever P_{req} passes the separator P_{hybrid} the engine is started or stopped.

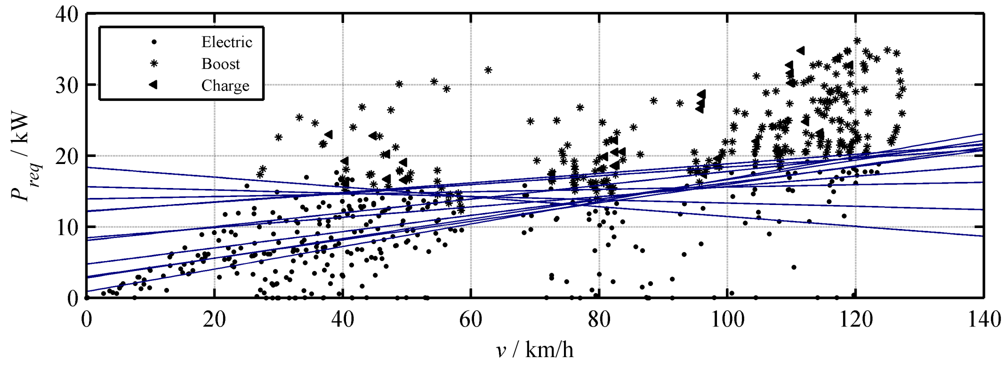

Fig. 5.15. Separator P_{hybrid} (blue lines) between electric mode and hybrid mode at different times during the BCN-CTS cycle calculated using SVM. Depicted are the predicted operating points and their optimal operation mode.

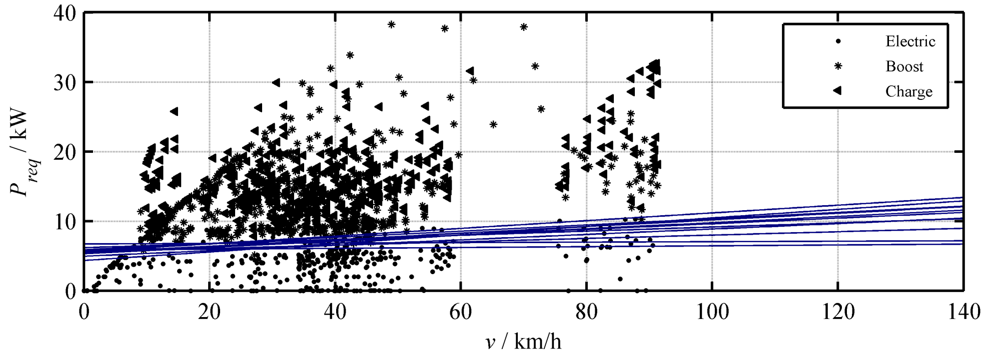

Fig. 5.16. Separator P_{hybrid} (blue lines) between electric mode and hybrid mode at different times during the FTP-72 cycle calculated using SVM.

5.5 EMS Implementation using Global Optimization

To evaluate the rule-based EMS without the influence of the real time implementable optimization from Section 4.4 later employed in the MPC framework, the rule-based strategy is carried out based on global optimal results ($N_p = \infty$) obtained by the S-DP algorithm presented in Section 3.1. In the following Section 5.7, instead the real time implementable optimization is used.

For rule adaptation by SVM, operating points of the next 200s. Simulations are carried out for the FTP-72 cycle using CS operation and the BCN-CTS cycle using CD operation. The control horizon is $N_c = 120$. Simulations are executed based on the assumption that $t_{calc} = 0$s (see Section 4.4 for a detailed explanation). A validation of this assumption is given in Section 5.6.

By way of example, the obtained rules are depicted in Fig. 5.17 and Fig. 5.18 for two sections of the BCN-CTS cycle. For the interval (600s; 720s], optimal control sequence $(\boldsymbol{u}_i^{opt})$ includes the hybrid mode as well as the electric mode. Therefore, SVM is employed and calculates the depicted limit P_{hybrid} between electric and hybrid mode. On the contrary, optimal control sequence $(\boldsymbol{u}_i^{opt})$ for the interval (1800s; 1920s] includes only the electric mode. Therefore, SVM is not executed and the limit P_{hybrid} is not included in the rule-based strategy (Fig. 5.18).

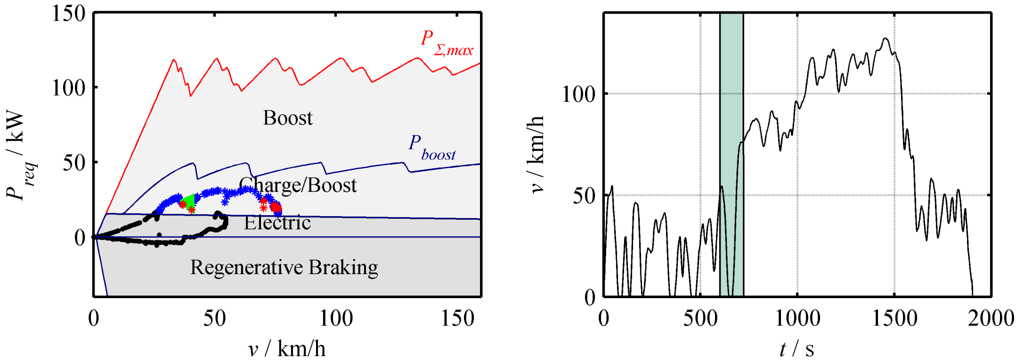

Fig. 5.17. Rule-based strategy 600 seconds into the BCN-CTS cycle obtained from $(\boldsymbol{u}_i^{opt})$ *for the marked trip section (right hand side) and resulting operating points (blue=boost, green=charge, red=ICE mode)*

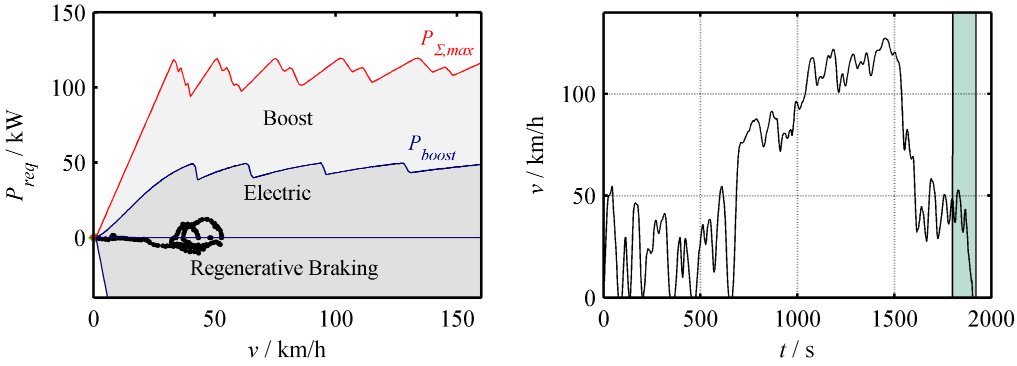

Fig. 5.18. Rule-based strategy 1800 seconds into the BCN-CTS cycle obtained from $(\boldsymbol{u}_i^{opt})$ *for the marked trip section (right hand side) and resulting operating points.*

The EMS operates in hybrid mode (Fig. 5.19) in phases with high power demand, i.e. acceleration phases ($t = 677$s) and during the motorway section (beginning second 1036). Selection of hybrid mode by the rule-based EMS coincides largely with the global optimum (calculated by S-DP from Section 3.1) indicated in Fig. 5.26. During these parts the optimal control sequence $(\boldsymbol{u}_i^{opt})$ is used. This leads to a strong coincidence of the engine operating points (Fig. 5.22 and Fig. 5.23). During the FTP-72 cycle with CS operation, the EMS starts the engine at lower power demand (Fig. 5.21), as due to missing high power sections the required charge maintenance is otherwise not achieved. A lower limit P_{hybrid} between electric and hybrid mode leads to a stronger influence of the hysteresis introduced between these modes (Fig. 5.16), resulting in a strong reduction of engine starts and engine operation at lower, less efficient load points (Fig. 5.24, Fig. 5.25).

Short peaks of P_{req} in acceleration phases can result in an undesired engine start, as caused by a positive road slope (Fig. 2.15) 1550 seconds into the BCN-CTS cycle (Fig. 5.20). In order to prevent these short engine starts, an additional delay could be introduced which starts the engine only when the power limit is exceeded for a certain time. In total, number of engine starts is reduced from 19 to 16 during the BCN-CTS cycle and from 74 to 55 during the FTP-72 cycle.

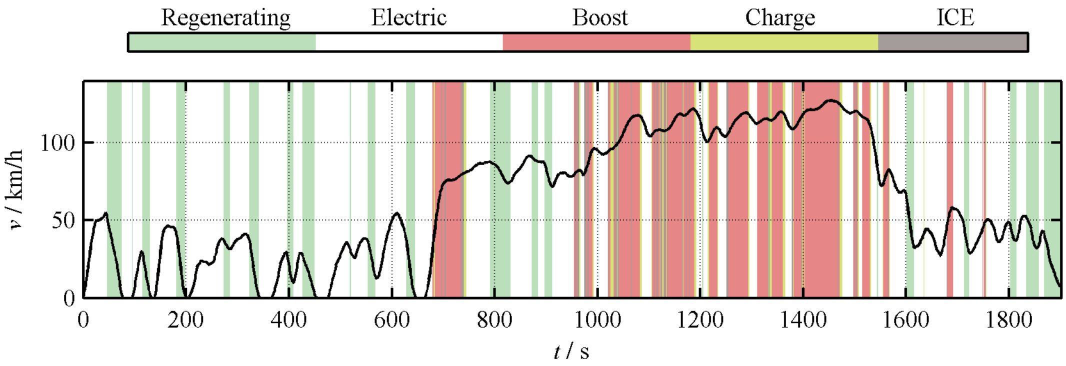

Fig. 5.19. Operation modes during the BCN-CTS cycle selected by the rule-based EMS.

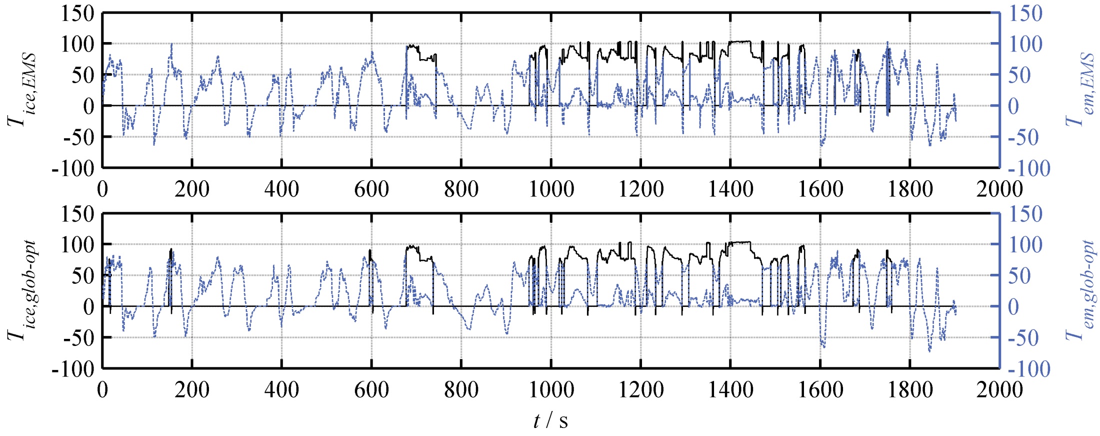

Fig. 5.20. Engine torque T_{ice} during the BCN-CTS cycle of the global optimum and the rule-based EMS.

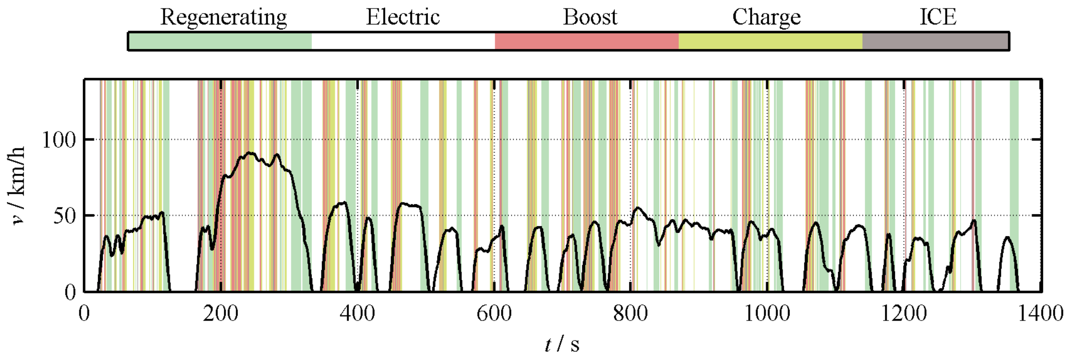

Fig. 5.21. Operation modes during the FTP-72 cycle selected by the rule-based EMS.

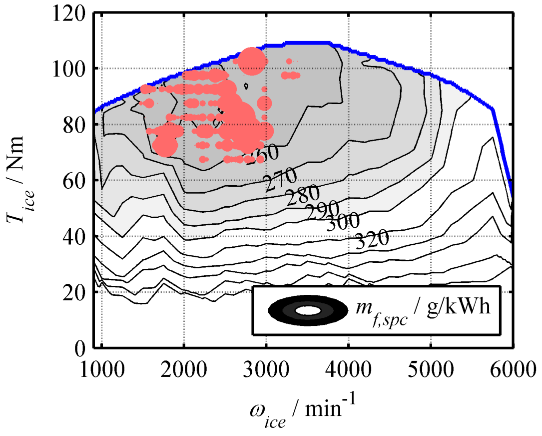

Fig. 5.22. Global optimum engine operating points during BCN-CTS.

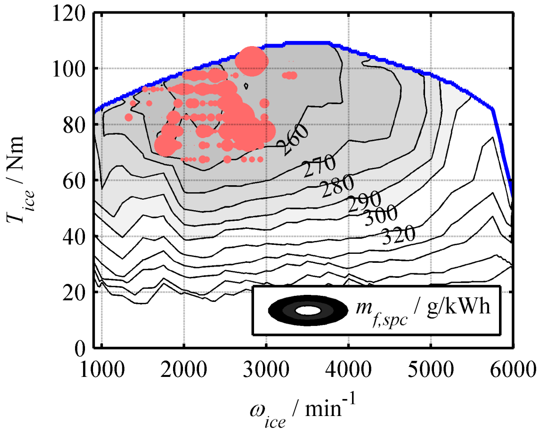

Fig. 5.23. Engine operating points during BCN-CTS using the rule-based EMS.

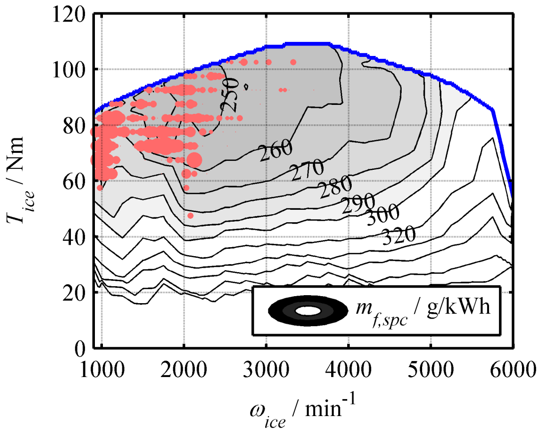

Fig. 5.24. Global optimum engine operating points during FTP-72.

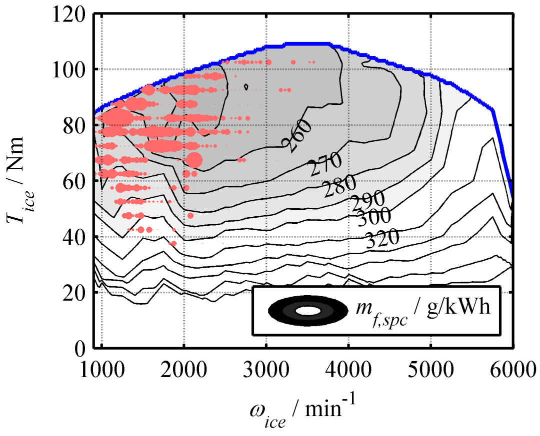

Fig. 5.25. Engine operating points during FTP-72 using the rule-based EMS.

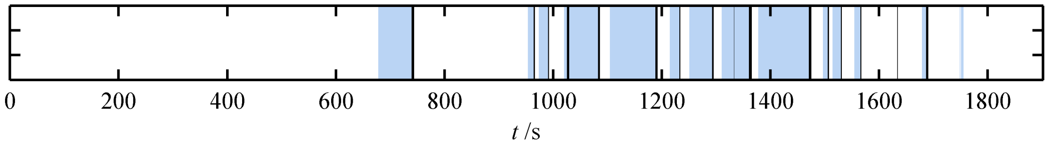

Fig. 5.26. Hybrid mode during BCN-CTS. Blue bars indicate that $\left(\boldsymbol{u}_i^{opt}\right)$ *is applied, while black bars indicate rule-based control from Section 5.2.2.*

Obtained results are compared to the global optimum in terms of fuel efficiency, i.e. the number of engine starts and gear shifts are disregarded. The relative differences

$$d_x = \frac{x_{EMS} - x_{glob-opt}}{x_{glob-opt}} \tag{5.23}$$

are indicated in Table XX. CO_2 emissions are calculated using Eq. (3.46).

For both cycles SOC at end of trip is at 0.295 and 0.297 close to the target SOC of 0.3. In the case of the FTP-72 cycle, the SOC deviation during the cycle is slightly different (Fig. 5.29) as the number of engine starts is significantly reduced (Fig. 5.27). However, this reduction in engine start/stops inevitably increases fuel and energy consumption by obtaining lower powertrain efficiency. Compared to the global optimum, fuel consumption increases by 0.7%, while m_{CO_2} increases by 1.5%. For the BCN-CTS cycle, fuel consumption increases by 0.9% and CO_2 emissions by 0.8%. Summarising, reducing the number of engine starts leads to a reduction in powertrain efficiency and thus a rise in both electrical energy and fuel consumption.

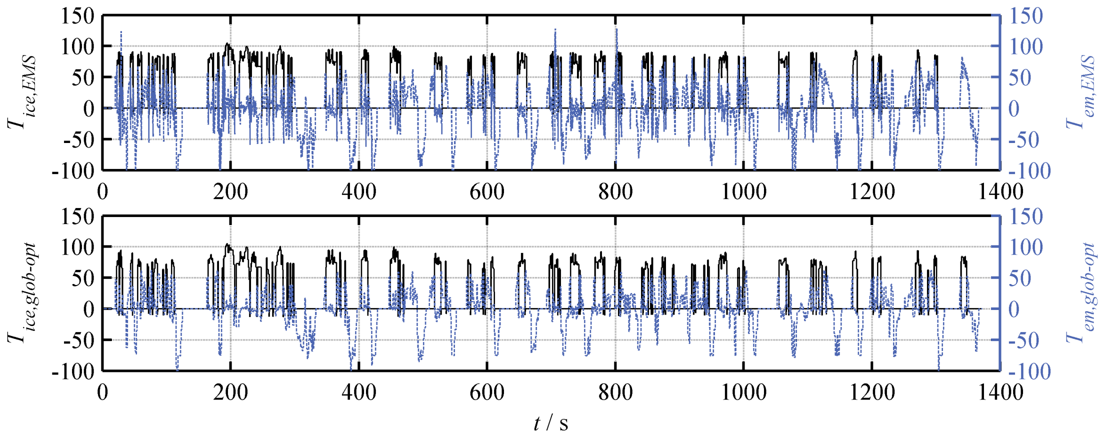

Fig. 5.27. Engine torque T_{ice} *during FTP-72 cycle of rule-based EMS and global optimum.*

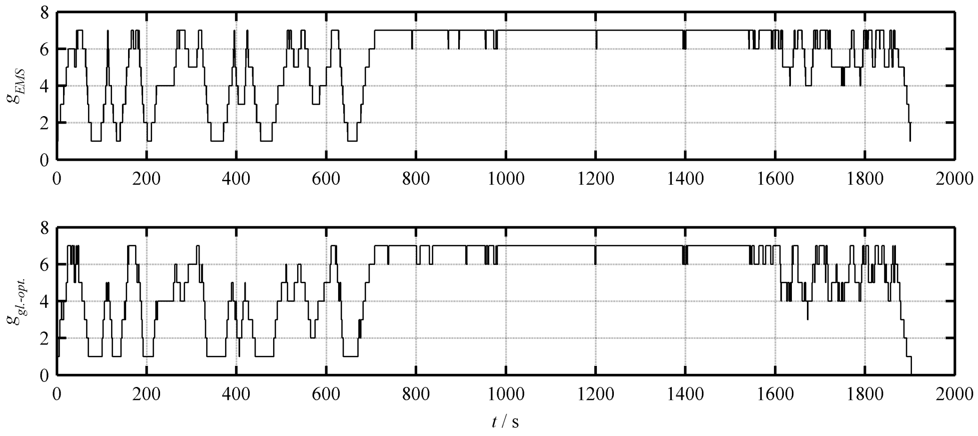

Fig. 5.28. Gear during the BCN-CTS cycle of rule-based EMS and global optimum.

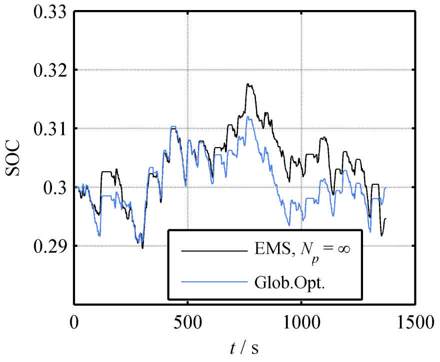

Fig. 5.29. SOC during the FTP-72 cycle of the rule-based EMS and the global optimum.

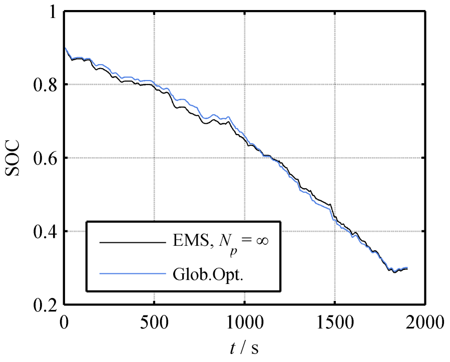

Fig. 5.30. SOC during the BCN-CTS cycle of the rule-based EMS and the global optimum.

Table XX: Simulation results for the cycles FTP-72 and BCN-CTS.

	FTP-72			BCN-CTS		
	EMS	Glob.opt.	d_x / %	EMS	Glob. opt.	d_x / %
SOC_{end}	0.295	0.300	-	0.297	0.301	-
V_f / l/100km	3.65	3.63	0.7	3.37	3.35	0.9
ΔE_{bat} / kWh/100km	0.180	0.005	-	7.290	7.249	0.6
m_{CO_2} /g/km	88.8	87.5	1.5	108.8	108.0	0.8
Engine starts	58	74	-21.6	17	19	-10.5
Gear shifts	486	527	-7.8	207	243	-14.8

5.6 Validation of Simulation Conditions

When starting the execution of the DP algorithm at time nN_c, the exact value of $SOC((n+1)N_c)$ at the beginning of the next control horizon is not known without the assumption of $t_{calc} = 0$ made in Section 4.4 and Section 5.5. The optimization algorithm therefore uses instead the estimation $\widetilde{SOC}\big((n+1)N_c\big)$ as an inital boundary condition x_0. This estimation is based on the set point function $SOC^*_{MILP}(k)$ and its deviation from the current $SOC(nN_c)$. An optimization starting at time nN_c uses the estimated $\widetilde{SOC}$

$$\widetilde{SOC}\big((n+1)N_c\big) = SOC^*_{MILP}\big((n+1)N_c\big) + [SOC^*_{MILP}(n\,N_c) - SOC(n\,N_c)]\,. \tag{5.24}$$

$\widetilde{SOC}\big((n+1)N_c\big)$ is the inital constraint $SOC^*(0)$ of the DP algorithm in the MPC framework, here the A-DP. The final constraint of the prediction horizon end is

$$SOC^*(k_N) = SOC^*_{MILP}\left((n+1)N_c + N_p\right) \quad . \tag{5.25}$$

Instead, results presented in the previous sections are obtained by the idealization of $t_{calc} = 0$, resulting in

$$\widetilde{SOC}\big((n+1)N_c\big) = SOC\big((n+1)N_c\big) \tag{5.26}$$

In a realistic scenario where the approximation $\widetilde{SOC}\big((n+1)N_c\big)$ from Eq. (5.24) is used as a boundary condition for the DP optimization with $N_c = 60$, results do not deteriorate (Table XXIII). The SOC across the cycle (Fig. 5.31) is similarly close to the global optimum. The final SOC of 0.293 instead of 0.296 is slightly further below the target of 0.3, resulting in lower fuel consumption of 3.67l/100km instead of 3.73l/100km

Table XXI: Simulation results of CS operation (FTP-72 cycle) with $N_c = 60$ using the estimation $\widetilde{SOC}$ from Eq. (5.24).

	EMS	Global optimum	d_x / %
SOC_{end}	0.293	0.300	-
V_f / l/100km	3.63	3.63	0.1
m_{CO_2} /g/km	88.5	87.5	1.1
Engine starts	59	74	-20.3

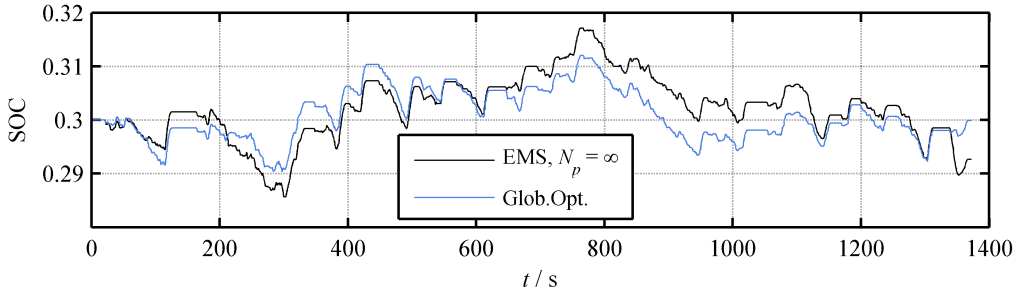

Fig. 5.31. SOC during FTP-72 cycle with $N_c = 60$ *using the estimation* $\widetilde{SOC}$ *from Eq. (5.24).*

5.7 EMS Implementation using A-DP

The EMS in Section 5.5 uses the S-DP algorithm within the MPC framework with infinite prediction horizon. As this is computationally too intensive for real time implementations, this section analyses the impact on results when using A-DP with receding prediction horizon from Section 4.4 instead. Results for the FTP-72 cycle and the cycles BCN-CTS, CTS-BCN and CADC are obtained using a prediction horizon of $N_p = 200$. For the cycles FTP-72 and BCN-CTS longer prediction horizons of $N_p = 300$ and $N_p = 450$ are also evaluated.

Calculation times using the A-DP algorithm with a receding prediction horizon are indicated in Section 4.4. The rule adaptation process increases the calculation times indicated in Table XVIII and Table XIX only slightly, as computational cost the rule adaptation by SVM is compared to the torque optimization small. The average calculation time for the SVM algorithm during the employed cycles is 0.45s for the FTP-72 and BCN-CTS, with a maximal calculation time of 0.59s during the FTP-72, and 0.58s during the BCN-CTS cycle. Calculation times are indicated for execution on an Intel i3 processor (1.8GHz) running Windows x64 (Table XXII).

Table XXII: Calculation time of the rule adaptation by SVM.

	FTP-72	BCN-CTS
$\bar{t}_{calc}$	0.45s	0.45s
$t_{calc,max}$	0.59s	0.58s

Comparing the simulation results to the results from Section 5.5 using global optimization, fuel economy is slightly lower. For both the FTP-72 and BCN-CTS cycle the final SOC is close to the target of 0.3, with a maximum deviation of 0.06 for $N_p = 200$ (Table XXI, Table XXIII). As a result of the higher negative final SOC deviation and thus higher electrical energy consumption for shorter prediction horizon lengths, fuel consumption V_f decreases from 0.5% to 1.6% for the FTP-72 cycle and from 1.4% to 0.9% for the BCN-CTS cycle (Table XXV) compared to the global optimum. This rise of V_f for the FTP-72 cycle strongly impacts on CO_2 emissions, as due to CS operation all traction energy is supplied by fuel energy. However, CO_2 emissions are almost constant for the BCN-CTS cycle with varying N_p values. The increase of V_f using longer prediction horizons is compensated for by using less electrical energy. Summarising, using shorter horizons, the EMS is less effective in achieving the target SOC, which influences fuel efficiency. In contrast, in the case discussed, fuel efficiency increases as more electrical energy is used. However, this deviation is undesired, as a definition of a target SOC closer to $E_{bat,min}$ could result from using the less efficient CS mode towards the cycle end. A deviation in the other direction, i.e. a higher SOC than the target SOC also has adverse effects on fuel economy.

Table XXIII: Simulation results for CS operation (FTP-72 cycle).

	EMS ($N_p = 200$)	EMS ($N_p = 300$)	EMS ($N_p = 450$)	Glob. opt.
SOC_{end}	0.294	0.295	0.297	0.300
V_f / l/100km	3.64	3.66	3.68	3.63
ΔE_{bat} / kWh/100km	0.197	0.158	0.086	0.005
m_{CO_2} /g/km	88.6	88.9	89.2	87.5

Table XXIV: Simulation results for CD operation (BCN-CTS cycle).

	EMS ($N_p = 200$)	EMS ($N_p = 300$)	EMS ($N_p = 450$)	Glob. opt.
SOC_{end}	0.294	0.299	0.302	0.301
V_f / l/100km	3.38	3.39	3.39	3.35
ΔE_{bat} / kWh/100km	7.327	7.266	7.266	7.249
m_{CO_2} /g/km	109.0	109.1	109.0	108.0

Table XXV: Relative difference to the global optimum for different prediction horizon lengths - simulation results for the cycles FTP-72 and BCN-CTS.

	BCN-CTS			FTP-72		
	d_{200} / %	d_{300} / %	d_{450} / %	d_{200} / %	d_{300} / %	d_{450} / %
V_f / l/100km	0.9	1.4	1.4	0.5	0.9	1.6
ΔE_{bat} / kWh/100km	1.1	0.2	-0.3	-	-	-
m_{CO_2} / g/km	1.0	1.0	0.9	1.3	1.5	1.9

5.7.1 Frequency of Engine Starts and Gear Shifts

Regarding the number of engine starts during the FTP-72 cycle, lengths the number is reduced for all simulated prediction horizon by more than 20% in comparison with the global optimum. The number of engine starts during the BCN-CTS cycle changes in respect to N_p between -21.1% and 0% reduction ($N_p = 300$, see Table XXVIII, Table XXIX). As a result from the different engine start control (Fig. 5.35, Fig. 5.36) engine average run time increases (Fig. 5.33, Fig. 5.34) and losses in the electric system are higher, which have to be compensated by more produced energy by the engine.

Changes in engine start control made by the rule-based EMS result in the engine operating at time instances where the operating point is sub-optimal in terms of engine and electric component efficiency. For avoiding engine efficiency, the powertrain operates in charge mode using load point shifting which results in an increased power transfer through the electric components. Using charge mode, electrical energy has to flow through the electric components twice: firstly when generating and storing the energy, and secondly when using it afterwards for boost or electric mode. This leads to an approximate electric system efficiency of

$$\bar{\eta}_{charge} = (\bar{\eta}_{em}\bar{\eta}_{inv}\bar{\eta}_{bat})^2 = 0.689 \tag{5.27}$$

with $\bar{\eta}_{em} = 0.95, \bar{\eta}_{inv} = 0{,}92, \bar{\eta}_{bat} = 0.95$, compared to

$$\bar{\eta}_{grid} = \bar{\eta}_{em}\bar{\eta}_{inv}\bar{\eta}_{bat} = 0.830 \tag{5.28}$$

when using electrical energy charged via the electrical grid.

The modified engine start control by the EMS during the BCN-CTS cycle results in a higher energy flow of $E_{bat,\Sigma} = 10.760\text{MJ}$ through the battery as defined in Eq. (4.23) compared to 10.007MJ of the global optimum. The difference results only partly from the 0.101MJ difference in charge depletion ΔE_{bat}. The same increase of energy flow occurs for the FTP-72 cycle, in which the total electrical power flow rises by 0.486MJ.

Increased energy flow through the electric system results in higher electrical energy losses, which have to be compensated for by the engine producing more mechanical energy. Despite more mechanical energy being produced by the engine, the total engine running time is shorter. Controlled by the EMS, engine running timer is 511s during the BCN-CTS and 331s during the FTP-72 cycle, while the global optimum is 535s and 348s respectively. The shorter running times together with a higher energy flow $E_{bat,\Sigma}$ indicate the use of the charge mode at high power load. The high electrical power flow in charge mode leads to phases of high battery use resulting in higher currents and higher ohmic losses by $P_{loss,ohmic} = I^2R$. Consequently, battery efficiency using the

EMS strategy is lower for all cycles (Table XXVI), which is also reflected in component energy losses of components (Fig. 5.32). While the engine efficiency is almost constant, engine losses are higher due to the additional energy which has to be generated to compensate for the higher losses in the electric system.

Table XXVI: Global optimum and rule-based EMS component efficiencies with $N_p = 200$.

	$\bar{\eta}_{ice}$		$\bar{\eta}_{em}$		$\bar{\eta}_{bat}$	
	Glob. Opt.	EMS	Glob. Opt.	EMS	Glob. Opt.	EMS
FTP-72	0.341	0.341	0.950	0.950	0.974	0.972
BCN-CTS	0.347	0.347	0.947	0.947	0.955	0.953
CTS-BCN	0.349	0.348	0.949	0.949	0.948	0.948
CADC	0.353	0.343	0.956	0.955	0.939	0.932

Table XXVII: Global optimum and EMS battery energy flow with $N_p = 200$.

	$E_{bat,\Sigma}$ / MJ		ΔE_{bat} / MJ	
	Glob. Opt.	EMS	Glob. Opt.	EMS
FTP-72	3.637	4.129	0.002	0.085
BCN-CTS	10.007	10.760	8.630	8.729
CTS-BCN	11.588	12.212	8.633	8.301
CADC	14. 548	14.414	8.648	8.595

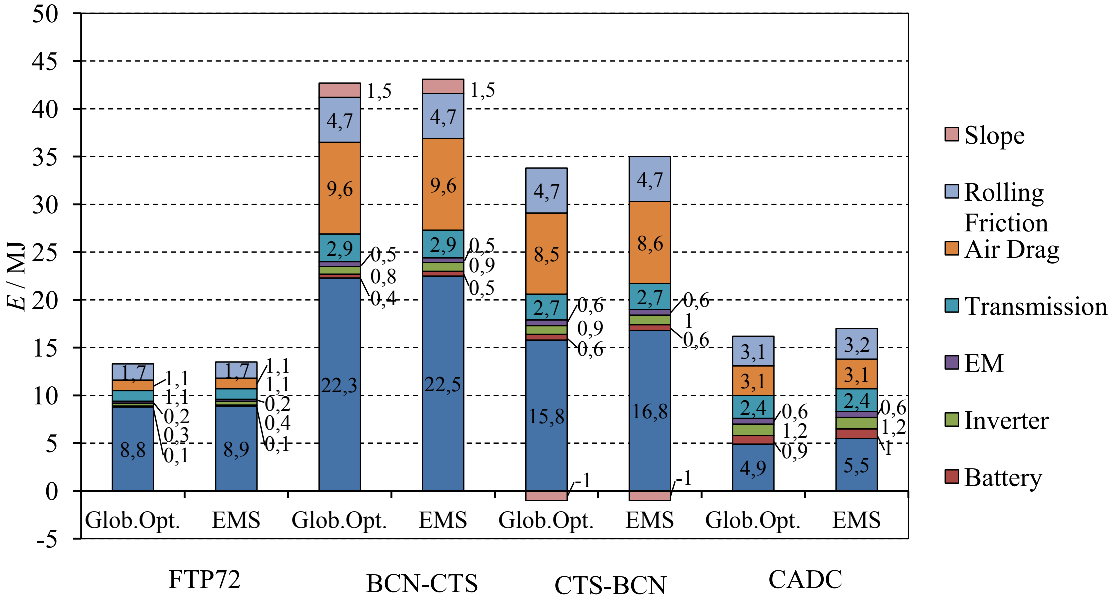

Fig. 5.32. Component losses for the different cycles compared to the global optimum.

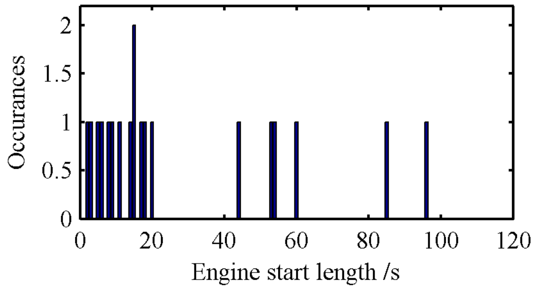

Fig. 5.33. Global optimum engine run time during the BCN-CTS cycle.

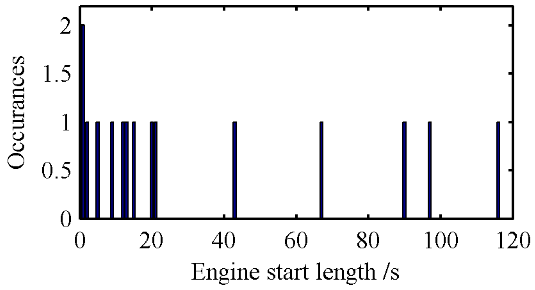

Fig. 5.34. Engine run time during the BCN-CTS cycle (EMS with $N_p = 200$).

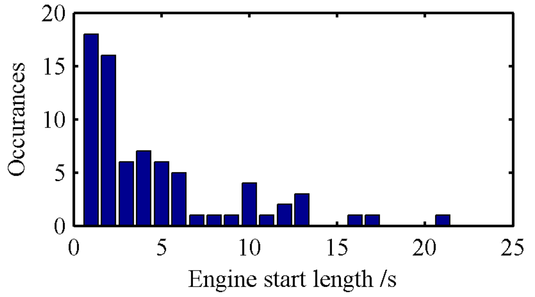

Fig. 5.35. Global optimum engine run time during the FTP-72 cycle.

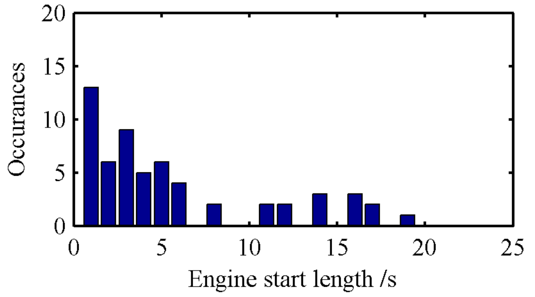

Fig. 5.36. Engine run time during the FTP-72 cycle (EMS with $N_p = 200$).

Table XXVIII: Simulation results and deviation from the global optimum for the FTP-72 cycle using different prediction horizon lengths.

	EMS ($N_p = 200$)	EMS ($N_p = 300$)	EMS ($N_p = 450$)	Global optimum
Engine starts	58 (-21.6%)	58 (-21.6%)	56 (-24.3%)	74
Gear shifts	492 (-6.6%)	484 (-8.2%)	490 (-7.0%)	526

Table XXIX: Simulation results for CD mode for the BCN-CTS cycle.

	EMS ($N_p = 200$)	EMS ($N_p = 300$)	EMS ($N_p = 450$)	Global optimum
Engine starts	15 (-21.1%)	16 (-15.8%)	17 (-10.5%)	19
Gear shifts	215 (-11.5%)	211 (-13.2%)	213 (-12.3%)	242

5.7.2 EMS Simulation for Driving Cycles CTS-BCN and CADC

In this section results obtained by the EMS for the cycles CTS-BCN and CADC are evaluated. Of special interest is the CTS-BCN cycle, as the set point function $SOC^*_{MILP}(k)$ calculated in Section 4.3 shows a significant deviation from the global optimum SOC in the middle part. Due to this deviation, using a prediction horizon of $N_p = 200$, a final SOC close to the objective of 0.3 cannot be achieved. The final SOC of 0.342 corresponds to 4% less electrical energy consumption ΔE_{bat} (Table XXX). Despite lower electrical energy consumption, total energy flow $E_{bat,\Sigma}$ is, with 0.624MJ, higher than the global optimum. Consequently, electric components energy losses are slightly higher (Fig. 5.32), taking into account that the charge mode and the later reutilization of the electrical energy causes the losses twice in the electric motor, inverter and battery. The differences of the energy loss in the engine with 16.8MJ compared to 15.8MJ does not result from the engine efficiency but from the greater requirement of mechanical energy to compensate the additional electrical losses and less use of stored electrical energy ΔE_{bat}.The reason for these higher losses is the set point function $SOC^*_{MILP}(k)$ in combination with the peculiarity of the cycle, which from second 1265 enters an urban section in combination with a negative slope (Fig. 5.39). Consequently, the power requirement is low and the EMS cannot, after initially following the function $SOC^*_{MILP}(k)$, over the last 900s of the trip consumes the stored electrical energy, to achieve the target SOC of 0.3 (Fig. 5.41). At the beginning of the low power section the global optimum SOC is lower than $SOC^*_{MILP}(k)$ (Fig. 5.40).

Using instead the global optimum SOC as set point function SOC^*_{S-DP}, the final SOC, 0.307, is significantly closer to the target SOC and fuel consumption only 3.3% higher (Table XXX) than the global optimum. For the CADC, the final SOC is 0.303, coming close to the target of 0.3, while the fuel consumption increases by 10.1%. This difference results partly from the lower engine efficiency, which is lower as a result from the EMS engine start control. However, relative rise in fuel consumption of 10.1% corresponds to an absolute increase of only 0.035l, which is reflected in the lower increase in CO_2 emissions per km by 3.5%.

Results show the importance of accuracy of the SOC set point function for achieving target SOC in PHEV, as fuel economy achieved depends heavily on the way of charge depletion across the trip. While lower fuel efficiency for the CTS-BCN results in part from engine start control, a further 1% increase in CO_2 emissions and 2.7% increase in fuel consumption (above the global optimum) results from sub-optimal discharging of the battery.

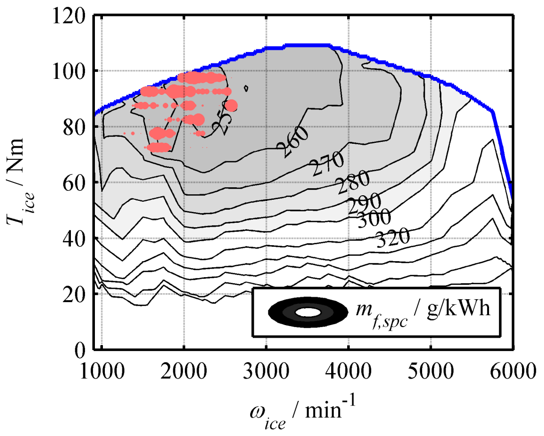

Fig. 5.37. Engine operating points during the CADC (global optimum).

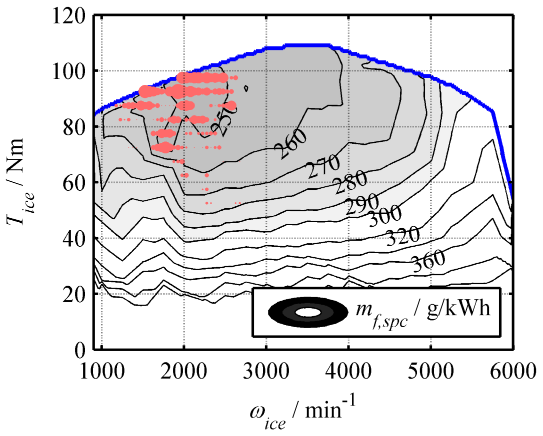

Fig. 5.38. Engine operating points during the CADC (EMS with $N_p = 200$).

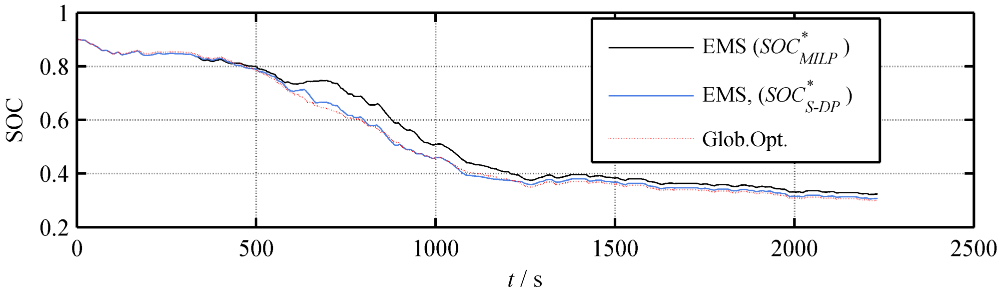

Fig. 5.39. SOC during the CTS-BCN cycle with $N_p = 200$.

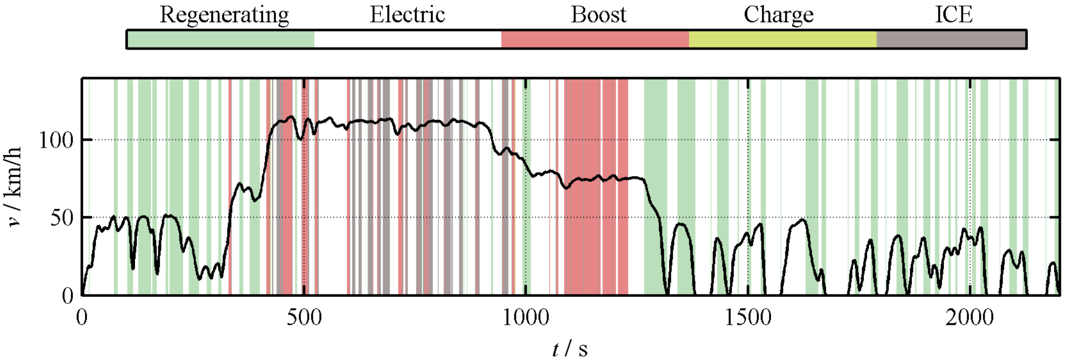

Fig. 5.40. Operation modes during CTS-BCN cycle (global optimum).

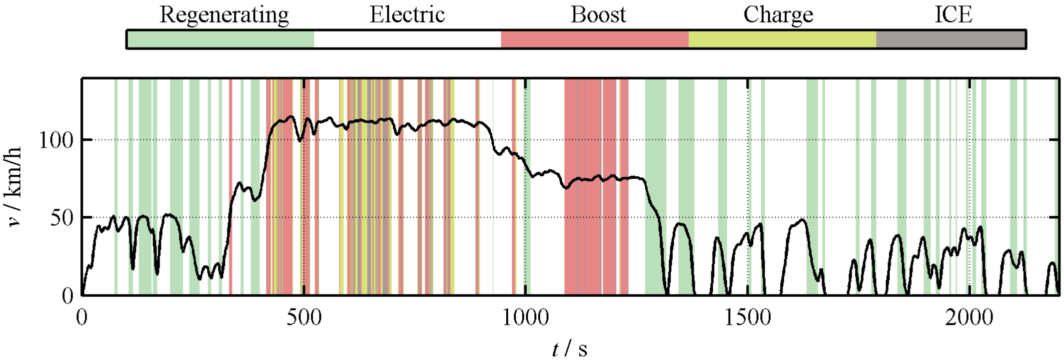

Fig. 5.41. Operation modes during CTS-BCN cycle (EMS, $N_p = 200$*).*

Table XXX: Relative difference to the global optimum of the strategy EMS with $N_p = 200$ *of the cycles CADC and CTS-BCN.*

	d_{CTS}/ % (SOC^*_{MILP})	d_{CTS}/ % (SOC^*_{DP})	d_{CADC} / %
SOC_{end}	0.324	0.307	0.303
V_f / l/100km	6.0	3.3	10.1
ΔE_{bat} / kWh/100km	-4.0	-1.3	-0.8
m_{CO_2}/ g/km	2.8	1.8	3.5
Engine starts	-52.6	-57.9	-8.2
Gear shifts	-14.1	-16.8	-13.9

5.8 Robustness against Inaccurate Prediction Data

Previous simulations are carried out assuming exact trip foreknowledge, in other words the EMS uses exact prediction data (EPD). In order to demonstrate the robustness of the EMS with inaccurate prediction data, in this section the EMS uses trip prediction data which does not correspond exactly with the real trip. The distorted prediction data (DPD) are used for predictive optimization and rule adaptation, while the vehicle drives the driving cycles BCN-CTS and FTP-72. In order to generate the DPD, an arbitrary noise is added to the standard trip profile by multiplying the cycle speed with a random time dependent factor $k_{dist}{}'$. Firstly, a random value k_{dist} is drawn from a uniform distribution from the interval (-0.05,0.05) with an expected value of 0. The sum of k_{dist} is the distortion factor at every time step:

$$k_{dist}^{\prime(k)} = \sum_{k'=1}^{k} k_{dist}\,(k) \quad . \tag{5.29}$$

These random values are used to calculate the cycle with the distorted cycle speed

$$v_{dist}(k) = v_{cycle}(k) \cdot \left[1 + k'^{(k)}_{dist}\right] \quad . \tag{5.30}$$

As the distortion factor $k'^{(k)}_{dist}$ is a sum, distortion grows with trip duration. This reflects that the prediction data accuracy decreases with increasing distance. However, trip prediction data is here not updated during the simulations with ongoing simulation time. From a generated set of different DPD, one DPD tending to a lower speed than the cycle (DPD1) and one DPD tending to higher velocity (DPD2) are chosen. The DPD is used for simulations with the BCN-CTS cycle (Fig. 5.42) and the FTP-72 cycle (Fig. 5.43).

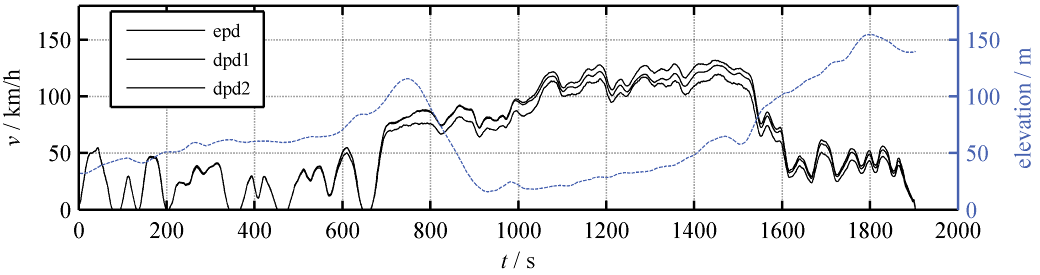

Fig. 5.42. Distorted prediction data (DPD1 and DPD2) for BCN-CTS cycle.

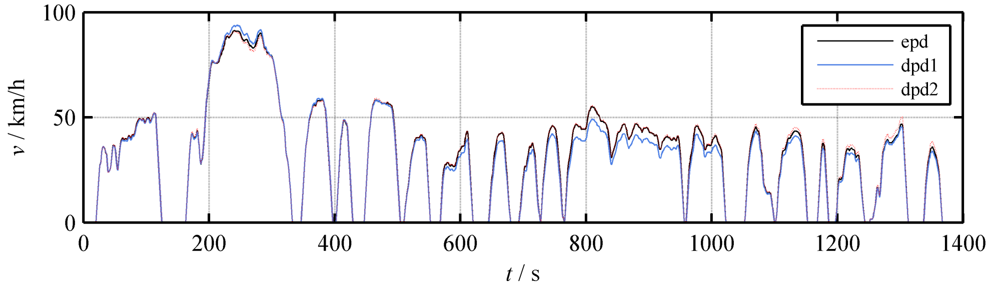

Fig. 5.43. Distorted prediction data (DPD1 and DPD2) for FTP-72 cycle.

Simulations are executed as in Section 5.7 with a control horizon length $N_c = 120$ and a prediction horizon length $N_p = 200$. Calculation of the set point function SOC^*_{MILP} and predictive optimization are performed using the DPD. During simulation, due to the deviation of DPD and real trip data, control sequence $(\boldsymbol{u}_i^{opt})$ calculated A-DP cannot as often used as in the case of exact prediction data. This is reflected in Fig. 5.44, which indicates the sections operating in hybrid mode in which the optimal control sequence $(\boldsymbol{u}_i^{opt})$ is applied (Fig. 5.26). When the vehicles operate in hybrid mode and $(\boldsymbol{u}_i^{opt})$ cannot be applied, the strategy described in Section 5.2 is used. The simulation results show that the proposed EMS is robust with inaccurate prediction data and still yields fuel economy close to the global optimum. For the FTP-72 cycle the final SOC is lower than the target of 0.3 (Table XXXI), while for the BCN-CTS cycle it is higher (Table XXXII). This leads to 2.5% higher CO_2 emissions for the BCN-CTS using the prediction data DPD1, and 1.7% higher emissions using the prediction data DPD2. Emissions rise for the FTP-72 by 1.9% and 1.2%. Lastly, number of engine starts is reduced in all cases by 15.8% -36.8%.

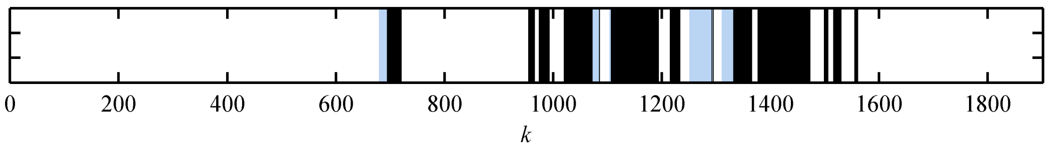

Fig. 5.44. Hybrid mode during BCN-CTS cycle (DPD1). Blue bars indicate that predictive optimization results ($\boldsymbol{u}_i^{opt}$) *are applied, while black bars indicate rule-based control from Section 5.2.2.*

Table XXXI: Simulation results and deviation from the global optimum for rule-based strategy in CS mode (FTP-72 cycle) and $N_p = 200$.

	EMS (DPD1)	EMS (DPD2)	Global optimum
SOC_{end}	0.296	0.293	0.300
V_f / l/100km	3.68 (1.4%)	3.64 (0.3%)	3.63
ΔE_{bat} / kWh/100km	0.121	0.234	0.005
m_{CO_2} /g/km	89.2 (1.9%)	88.6 (1.2%)	87.5
Engine starts	52 (-29.7%)	55 (-25.7%)	74
Gear shifts	478 (-9.1%)	496 (-5.7%)	526

Table XXXII: Simulation results and deviation from the global optimum for CD mode (BCN-CTS cycle) and $N_p = 200s$.

	EMS (DPD1)	EMS (DPD2)	Global optimum
SOC_{end}	0.303	0.301	0.301
V_f / l/100km	3.46 (3.5%)	3.42 (2.3%)	3.35
ΔE_{bat} / kWh/100km	7.210 (-0.5%)	7.244 (-0.1%)	7.249
m_{CO_2} /g/km	110.6 (2.5%)	109.8 (1.7%)	108.0
Engine starts	12 (-36.8%)	16 (-15.8%)	19
Gear shifts	201 (-16.9%)	205 (-15.3%)	242

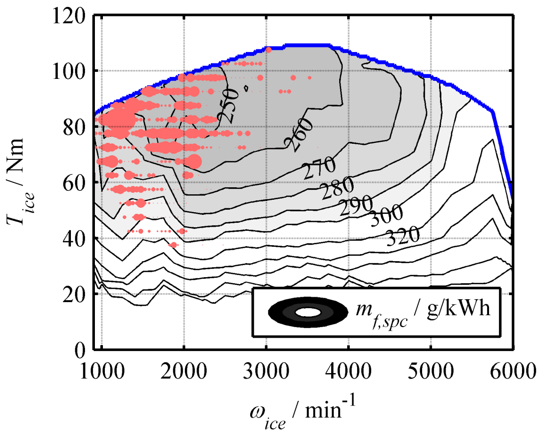

Fig. 5.45. Engine operating points during the FTP-72 cycle (N_p = 200, DPD1).

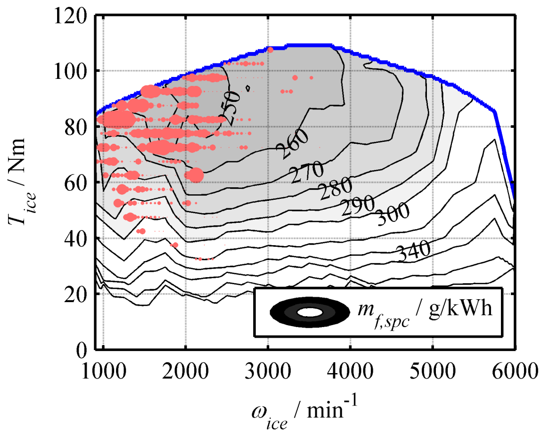

Fig. 5.46. Engine operating points during the FTP-72 cycle (N_p = 200, DPD2).

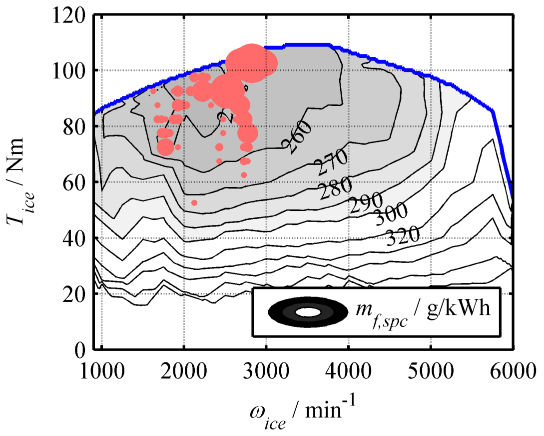

Fig. 5.47. Engine operating points during the BCN-CTS cycle (N_p = 200, DPD1).

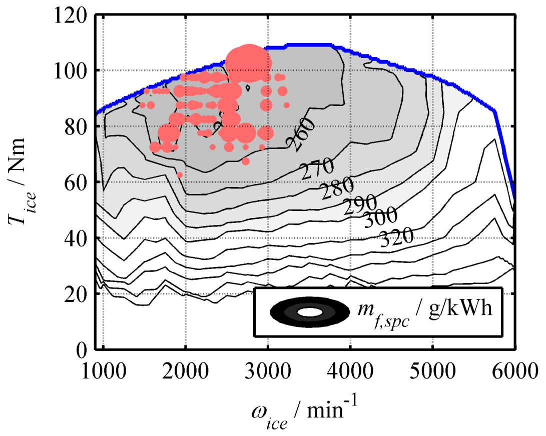

Fig. 5.48. Engine operating points during the BCN-CTS cycle (N_p = 200, DPD2).

5.9 Conclusions

The MPC approach using a receding prediction horizon from Chapter 4 achieves good results in terms of fuel economy and achieves optimal battery charge depletion across the trip. As the optimization results obtained relate to engine and electric motor torque, erroneous prediction data leads to torque deviations and thus to a deviation in vehicle speed. Using a torque ratio leads to sub-optimal results and can lead to an increased number of engine starts.

In order to employ the algorithm in a real-world scenario, considering divergence between trip predictions and actual trip values, the algorithm is integrated in a rule-based EMS structure. Where real vehicle speed deviates from predicted speed, a predefined local optimization is applied which considers vehicle speed and the torque demanded by the driver. Where vehicle speed and torque demand coincides with prediction data, torque obtained by predictive optimization is used.

Simulations of the EMS are carried out with a control horizon length of 120s, during which optimization for the following control horizon is executed. This includes calculation of gear and torque as well as an adaptation of the rule-based strategy which selects the operation mode. In addition to ensuring robustness against inaccurate prediction data, the rule-based EMS reduces frequency of engine starts and gear shifts. Results show a reduction of engine starts of 21.1%-57.9%, and of gear shifts of 6.6%-16.8% compared to the global optimum in terms of fuel economy. However, these improvements inevitably bring losses in fuel economy. Assuming exact prediction data, these losses are low, with fuel consumption and CO_2 emissions within 1.9% and 1.6% of compared to the global optimum respectively, for the BCN-CTS and FTP-72 cycle. From simulations of the CTS-BCN cycle and the CADC result greater deviations of 2.8% and 3.5%, respectively. In case of the CTS-BCN, the increase results partly from a sub-optimal SOC set point function and can be reduced to 1.8% using an accurate function. Increase for the CADC results from the greatly reduced number of engine starts by over 50%.

The EMS is robust against inaccurate prediction data in terms of fuel economy and engine start and gear shifting frequency. With inaccurate prediction data, predictive optimization is combined with a local optimization of torques in charge mode. Results show deviation of fuel economy and CO_2 emissions from the global optimum of below 2.5% of and 3.5% respectively.

6 Summary and Outlook

In this dissertation, a real time implementable energy management strategy (EMS) for plug-in HEV has been proposed. The EMS focuses on the optimization of torque and gear during a trip to minimize fuel consumption. Besides fuel economy, the following are also considered:

- optimal depletion of stored electrical energy across the entire trip
- the number of engine starts and gear shifts
- low computational cost.

Minimal fuel consumption is achieved by maintaining engine operation in high efficiency regions and the substitution of fuel for electrical energy stored in the battery as the power source. For optimal efficiency, fuel substitution requires a predictive optimization. Due to currently available technologies such as automobile navigation systems which use geographic information systems (GIS), trip foreknowledge can be assumed when the driver indicates his destination. In the near future, prediction quality is expected to improve further when new technologies such as intelligent transportation systems (ITS) and vehicle-to-vehicle communication (V2V) become available. The EMS uses torque and gear obtained from predictive optimization within an adaptive rule-based strategy, which improves drivability and assures improved fuel economy even when prediction data is inaccurate.

6.1 Summary of Contributions

The EMS which has been proposed presents a novel combination of a torque and gear optimization with an online optimized rule-based strategy. This combined optimization approach achieves minimal fuel consumption and improved drivability as well as less wear due to reduced frequency of gear shifts and engine start/stops. Torque/gear optimization and rule adaptation are executed sequentially by the EMS, in three optimization steps. The first execution step of the EMS is the calculation of a battery state of charge (SOC) set point function for the whole trip length. This function, which is calculated using a mixed integer linear program (MILP), leads to the following contributions:

- the use of two optimization algorithms, one of which is a MILP which defines the SOC boundary condition of a second DP algorithm, thus reducing the prediction horizon length and calculation cost within a charge-depleting strategy

- the use of MILP with a power flow based vehicle model to overcome model non-linearities.

In execution step two, the SOC function calculated using MILP is used as SOC boundary condition in a DP based algorithm in a model predictive control framework. The DP algorithm realizes an optimization of torque and gear using a receding prediction horizon. Results obtained by the accelerated DP algorithm show deviation from minimal consumption of electric and fuel energy weighted against CO_2 emissions of less than 0.07%. Computational cost is by a factor of approximately 50 significantly reduced. Further reduction in calculation time by approximately 99.8% can be achieved employing the DP algorithm in an MPC framework achieving deviation from the global optimum CO_2 emissions lower than 0.7%. Contributions in respect to the acceleration of dynamic programming for use in real time strategies are:

- the proposal of using vehicle specific lookup tables which are accessed in respect to the predicted driving cycle power demand and vehicle speed,
- the correction of rounding errors generated by using lookup tables by introducing an additional variable which approximates the resulting SOC error at every time step.

The algorithm is embedded in a rule-based EMS to reduce the number of engine starts and assure functionality of the EMS when prediction data is inaccurate. The novel contributions of the rule-based part of the EMS are

- the continuous adaptation of its rules during the trip bases on an online optimization to achieve the target SOC at end of trip,
- use of an optimized charge mode regarding the torque split within the rule-based strategy.

Results obtained demonstrate that carbon dioxide emissions are within 3.5% of the global optimum. These results are obtained by reducing both engine starts and gear shifts in comparison with the global optimum in terms of fuel efficiency. Even with distorted prediction data the deterioration of CO_2 emission was below 2.5%.

6.2 Outlook

The proposed strategy achieves a significant increase in fuel economy and an almost complete discharge of stored electrical energy during the cycle. However, the use of a receding prediction horizon for cycle patterns with a long section of low power demand towards the cycle end, as in the recorded CTS-BCN driving cycle, showed that due to inaccuracy of the SOC set point function, full charge depletion was not achieved. This behaviour results partly from the simplified linear vehicle model, and its constant battery and electric motor efficiency model. Therefore, further investigation could be directed at how convex description of these components, such as used in the above proposed engine model, improves results and affects calculation time.

Further research could also look at the behaviour of the adaptive rule-based strategy with real prediction data, i.e. trip data obtained from a trip prediction algorithm on a real trip. This can be realized by implementing the EMS in a real vehicle using equipment for rapid control prototyping. For real-time implementation, size of lookup tables used by the accelerated DP algorithm can be reduced.

Finally, further research has to focus on methods for implementing the EMS in vehicle control units. For this work, the EMS was realized by a script based implementation in Matlab. Real time application makes code optimizations and adaptations necessary.

References

[1] "EU transport in figures," European Comission, 2012.

[2] "End-user GHG emissions from energy: Reallocation of emissions from energy industries to end users 2005…-2010," EEA (European Environment Agency), Dec. 2012.

[3] *Regulation (EC) No 443/2009 of the European Parliament and of the Council of 23 April 2009 setting emission performance standards for new passenger cars as part of the Community's integrated approach to reduce CO 2 emissions from light-duty vehicles (Text with EEA relevance)*. .

[4] "Zahlen und Fakten - Energiedaten - Nationale und internationale Entwicklung," Bundesministerium für Wirtschaft und Technologie, Berlin, 2013.

[5] "Monitoring CO2 emissions from new passenger cars in the EU: summary of data for 2012," European Environment Agency, Copenhagen, 2013.

[6] W. Prestl and V. Wagner, "Energie-und Nachhaltigkeitsaspekte von Antrieben," *Automob. Z.*, vol. 114, no. 7/8, 2012.

[7] "European Environment Agency (EEA) - Data Viewer," *CO2 intensity of heat and electricity generation in 2009*. [Online]. Available: http://www.eea.europa.eu/data-and-maps/figures/co2-electricity-g-per-kwh. [Accessed: 23-May-2013].

[8] A. Atkins, "Reducing CO2 – The Ricardo Mechanical Hybrid Drive," in *Proc. 19. Aachener Kolloquium Fahrzeug und Motorentechnik*, Aachen, 2010.

[9] M. Kaszynski and O. Sawodny, "Determining the fuel savings potential of parallel hybrid hydraulic vehicles," *Int. J. Powertrains*, vol. 1, no. 1, pp. 22–42, Jan. 2011.

[10] M. Ceraolo, A. di Donato, and G. Franceschi, "A general approach to energy optimization of hybrid electric vehicles," *Veh. Technol. IEEE Trans.*, vol. 57, no. 3, pp. 1433–1441, 2008.

[11] T. Takaoka, M. Komatsu, and G. Killmann, "Newly Developed Toyota Plug-in Hybrid System and its Vehicle Performance," in *Proc. 19. Aachener Kolloquium Fahrzeug und Motorentechnik*, Aachen, 2010.

[12] R. Bady and J. W. Biermann, "Hybrid-Elektrofahrzeuge-Strukturen und zukünftige Entwicklungen," 2000.

[13] O. Sundström, L. Guzzella, and P. Soltic, "Optimal hybridization in two parallel hybrid electric vehicles using dynamic programming," in *Proceedings of the 17th IFAC world congress*, 2008, pp. 4642–4647.

[14] D. Karbowski, S. Pagerit, J. Kwon, A. Rousseau, and K. Pechmann, "Fair comparison of powertrain configurations for plug-in hybrid operation using global optimization," in *SAE World Congress*, Detroit, 2009, pp. 01–1334.

[15] S. Kim, J. Park, J. Hong, M. Lee, and H. Sim, "Transient control strategy of hybrid electric vehicle during mode change," SAE, SAE Technical Paper 2009-01-0228, 2009.

[16] T. van Keulen, B. de Jager, J. Kessels, and M. Steinbuch, "Energy Management in Hybrid Electric Vehicles: Benefit of Prediction," in *Proc. IFAC Symposium on Advances in Automotive Control, München*, 2010.

[17] E. Hellström, M. Ivarsson, J. \AAslund, and L. Nielsen, "Look-ahead control for heavy trucks to minimize trip time and fuel consumption," *Control Eng. Pr.*, vol. 17, no. 2, pp. 245–254, 2009.

[18] V. H. Johnson, K. B. Wipke, and D. J. Rausen, "HEV control strategy for real-time optimization of fuel economy and emissions," *SAE Trans.*, vol. 109, no. 3, pp. 1677–1690, 2000.

[19] L. Engvall, A. Cook, and A. Khaligh, "A predictive trip-based method for state of charge maintenance in series PHEVs to boost cold weather efficiency," in *2012 IEEE Transportation Electrification Conference and Expo (ITEC)*, 2012, pp. 1–6.

[20] F. Will and A. Boretti, "A New Method to Warm Up Lubricating Oil to Improve the Fuel Efficiency During Cold Start," SAE International, Warrendale, PA, SAE Technical Paper 2011-01-0318, Apr. 2011.

[21] J. Gonder and T. Markel, "Energy management strategies for plug-in hybrid electric vehicles," *Energy*, vol. 1, p. 0290, 2007.

[22] J. J. Valera García, "Control y gestión inteligente del sistema de propulsión en los vehículos eléctricos de autonomía extendida_," Universidad del País Vasco, Spain, 2013.

[23] C. Zhang, A. Vahidi, P. Pisu, X. Li, and K. Tennant, "Role of Terrain Preview in Energy Management of Hybrid Electric Vehicles," *IEEE Trans. Veh. Technol.*, vol. 59, no. 3, pp. 1139–1147, 2010.

[24] Q. Gong, Y. Li, and Z. Peng, "Power management of plug-in hybrid electric vehicles using neural network based trip modelling," in *American Control Conference, 2009. ACC'09.*, 2009, pp. 4601–4606.

[25] A. Sciarretta and L. Guzzella, "Control of hybrid electric vehicles," *Control Syst. IEEE*, vol. 27, no. 2, pp. 60–70, 2007.

[26] S. G. Wirasingha and A. Emadi, "Classification and Review of Control Strategies for Plug-In Hybrid Electric Vehicles," *IEEE Trans. Veh. Technol.*, vol. 60, no. 1, pp. 111–122, 2011.

[27] C.-C. Lin, H. Peng, J. W. Grizzle, and J.-M. Kang, "Power management strategy for a parallel hybrid electric truck," *Control Syst. Technol. IEEE Trans.*, vol. 11, no. 6, pp. 839–849, 2003.

[28] M. Salman, N. J. Schouten, and N. A. Kheir, "Control strategies for parallel hybrid vehicles," in *American Control Conference, 2000. Proceedings of the 2000*, 2000, vol. 1, pp. 524–528 vol.1.

[29] S. G. Li, S. M. Sharkh, F. C. Walsh, and C. N. Zhang, "Energy and Battery Management of a Plug-In Series Hybrid Electric Vehicle Using Fuzzy Logic," *IEEE Trans. Veh. Technol.*, vol. 60, no. 8, pp. 3571–3585, Oct. 2011.

[30] S. Delprat, J. Lauber, T. M. Guerra, and J. Rimaux, "Control of a parallel hybrid powertrain: optimal control," *Veh. Technol. IEEE Trans.*, vol. 53, no. 3, pp. 872–881, 2004.

[31] S. Stockar, V. Marano, M. Canova, G. Rizzoni, and L. Guzzella, “Energy-Optimal Control of Plug-in Hybrid Electric Vehicles for Real-World Driving Cycles,” *IEEE Trans. Veh. Technol.*, vol. 60, no. 7, pp. 2949–2962, Sep. 2011.

[32] S. Kermani, R. Trigui, S. Delprat, B. Jeanneret, and T. M. Guerra, “PHIL implementation of energy management optimization for a parallel HEV on a predefined route,” *Veh. Technol. IEEE Trans.*, vol. 60, no. 3, pp. 782–792, 2011.

[33] J. T. Kessels, M. W. Koot, P. P. van den Bosch, and D. B. Kok, “Online energy management for hybrid electric vehicles,” *Veh. Technol. IEEE Trans.*, vol. 57, no. 6, pp. 3428–3440, 2008.

[34] V. Ngo, T. Hofman, M. Steinbuch, and A. Serrarens, “Optimal Control of the Gearshift Command for Hybrid Electric Vehicles,” *IEEE Trans. Veh. Technol.*, vol. 61, no. 8, pp. 3531 –3543, Oct. 2012.

[35] N. Kim, S. Cha, and H. Peng, “Optimal Control of Hybrid Electric Vehicles Based on Pontryagin’s Minimum Principle,” *IEEE Trans. Control Syst. Technol.*, vol. 19, no. 5, pp. 1279–1287, 2011.

[36] G. Paganelli, S. Delprat, T. M. Guerra, J. Rimaux, and J.-J. Santin, “Equivalent consumption minimization strategy for parallel hybrid powertrains,” in *Vehicular Technology Conference, 2002. VTC Spring 2002. IEEE 55th*, 2002, vol. 4, pp. 2076–2081.

[37] A. Kleimaier and D. Schroder, “An approach for the online optimized control of a hybrid powertrain,” in *7th International Workshop on Advanced Motion Control, 2002*, 2002, pp. 215–220.

[38] M. Stiegeler, “Entwurf einer vorausschauenden Betriebsstrategie für parallele hybride Antriebsstränge,” Universität Ulm. Fakultät für Ingenieurwissenschaften und Informatik, 2008.

[39] G. Paganelli, M. Tateno, A. Brahma, G. Rizzoni, and Y. Guezennec, “Control development for a hybrid-electric sport-utility vehicle: strategy, implementation and field test results,” in *Proceedings of the American Control Conference*, 2001, vol. 6, pp. 5064–5069.

[40] C. Musardo, G. Rizzoni, Y. Guezennec, and B. Staccia, “A-ECMS: An adaptive algorithm for hybrid electric vehicle energy management,” *Eur. J. Control*, vol. 11, no. 4–5, p. 509, 2005.

[41] A. Sciarretta, L. Guzzella, and M. Back, “A real-time optimal control strategy for parallel hybrid vehicles with on-board estimation of the control parameters,” in *Proc. IFAC Symp. Adv. Automotive Contr*, 2004, pp. 19–23.

[42] D. Ambühl and L. Guzzella, “Predictive reference signal generator for hybrid electric vehicles,” *Veh. Technol. IEEE Trans.*, vol. 58, no. 9, pp. 4730–4740, 2009.

[43] R. E. Bellman, *Dynamic Programming*. Princeton, NJ: Princeton University Press, 1957.

[44] Q. Gong, Y. Li, and Z. R. Peng, “Trip-based optimal power management of plug-in hybrid electric vehicles,” *Veh. Technol. IEEE Trans.*, vol. 57, no. 6, pp. 3393–3401, 2008.

[45] M. Koot, J. Kessels, B. de Jager, W. Heemels, P. P. J. Van den Bosch, and M. Steinbuch, “Energy management strategies for vehicular electric power systems,” *Veh. Technol. IEEE Trans.*, vol. 54, no. 3, pp. 771–782, 2005.

[46] A. Brahma, Y. Guezennec, and G. Rizzoni, “Dynamic optimization of mechanical/electrical power flow in parallel hybrid electric vehicles,” in *Proceedings of 5th Int. Symposium on Advanced Vehicle Control*, Ann Arbor, 2000.

[47] A. Brahma, Y. Guezennec, and G. Rizzoni, “Optimal energy management in series hybrid electric vehicles,” in *Proceedings of the American Control Conference*, Chicago, 2000, vol. 1, pp. 60–64 vol.1.

[48] M. A. M. Asbogard, L. Johannesson, D. Angervall, and P. Johansson, “Improving System Design of a Hybrid Powertrain Using Stochastic Drive Cycles and Dynamic Programming,” in *SAE World Congress & Exhibition, April 2007, Detroit, MI, USA*, 2007.

[49] Y. H. Hung, J. F. Tsai, C. T. Wu, C. T. Hsu, and S. M. Lo, “On-line suboptimal control strategies for a power-assist hybrid electric vehicle’,” in *Proc. SAE World Congress*, 2007.

[50] M. Back, “Predictive control of drivetrains,” in *Proceedings of the 15th IFAC World Congress*, Barcelona, 2002, pp. 1506–1506.

[51] E. D. Tate, J. W. Grizzle, and H. Peng, “Shortest path stochastic control for hybrid electric vehicles,” *Int. J. Robust Nonlinear Control*, vol. 18, no. 14, pp. 1409–1429, 2008.

[52] S. J. Moura, H. K. Fathy, D. S. Callaway, and J. L. Stein, “A stochastic optimal control approach for power management in plug-in hybrid electric vehicles,” *Control Syst. Technol. IEEE Trans.*, vol. 19, no. 3, pp. 545–555, 2011.

[53] L. J. L. Johannesson, M. A. M. Asbogard, and B. E. B. Egardt, “Assessing the Potential of Predictive Control for Hybrid Vehicle Powertrains Using Stochastic Dynamic Programming,” *IEEE Trans. Intell. Transp. Syst.*, vol. 8, no. 1, pp. 71–83, 2007.

[54] E. D. Tate and S. P. Boyd, “Finding ultimate limits of performance for hybrid electric vehicles,” *SAE Trans.*, vol. 109, no. 6, pp. 2437–2448, 2000.

[55] R. Beck, A. Bollig, and D. Abel, “Comparison of two real-time predictive strategies for the optimal energy management of a hybrid electric vehicle,” *Oil Gas Sci. Technol.-Rev. IFP*, vol. 62, no. 4, pp. 635–643, 2007.

[56] P. Pisu and G. Rizzoni, “A comparative study of supervisory control strategies for hybrid electric vehicles,” *Control Syst. Technol. IEEE Trans.*, vol. 15, no. 3, pp. 506–518, 2007.

[57] A. Sciarretta, M. Back, and L. Guzzella, “Optimal control of parallel hybrid electric vehicles,” *IEEE Trans. Control Syst. Technol.*, vol. 12, no. 3, pp. 352–363, 2004.

[58] D. F. Opila, X. Wang, R. McGee, R. B. Gillespie, J. A. Cook, and J. W. Grizzle, “An Energy Management Controller to Optimally Trade Off Fuel Economy and Drivability for Hybrid Vehicles,” *IEEE Trans. Control Syst. Technol.*, vol. 20, no. 6, pp. 1490–1505, 2012.

[59] O. Sundström, P. Soltic, and L. Guzzella, “A Transmission-Actuated Energy-Management Strategy,” *IEEE Trans. Veh. Technol.*, vol. 59, no. 1, pp. 84–92, 2010.

[60] C. Zhang and A. Vahidi, “Route Preview in Energy Management of Plug-in Hybrid Vehicles,” *IEEE Trans. Control Syst. Technol.*, vol. 20, no. 2, pp. 546–553, 2012.

[61] B. Bader, O. Torres, J. Ortega, G. Lux, and J. L. Romeral, “Reduction of the Prediction Horizon of a Predictive Energy Management for a Plug-in HEV in Hilly Terrain,” in *Proc. Urban Transport 2012*, A Coruña, 2012.

[62] G. Rizzoni, L. Guzzella, and B. M. Baumann, “Unified modelling of hybrid electric vehicle drivetrains,” *IEEEASME Trans. Mechatronics*, vol. 4, no. 3, pp. 246 – 257, Sep. 1999.

[63] V. Ngo, T. Hofman, M. Steinbuch, and A. Serrarens, “Effect of Gear Shift and Engine Start Losses on Control Strategies for Hybrid Electric Vehicles,” in *Proc. Symposium EVS26*, Los Angeles, 2012.

[64] A. J. Markel and A. Simpson, *Plug-in hybrid electric vehicle energy storage system design*. National Renewable Energy Laboratory, 2006.

[65] Y. Gao and M. Ehsani, “Design and control methodology of plug-in hybrid electric vehicles,” *Ind. Electron. IEEE Trans.*, vol. 57, no. 2, pp. 633–640, 2010.

[66] K. B. Wipke, M. R. Cuddy, and S. D. Burch, “ADVISOR 2.1: a user-friendly advanced powertrain simulation using a combined backward/forward approach,” *Veh. Technol. IEEE Trans.*, vol. 48, no. 6, pp. 1751–1761, 1999.

[67] A. Rousseau and R. Larsen, “Simulation and Validation of Hybrid Electric Vehicles Using PSAT,” in *Global Powertrain Congress, Detroit, June*, 2000, pp. 6–8.

[68] P. Fritzson, *Principles of object-oriented modelling and simulation with Modelica 2.1*. Piscataway, NJ: IEEE Press [u.a.], 2004.

[69] L. Poeti, J. Marco, and N. D. Vaughan, “Object oriented plant models for HEV controller development,” *SAE Tech. Pap. 2009-01-0148*, 2009.

[70] V. H. Johnson, “Battery performance models in ADVISOR,” *J. Power Sources*, vol. 110, no. 2, pp. 321–329, Aug. 2002.

[71] S. J. Pachernegg, “A Closer Look at the Willans-Line,” SAE International, Warrendale, PA, SAE Technical Paper 690182, Feb. 1969.

[72] M. Andre, “Real-world driving cycles for measuring cars pollutant emissions–Part A: The ARTEMIS European driving cycles,” *Rep. INRETS-LTE*, vol. 411, p. 97, 2004.

[73] L. Guzzella and A. Sciarretta, *Vehicle Propulsion Systems: Introduction to Modelling and Optimization*, 3rd ed. 2013. Springer, 2012.

[74] Y. Rosefort, B. Lüers, M. Wittler, M. Salmen, and M. Simm, “Zukünftige Anforderungen an die Abgasmesstechnik,” *MTZ-Mot. Z.*, vol. 71, no. 10, pp. 706–711, 2010.

[75] M. Back, “Prädiktive Antriebsregelung zum energieoptimalen Betrieb von Hybridfahrzeugen,” Univ.-Verlag Karlsruhe, 2005.

[76] H. Mosbech, "Optimal control of hybrid vehicle," in *Proc., International Symp. on Automotive Technology & Automation (ISATA'80)*, 1980, vol. 2, pp. 303–320.

[77] M. Oprean, V. Ionescu, N. Mocanu, S. Beloiu, and C. Stanciu, "Dynamic programming applied to hybrid vehicle control," in *Proc. of the International Conf. on Electric Drives (ICED 88)*, 1988, vol. 4, p. D2.

[78] A. Sciarretta, L. Guzzella, and C. H. Onder, "On the power split control of parallel hybrid vehicles: from global optimization towards real-time control," *Automatisierungstechnik*, vol. 51, no. 5, pp. 195–203.

[79] D. P. Bertsekas, *Dynamic programming and optimal control*, vol. 1. Athena Scientific Belmont, MA, 1995.

[80] Q. Gong, Y. Li, and Z.-R. Peng, "Trip based power management of plug-in hybrid electric vehicle with two-scale dynamic programming," in *Vehicle Power and Propulsion Conference, 2007. VPPC 2007. IEEE*, 2007, pp. 12–19.

[81] G.-E. Katsargyri, I. V. Kolmanovsky, J. Michelini, M. L. Kuang, A. M. Phillips, M. Rinehart, and M. A. Dahleh, "Optimally controlling Hybrid Electric Vehicles using path forecasting," 2009, pp. 4613–4617.

[82] B. Bader, O. Torres, G. Lux, and J. L. Romeral, "Influence of the Prediction Horizon length of a PHEV Energy Management on Fuel consumption," in *Proc. Symposium EVS26*, Los Angeles, 2012.

[83] D. G. Luenberger, *Linear and nonlinear programming*. Springer, 2003.

[84] S. P. Boyd and L. Vandenberghe, *Convex optimization*. Cambridge, UK; New York: Cambridge University Press, 2004.

[85] G. Sierksma, *Linear and integer programming: theory and practice*. New York: Marcel Dekker, 2002.

[86] R. Vanderbei, *[Linear Programming] Foundations and Extensions (International Series in Operations Research & Management Science #114)] BY [Vanderbei, Robert]Paperback*. Springer, 2010.

[87] L. Wang, *Model predictive control system design and implementation using MATLAB®*. London: Springer, 2009.

[88] M. Böckl, "Adaptives und prädiktives Energiemanagement zur Verbesserung der Effizienz von Hybridfahrzeugen / Michael Böckl," TU Wien, 2008.

[89] J. Yan, C. Li, H. Qian, G. Xu, and Y. Xu, "Multi-objective parameters optimization of electric assist control strategy for parallel hybrid electric vehicle," in *Advanced Intelligent Mechatronics, 2009. AIM 2009. IEEE/ASME International Conference on*, 2009, pp. 1992–1997.

[90] B. Kim, Y. Kim, T. Kim, Y. Park, and S. W. Cha, "HEV Cruise Control Strategy on GPS (Navigation) Information," *EVS24*, 2009.

[91] A. Rousseau, S. Pagerit, and D. W. Gao, "Plug-in hybrid electric vehicle control strategy parameter optimization," *J. Asian Electr. Veh.*, vol. 6, no. 2, pp. 1125–1133, 2008.

[92] Bingzhan Zhang, C. C. Mi, and Mengyang Zhang, “Charge-Depleting Control Strategies and Fuel Optimization of Blended-Mode Plug-In Hybrid Electric Vehicles,” *IEEE Trans. Veh. Technol.*, vol. 60, no. 4, pp. 1516–1525, May 2011.

[93] H.-D. Lee, S.-K. Sul, H.-S. Cho, and J.-M. Lee, “Advanced gear-shifting and clutching strategy for a parallel-hybrid vehicle,” *IEEE Ind. Appl. Mag.*, vol. 6, no. 6, pp. 26 –32, Dec. 2000.

[94] H. S. Cho, “Design of the powertrain system of a hybrid vehicle and development of its driving control algorithm,” Seoul National University, 1998.

[95] W. Wang, Q. Wang, and X. Zeng, “Automated Manual Transmission Shift Strategy for Parallel Hybrid Electric Vehicle,” SAE International, Warrendale, PA, SAE Technical Paper 2009-01-0144, Apr. 2009.

[96] V. N. Vapnik, *Statistical Learning Theory*, 1st ed. Wiley-Interscience, 1998.

[97] B. Schölkopf and A. J. Smola, *Learning with Kernels: Support Vector Machines, Regularization, Optimization, and Beyond*. Mit Press, 2002.

Glossary

A-DP	Accelerated DP algorithm
AER	All-electric range
BEV	Battery electric vehicle
CADC	Common Artemis Driving Cycle
CD	Charge-depleting
CS	Charge-sustaining
DP	Dynamic programming
ECU	Engine control unit
EM	Electric motor
EMS	Energy management strategy
FTP	Federal Test Procedure
GIS	Geographic information system
GPS	Global Positioning System
HEV	Hybrid electric vehicle
ICE	Internal combustion engine
ITS	Intelligent transportation system
LP	Linear programming
MILP	Mixed integer linear programming
MPC	Model predictive control
NEDC	New European Driving Cycle
PHEV	Plug-in hybrid electric vehicle
S-DP	Standard DP algorithm
SOC	State of charge
SOE	State of energy
SVM	Support vector machine
V2V	Vehicle-to-vehicle communication